Technische Universität München

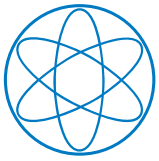

Physik Department

Long-Lived and Efficient Qubit Memory for Photonic Quantum Networks

Ulf Matthias Körber

Dissertation

Max-Planck-Institut für Quantenoptik, Garching

and Physik Department, Technische Universität München

June 2020

Max-Planck-Institut für Quantenoptik

Technische Universität München

Long-Lived and Efficient Qubit Memory for Photonic Quantum Networks

Ulf Matthias Körber

Vollständiger Abdruck der von der Fakultät für Physik der Technischen Universität München zur Erlangung des akademischen Grades eines

Doktors der Naturwissenschaften (Dr. rer. nat.)

genehmigten Dissertation.

Vorsitzende :		Prof. Dr. Nora Brambilla
Prüfer der Dissertation :	1.	Hon.-Prof. Dr. Gerhard Rempe
	2.	Prof. Dr. Rudolf Gross

Die Dissertation wurde am 09.06.2020 bei der Technischen Universität München eingereicht und durch die Fakultät für Physik am 26.10.2020 angenommen.

Contents

Summary

Optical quantum memories are crucial ingredients for a multitude of quantum network protocols. In this thesis, the efficient absorption and emission of a single-photon polarization qubit in a complex-valued temporal mode by a single-atom-based light-matter interface is analytically investigated and experimentally demonstrated. Further, an unprecedented storage time of more than 100 ms is achieved by intermittently mapping the stored qubit to a decoherence-protected atomic storage basis.

Zusammenfassung

Optische Quantenspeicher sind wesentliche Bestandteile vieler Quantennetzwerkprotokolle. In dieser Arbeit wird die effiziente Absorption und Emission eines Polarisationsqubits in einer komplexwertigen zeitlichen Mode von einer Einzelatom-Licht-Materie-Schnittstelle analytisch untersucht und experimentell demonstriert. Zudem wird eine bisher unerreichte Speicherzeit von mehr als 100 ms demonstriert, indem das Qubit zwischenzeitlich in einen vor Dekohärenz geschützten atomaren Unterzustand transferiert wird.

1.Introduction

At the end of the 19^{th} century, theoretical physics failed to predict the spectral energy density of the electromagnetic field emitted by a black body in thermal equilibrium. Based on the assumption that energy is equally distributed over all oscillator modes, the prevailing theories predicted the *ultraviolet catastrophe*, a diverging energy density for high frequencies [1]. To resolve this issue, Max Planck quantized the energy packets, which the oscillator modes can emit and absorb, and thereby introduced the famous Planck constant h [2]. With Einstein's interpretation of the photo-electric effect in 1905 [3], this notion was dramatically extended, and the photon as the quantized carrier of energy in the electromagnetic field was introduced. Later, with the advent of the wave-function formalism, modern quantum physics was created and thereby two states of matter that lack a classical counterpart: the superposition of mutually exclusive states and the entanglement, a *superposition of correlations* between multiple quantum particles sharing a common and indivisible state. Especially, the latter gave rise to skepticism about the completeness of the quantum theory, because a measurement on one of two entangled and potentially far separated particles immediately affects the state of the other particle. This *spooky action at a distance* contradicts the principle of relativity and local realism [4]. Since then, significant efforts have been made to experimentally demonstrate [5–11] the violation of Bell's inequality [12] to confirm that quantum mechanics is indeed complete and that realism is a non-local property of nature. Today, one century after the foundation of quantum physics was created, the controlled manipulation of quantum systems and especially the non-locality of entangled quantum states distributed in future large-scale networks is about to change the way we approach communication and computation complexity [13].

A defining property of entangled quantum systems is that the size of their state space grows exponentially with the number of quantum particles. This drastically limits the ability to simulate complex physical phenomena with classical computers. Therefore, in 1982, Richard Feynman suggested that due to the quantumness of nature itself, only quantum systems can serve as an efficient simulation platform for complex physical problems [14, 15]. Three years later, David Deutsch turned this scaling argument around and showed that quantum systems could also be employed as a general computation device with the potential to gain significant speedups for classical problems. This led to the development of quantum algorithms, which allow for up to an exponential speedup [16–19] compared to their classical counterparts.
First experimental implementations of quantum computers with a few qubits were shown in nuclear-magnetic-resonance systems [20], but the usability of those systems is limited due to their poor scaling behavior [21]. More recent approaches employ trapped ions [22–24] or superconducting circuits [25–27], but despite promising results, the scaling to large qubit numbers with universal two-qubit gates is very demanding [28, 29].
One way to solve the scalability problem of quantum computers is to interconnect smaller computational nodes in a quantum network [30]. Besides achieving scalability [31–33], this approach also yields new applications like the formation of highly accurate and precise network clocks [34]. Additionally, finding consensus in a faulty classical network is a common but very costly task, which can be solved more efficiently by sharing quantum states [35–39] via quantum channels. Finally, the exchange of quantum states between network nodes allows for the creation of communication channels that are secured against eavesdropping by the fundamentals of quantum physics [40–44]. The inability to amplify quantum states [45, 46] forbids the undetected eavesdropping on quantum communication channels,

but simultaneously renders the creation of a large-scale quantum network a major challenge.

To establish a quantum network, qubits must be faithfully exchanged between network nodes [47]. The photon is the natural carrier for this state exchange in a long-distance quantum network because it can be transmitted with the speed of light and only weakly interacts with the environment [48–50]. Nevertheless, unavoidable losses in optical fibers or diffraction losses in free-space render the direct transmission of photonic qubits challenging [51]. To overcome this limitation, the quantum repeater was proposed [52, 53] to establish entanglement between the sender and the receiver node and to use quantum teleportation to transmit the state [54–57], but the implementation of a quantum repeater is demanding. For a working large-scale quantum network that allows for distributed quantum computations, three essential criteria were identified [30, 49, 58]: long-lived qubit storage, efficient and coherent light-matter interfaces and high-fidelity gates between multiple qubits at a network node. For quantum information applications, a suitable light-matter interface must support controlling the complex-valued temporal mode of the emitted and absorbed photon. This is critical to achieving indistinguishability between photons to allow for a high interference contrast. Furthermore, control over the temporal modes is vital to creating compatibility between different systems in a hybrid quantum network [58].
One of the significant challenges to create a quantum network is the identification of a platform that fulfills these requirements. For instance, long coherence times have been observed in various systems but without an efficient interface [59–64]. A prominent example is quantum computing nodes based on trapped-ions, which also exhibit high-fidelity gate operations, but the mediation of efficient light-matter interactions is an outstanding challenge [65–67]. In contrast, efficient storage of a polarization qubit in a Bose-Einstein condensate was demonstrated but with a storage time insufficient for a large-scale quantum network [68]. Additionally, control over the intensity profile of single photons was achieved with various systems including atomic ensembles and atom-cavity systems [69–76], and the manipulation of the phase of a temporal mode was demonstrated with electro-optic modulators [77, 78] but an efficient conversion between complex-valued temporal modes over a broad range is still an unsolved problem.

One prominent candidate that simultaneously allows for efficient and coherent light-matter interactions, two-qubit gates, and long coherence times are neutral atoms trapped [79, 80] in high-finesse optical cavities formed by super polished mirrors [81]. Such cavity systems exhibit a strong coupling between a single photonic excitation and the atom [82, 83] and therefore allow for the formation of an efficient light-matter interface [84–89]. Moreover, control over the temporal mode was theoretically demonstrated for three-level atoms [90–92]. Also, atom cavity systems can be employed to perform quantum gates between a single photon and an atom, between two atoms trapped in the same resonator, and also to mediate quantum gates between two photons [93–95]. Furthermore, the storage of a polarization qubit on a single atom trapped in a resonator was demonstrated with moderate storage times [87, 96] and the same atomic species was found to support significantly longer coherence times by utilizing a different set of atomic basis states [97]. Additionally, a high level of control over all degrees of freedom of a single atom inside an optical resonator was demonstrated, including three-dimensional cooling of the atom into its motional ground state [98], as well as positioning the atom with submicron accuracy [99]. The applicability of atom-cavity systems for quantum network applications has already been demonstrated by creating entanglement between an atom and a photon, exchanging the state between two resonator system directly or by teleportation and entangling an atom-cavity system with a Bose-Einstein condensate in a hybrid network [56, 100, 101]. Finally, the development of new fiber-based microresonators with higher light-matter interaction rates [102–104] will

push the potential of atom-cavity systems further rendering those a vital platform for research.

In this thesis, the potential of single-atom cavity systems for quantum network applications is advanced by achieving significant improvements addressing two of the three above mentioned criteria, namely the efficient and coherent light-matter interface and the long-lived storage of polarization qubits carried by single-photons.
The coherent absorption and emission of a single photon from an atom-cavity system are improved significantly by generalizing the model by Gorshkov *et al.* [90] from a three-level atom to an n-level atom. By incorporating the full relevant level structure, the correct relation between the control pulse and the absorbed or emitted temporal photonic modes is found. This advances the light-matter interface in two crucial regards. By applying the model for the three-level atom to the experimental apparatus, the absorption efficiency degrades with an increasing atom-resonator detuning. This poses a significant limitation onto the usability of the light-matter interface since atom-resonator detunings are crucial for scaling the system towards multiple atoms with controllable light-matter interactions. Additionally, even for single-atom cavity systems, a vanishing atom-resonator detuning is not necessarily the optimal working point in terms of interface efficiency and the purity of the emitted modes and underlines the importance of the free-choice of the atom-resonator detuning. Furthermore, precise control over temporal modes is inevitable for quantum information applications and the independent control over the absorbed and emitted modes enables the atom-cavity system to interconvert between a broad range of temporal modes, thereby establishing compatibility between various systems in a hybrid network.
In terms of long-lived storage of photonic polarization qubits, a significant breakthrough is achieved: By coherently mapping the stored qubit between a pair of basis states used for the light-matter interactions and another pair used during the storage period, magnetic field fluctuations are eliminated as the dominant source of decoherence. Further decoherence mechanisms are suppressed by the implementation of the spin-echo technique, resulting in a coherence time of the stored polarization qubit for longer than 100 ms. Compared to prior work [96] this is an increase by almost three orders of magnitude and poses the first demonstration of photonic qubit storage with a coherence time exceeding the lower bound for the direct teleportation of qubits in a global quantum network [105].

This thesis is structured as follows: In the first part, a generalized formalism based on the work of Gorshkov *et al.* is derived that incorporates an arbitrary number of excited states. This formalism is then applied to ^{87}Rb with the level structure used for the light-matter interface, and the impact of the individual excited states is investigated. Subsequently, numerical methods are used to verify the predictions of the model and to quantify the impact of incoherent processes. Finally, the model is compared to experimental results followed by a demonstration of the temporal mode conversion capabilities for quantum network applications.
In the second part, the previously demonstrated light-matter interface is employed for the storage of single-photon polarization qubits. After magnetic field fluctuations are identified as the limiting source of decoherence, a basis transfer scheme is developed to map the qubit to a magnetically insensitive atomic state pair during the storage time. Subsequently, the scheme is tested experimentally, and the observed residual decoherence is utilized to identify additional decoherence mechanisms. To eliminate the identified mechanisms, a spin-echo technique is employed, further prolonging the coherence of the stored qubit followed by a final analysis of the remaining decoherence rate. The thesis concludes by summarizing the results along with a discussion of the implications for future experiments.

2.Atom-Cavity Light-Matter Interface

The content of this chapter is based on the prior publication:

Deterministic shaping and reshaping of single-photon temporal wave functions
O. Morin, M. Körber, S. Langenfeld & G. Rempe
Phys. Rev. Lett, volume **123**, 133602 (2019)

2.1. Motivation and Structure

Light-matter interactions are the foundation of future quantum networks based on quantum information carried by single photons which are exchanged between stationary matter-based network nodes. In this chapter, the absorption and emission processes of a single photon from a single atom trapped in a high-finesse optical resonator are studied. The focus of this chapter is to optimize the light-matter interaction efficiency and to gain full control over the temporal photonic mode in the single-photon absorption and emission process. In prior work [96], the absorption and subsequent emission of a single photon were described as a *Stimulated Raman Adiabatic Passage* (STIRAP) process [106, 107]. However, the applicability of this semi-classical model to the cavity-assisted absorption and emission of a single photon is limited. Theoretical work from multiple groups [90–92] was carried out to model the absorption and emission of a single quantum of light and to provide control over the temporal mode of the photon.

In collaboration with Prof. Giovanna Morigi and Luigi Gianelli from the University of Saarland, the model by Gorshkov *et al.* [90] was identified to be a suitable model for the atom-cavity system used throughout this thesis. Although initially designed for atomic ensembles, it was verified by Gianelli *et al.* [108] that it is also applicable to a single-atom resonator system in the intermediate coupling regime. In contrast to the work by Fleischhauer *et al.* [92] and Dilley *et al.* [91], it also allows for a detuning between the resonator and the atomic transition. Although Gianelli *et al.* integrated multiple loss channels to the model of Gorshkov *et al.* [90], providing a better resemblance of the actual experimental conditions, a striking mismatch between the theoretical predictions and our experimental results could not be resolved. With an increasing detuning of the cavity mode from the atomic resonance, the efficiency of the light-matter interface rapidly degrades for the storage process, and the temporal mode of a produced photon diverges from the prediction. Since a non-vanishing atom-cavity detuning allows for scaling the atom-cavity system to multiple emitters coupled to the same cavity mode and high efficiencies are crucial for future quantum networks, a profound understanding of the light-matter interaction is of vital importance.

Here, an extension of the model by Gorshkov *et al.* is derived, which incorporates an arbitrary number of atomic excited states. The model correctly predicts the efficiency of the coherent light-matter interactions for all atom-cavity detunings. Further, it allows for precisely controlling the temporal mode of the produced photon including its phase profile.

The structure of this chapter is as follows: After a short introduction to the system, the model by Gorshkov *et al.* is generalized to include multiple excited states. The solutions of the underlying differential equations are first discussed in general and then applied to the atom-resonator system used throughout this thesis. The theoretical predictions are

then compared to numerical calculations that simulate the dynamics of the system without the assumptions used in the derivation of the model. Decremental effects that limit the coherence of the light-matter interactions are identified and checked against numerical predictions. The theoretical expectation of the light-matter interface efficiency is compared to experimental results followed by a thorough investigation of the control over the complex temporal envelope of the created photons. Finally, the control over the absorbed and emitted mode is utilized to demonstrate two possible applications, the mode-selective absorption and the mode-conversion-capabilities of the system.

2.2. Theoretical Background

2.2.1. Cavity Assisted Light Matter Interactions

A single atom with two ground states $|g\rangle$ and $|s\rangle$ and n excited states $|e_i\rangle$ is optically trapped at the center of a high-finesse optical cavity. The resonator field is detuned by Δ_i from the transition $|g\rangle \leftrightarrow |e_i\rangle$ and couples these states with the light-matter interaction rate g_i given by

$$g_i = \sqrt{\frac{\omega_c}{2\hbar\epsilon_0 V}}\mu_{ge_i}, \tag{2.1}$$

with the vacuum permittivity ϵ_0, the resonance frequency of the cavity ω_c, the mode volume of the cavity V and the atomic dipole moment μ_{ge_i} for the transition $|g\rangle \leftrightarrow |e_i\rangle$. A macroscopic control field with frequency ω_p is aligned perpendicular to the cavity axis and couples the second ground state $|s\rangle$ to the excited states $|e_i\rangle$ with the time-dependent Rabi frequencies $2\Omega_{c,i}(t)$. This is illustrated in Figure 2.1. Once the ground states $|g\rangle$ and $|s\rangle$ are both coupled to an excited state $|e_i\rangle$, a so-called Λ-system is formed, and the population transfer between $|g\rangle$ and $|s\rangle$ can be mediated by $|e_i\rangle$. Note that each excited state allows for the creation of a Λ-system. The system is in two-photon resonance, meaning that the transition frequency of the two ground states governed by their energy difference matches the frequency difference of the cavity mode and the control field:

$$E_{|s\rangle} - E_{|g\rangle} = \Delta E = \hbar(\omega_p - \omega_c) \tag{2.2}$$

In dipole and rotating-wave approximation, the dynamics of the driven atom-cavity system for a three-level Λ-system, with only one excited state $|e\rangle$, is given by the interaction Hamiltonian [96, 108]

$$\hat{H}_{\text{int}}^{(3-lvl)} = \Delta|e\rangle\langle e| + (g|e\rangle\langle g|\hat{a} + \Omega_c(t)|e\rangle\langle s| + h.c.) \ , \tag{2.3}$$

with the annihilation operator $\hat{a}$ for the cavity mode excitation. Here, the first term is associated with the energy of the excited state in the rotating frame of the cavity mode. The second term describes the absorption of a cavity excitation from the atom, and the third term corresponds to the coupling of $|g\rangle$ and $|s\rangle$ by the control field with Rabi frequency $2\Omega_c(t)$. For a system with n excited states $|e_i\rangle$, the interaction Hamiltonian can be straightforwardly extended to

$$\hat{H}_{\text{int}}^{(n-lvl)} = \sum_i \Delta_i \left(|e_i\rangle\langle e_i|\right) + \left[\sum_i \left(g_i|e_i\rangle\langle g|\hat{a} + \Omega_{c,i}(t)|e_i\rangle\langle s|\right) + h.c.\right]. \tag{2.4}$$

Note that this Hamiltonian only describes the unitary evolution of the closed atom-cavity system. For a complete description of the open system including the coupling of the atom

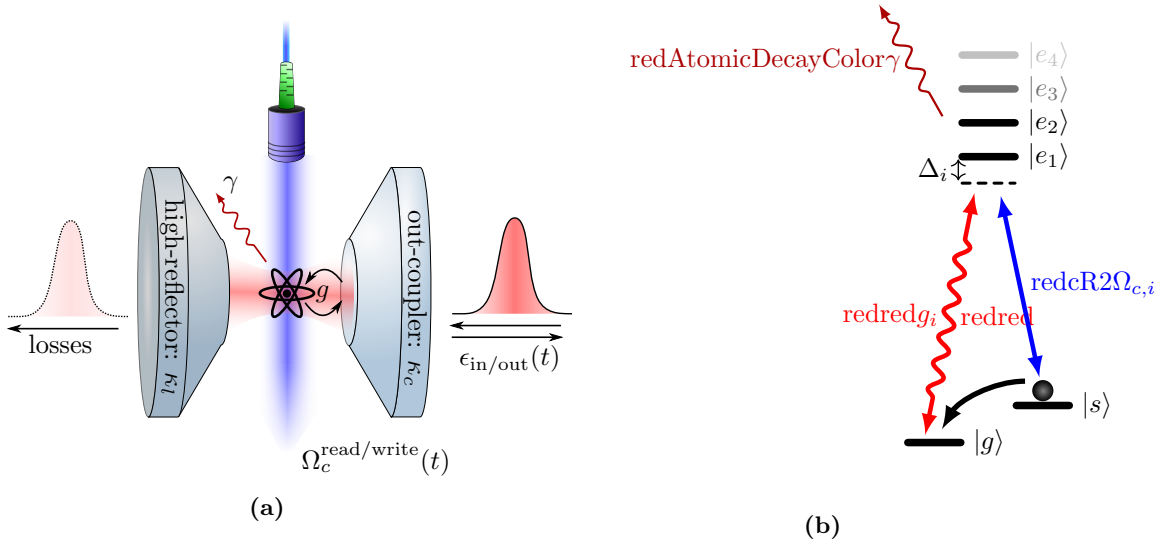

Figure 2.1.: Atom-cavity system. A single ^{87}Rb atom is trapped at the center of a high-finesse optical resonator. The resonator mode (red arrow in **b**) couples the ground state of the atom $|g\rangle$ to one or more excited states $|e_i\rangle$ with a single-photon detuning Δ_i and the light-matter interaction rate g_i. A macroscopic laser beam is aligned perpendicular to the cavity axis and couples one or more excited states with a second ground state $|s\rangle$ with Rabi frequency $\Omega_{c,i}(t)$ (blue arrow in **b**). The resonator mode and the macroscopic beam form a Λ-system which allows for the coherent absorption of a single photon from the temporal mode $\epsilon_{\text{in}}(t)$ impinged on the cavity mode by transporting the atomic population from $|g\rangle$ to $|s\rangle$. In the reversed process, a single photon can be emitted from the resonator system to the temporal mode $\epsilon_{\text{out}}(t)$.

to free-space modes resulting in atomic decay, as well as the in- and out-coupling of a single photon in the temporal mode $\epsilon_{\text{in/out}}(t)$, the system can be written in the master equation formalism with Lindblad operators [109, 110]

$$\frac{d}{dt}\hat{\rho} = \frac{1}{i\hbar}\left[\hat{H},\hat{\rho}\right] - \sum_k \underbrace{\frac{\gamma_k}{2}\left(\hat{c}_k^\dagger \hat{c}_k \hat{\rho} + \hat{\rho}\hat{c}_k^\dagger \hat{c}_k - 2\hat{c}_k \hat{\rho} \hat{c}_k^\dagger\right)}_{\hat{\mathcal{L}}(\hat{c})} . \tag{2.5}$$

Here, $\hat{\rho}$ is the density matrix of the system, $\hat{H}$ the Hamiltonian describing the unitary evolution of the system and the collapse operators $\hat{c}$ for non-unitary state changes which happen with the rate γ_k. For example, a collapse operator can describe the spontaneous decay from an excited state $|e\rangle$ to the ground state $|s\rangle$ with a rate γ, $\hat{c}_{es} = \frac{\gamma}{2}|s\rangle\langle e|$. Although finding an analytical solution for the system in this form is not the scope of this work, the master equation formalism will be used in Section 2.4.6 to perform numerical simulations of the dynamics of the system without further assumptions.

The focus of this chapter is to find the exact shape of the control field $\Omega_c^{\text{read}}(t)$ to produce a single photon in the temporal mode $\epsilon_{\text{out}}(t)$ with a single ^{87}Rb atom trapped in a high-finesse optical resonator in the intermediate coupling regime. As shown in [90] for the three-level system, the problem to solve is equivalent to finding the optimal control pulse $\Omega_c^{\text{write}}(t)$ to maximize the storage efficiency for a single incoming photon in the temporal mode $\epsilon_{\text{in}}(t)$. Before this problem is addressed in Section 2.3, existing formalisms are shortly discussed in the next sections.

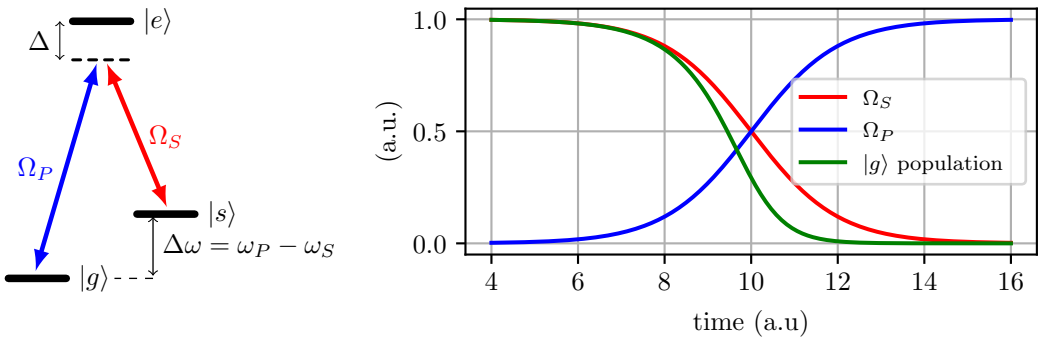

Figure 2.2.: Level structure of STIRAP scheme for a Λ-system. The ground state $|g\rangle$ is coupled to the excited state $|e\rangle$ by the so-called *Stokes* field with a single-photon detuning Δ and the Rabi frequency Ω_S while the excited state $|e\rangle$ is coupled to $|s\rangle$ by the *Pump* field with Rabi frequency Ω_P with the same single-photon detuning Δ. Since the detuning Δ is the same for both couplings, the system is in two-photon resonance such that the energy difference of the photons in the *Pump* and *Stokes* field matches the energy difference of $|g\rangle$ and $|s\rangle$. The graph shows the dynamics of the *Pump* and *Stokes* fields, as well as the population of the initial state $|g\rangle$ for the counterintuitive pulse sequence.

2.2.2. Stimulated Raman Adiabatic Passage

The Stimulated Raman Adiabatic Passage (STIRAP) [106, 107] is a well-known technique used for the coherent population transfer between two energy eigenstates $|g\rangle$ and $|s\rangle$ mediated by a third energy eigenstate $|e\rangle$. It was used in prior work [96] to describe the absorption and emission of a single photonic excitation. Within this semi-classical model, the three-level system is driven by two classical fields, the *Stokes* and *Pump* fields. Those fields couple the states $|g\rangle$ and $|s\rangle$ to the excited state $|e\rangle$ with single-photon detunings Δ_P and Δ_S, respectively. The system is considered to be in two-photon resonance, meaning that the energy difference of the photons in the *Pump* and *Stokes* fields exactly matches the difference of the energy levels $|g\rangle$ and $|s\rangle$. This is equivalent to having the same single-photon detuning for both couplings $\Delta_P = \Delta_S = \Delta$. The corresponding driving Hamiltonian in the rotating-wave approximation in the basis $(|g\rangle, |e\rangle, |s\rangle)$ is given by

$$H(t) = \hbar \begin{bmatrix} 0 & \frac{1}{2}\Omega_P(t) & 0 \\ \frac{1}{2}\Omega_P(t)^* & \delta & \frac{1}{2}\Omega_S(t) \\ 0 & \frac{1}{2}\Omega_S(t)^* & \Delta \end{bmatrix}_{(|g\rangle,|e\rangle,|s\rangle)} , \tag{2.6}$$

with the temporal profiles of the *Pump* and *Stokes* fields defined by $\Omega_P(t)$ and $\Omega_S(t)$, respectively. The presence of the Raman beams perturbs the system, and the eigenstates $|\Phi_i\rangle$ become

$$|\Phi_0(t)\rangle = \cos\chi(t)|g\rangle + \sin\chi(t)|s\rangle , \tag{2.7}$$
$$|\Phi_1(t)\rangle = \sin\chi(t)\sin\phi(t)|g\rangle + \cos\chi(t)|e\rangle + \cos\chi(t)\sin\phi(t)|s\rangle , \tag{2.8}$$
$$|\Phi_2(t)\rangle = \sin\chi(t)\cos\phi(t)|g\rangle - \sin\chi(t)|e\rangle + \cos\chi(t)\cos\phi(t)|s\rangle , \tag{2.9}$$

with the mixing angles

$$\chi(t) = \arctan\left(\frac{\Omega_P(t)}{\Omega_S(t)}\right) , \quad \phi(t) = \arctan\left(\frac{\sqrt{\Omega_P(t)^2 + \Omega_S(t)^2}}{\Delta}\right) . \tag{2.10}$$

In the STIRAP sequence, the system is initially prepared in the state $|g\rangle$, and the transfer starts by only applying a non-zero Rabi frequency for the *Stokes* beam, such that the

perturbed system remains in the initial state, $\frac{\Omega_P(t_0)}{\Omega_S(t_0)} = 0$ and $|\Phi_0\rangle = |g\rangle$. By smoothly inverting the ratio of the *Stokes* and *Pump* Rabi frequencies such that it approaches infinity at the end of the transfer, $\Omega_P(t_e)/\Omega_S(t_e) \to \infty$, the eigenstate $|\Phi_0(t)\rangle$ is transformed from $|g\rangle$ to $|s\rangle$. This adiabatically transfers the atomic population without populating the excited state $|e\rangle$. This protocol is called the *counterintuitive* STIRAP sequence, as it first couples the states $|s\rangle$ and $|e\rangle$ although the population is initialized in the state $|g\rangle$. Since the excited state is never populated, the system is not prone to atomic decay, allowing for unity transfer efficiency. By reversing the ordering of the Ω_P and Ω_S the population transfer can be reversed since this swaps merely the role of the states $|g\rangle$ and $|s\rangle$ and the driving amplitudes Ω_P, Ω_S. For the adiabatic evolution, it is necessary that the Rabi frequencies are sufficiently large and that the characteristic timescale τ for the overlap between Ω_P and Ω_S is not too small. A criterion for the adiabaticity of the process is given by [107]

$$\int \Omega_{P/S} \cdot dt \gg 1 \ , \tag{2.11}$$

which has to be fulfilled for both Raman pulses individually.

In case of cavity-assisted single photon storage, the intracavity field created by the impinging photon takes the role of the *Stokes* field while the *Pump* field is a classical control field aligned perpendicular to the cavity axis. In the reversed process used for photon retrieval, the vacuum field inside the empty cavity takes the role of the *Stokes* field resulting in a so-called Vacuum Stimulated Raman Adiabatic Passage (VSTIRAP) [111]. In both scenarios, the STIRAP protocol is not entirely applicable due to multiple reasons. The *Stokes* field created by the single-photon excitation inside the cavity is not necessarily intense enough to fulfill the adiabaticity criteria of the STIRAP. To allow efficient, fast transfers beyond the adiabatic limit the pulse shapes must be tailored for the specific situation to allow for *three-level superadiabatic quantum driving* [112]. More importantly, the *Stokes* field is not an intense classical light field, but a single quantum in the cavity mode. In the counterintuitive pulse sequence, the *Pump* field is left on until the transfer is completed. Here, the *Stokes* field created by the single photon becomes entangled with the atomic state and vanishes during the population transfer. Additionally, the STIRAP, as described above, does not provide a recipe to create or store photons with a specific complex-valued temporal envelope $\epsilon_{\text{out}}(t)$ and $\epsilon_{\text{in}}(t)$, respectively.

For the cavity parameters used in this work, $(g, \kappa, \gamma) = 2\pi\,(4.9, 2.75, 3.03)\,\text{MHz}$, the atomic decay rate γ is comparable to the light-matter interaction rate. Consequently, it cannot be treated as a perturbation and left out from the Hamiltonian (see Equation 2.6). It is well known that the efficiency of cavity based light-matter interaction is governed by the competition between g and the decay of the cavity field and the atomic population, but the STIRAP formalism fails to predict a realistic transfer efficiency.

2.2.3. Cavity-Assisted Single-Photon Absorption

As discussed above, the STIRAP protocol is not entirely applicable to achieve maximally efficient absorption of a single photon by a single atom inside an optical resonator. To optimize the absorption efficiency different approaches to model the cavity-assisted coherent absorption have been taken. In the work of Fleischhauer *et al.* [92], the control field is optimized for impedance matching to minimize the reflection of the photon. In this approach, it is assumed that the cavity is on resonance with the atomic transition ($\Delta = 0$),

that the cooperativity is high ($C \gg 1$) with

$$C := \frac{g^2}{\gamma\kappa} \ , \tag{2.12}$$

and that the pulse duration is large compared to the cavity decay rate κ and the decay γ of the excited state $|e\rangle$. In the work of Dilley *et al.* [91], the requirement of a large cooperativity is relaxed to $C > 1$, but atom-cavity resonance is still assumed. In contrast, in the work of Gorshkov *et al.* [90], atom-cavity resonance is not assumed, and the control field can account for arbitrary detunings. Further, instead of minimizing the reflection of the incoming photon, the transfer efficiency from $|g\rangle$ to $|s\rangle$ is optimized. This approach is favorable since a suppressed photon reflection does not necessarily result in a successful transfer to $|s\rangle$ but can also be a result of incoherent scattering of the atom. This approach assumes a cooperativity greater than 1, a smooth photon shape $\epsilon_{\text{in}}(t)$, the bad-cavity limit $\kappa \gg g$. This allows to adiabatically eliminate the excited state, given that the condition $\gamma T_{\text{char}} C \gg 1$ for the lower bound of the characteristic time T_{char} of the photon is met. It was numerically shown [108] that the control field found by Gorshkov *et al.* performs better than the control fields of Fleischhauer *et al.* and Dilley *et al.* concerning the transfer efficiency. Although the parameters of the atom-cavity system $(g, \kappa, \gamma) = 2\pi\,(4.9, 2.75, 3.03)\,\text{MHz}$ do not fulfill the assumptions of the bad-cavity limit, Gianelli *et al.* demonstrated numerically [108] that the control field performs well in this intermediate coupling regime, and that the model is applicable for the storage on a single atom although it was initially intended for a cold atomic ensemble. Since this model by Gorshkov *et al.* allows for a non-vanishing single-photon detuning and optimizes the actual transfer efficiency, it is the most promising one and will be extended to incorporate multiple excited states (see Section 2.3) to resemble a realistic experimental scenario.

2.2.3.1. The Three-Level Model by Gorshkov et al.

Here, the model by Gorshkov *et al.* [90] is briefly introduced before it is extended in the subsequent section. The starting point is the input-output relation for the cavity field given in Equation (2) of [90]

$$\epsilon_{\text{out}}(t) = \sqrt{2\kappa}\epsilon(t) - \epsilon_{\text{in}}(t) \ , \tag{2.13}$$

and the equations of motion in the Heisenberg picture and within the rotating-wave approximation for the expectation amplitude P of the excited state $|e\rangle$, the expectation amplitude S of the storage state $|s\rangle$ and the cavity population $\epsilon(t)$ given in Equations (3-6) in [90]:

$$\dot{\epsilon}(t) = -\kappa\epsilon(t) + igP + \sqrt{2\kappa}\epsilon_{\text{in}}(t), \tag{2.14}$$

$$\dot{P} = -\left(\gamma + i\Delta\right)P + ig\epsilon(t) + i\Omega_c(t)S, \tag{2.15}$$

$$\dot{S} = -i\Omega_c^*(t)P \ . \tag{2.16}$$

Here, γ is the atomic decay rate, g the cavity coupling rate, κ the cavity field decay rate and Δ the single-photon detuning between the cavity resonance and the atomic transition $|g\rangle \leftrightarrow |e\rangle$. This system of equations is solved and a reversible mapping between the temporal shape of the control pulse and the produced photon is retrieved:

$$\Omega_G(t) = \frac{-\gamma\,(C+1) + i\Delta}{\sqrt{2\gamma\,(C+1)}} \frac{\epsilon_{\text{in}}(t)}{\sqrt{\int_{t_0}^{t} \left|\epsilon_{\text{in}}(t')\right|^2 dt'}}$$

$$\times \exp\left(i\frac{\Delta}{2\gamma\,(C+1)} \cdot \ln\left(\int_{t_0}^{t} \left|\epsilon_{\text{in}}(t')\right|^2 dt'\right)\right) \ . \tag{2.17}$$

Additionally, the efficiency to create a photon inside the cavity mode is a function of the cooperativity of the atom-cavity coupling,

$$\eta = \frac{C}{1+C} \ . \tag{2.18}$$

Note that the efficiency is a constant quantity which does neither depend on the detuning between the cavity and the atomic transition nor the pulse shape. Also, the ground state $|g\rangle$ is not part of Equations (2.14-2.16). Since the model was initially designed for cold atomic ensembles, it is assumed that there is a bath of ground state population which can always be driven to an excited state by a single excitation in the cavity (see Equation 2.37). However, Gianelli *et al.* showed that this is still applicable to the single-atom scenario as long as there is only one or less excitations in the system. Loosely speaking, if there is an excitation in the cavity mode, the atom must be in its ground state and can be driven to the excited state. In the single-atom scenario, the validity of the model immediately breaks down once there is a second excitation present in the system because Equation 2.37 would transfer population from the cavity mode to the excited state although the atom is not necessarily in the ground state $|g\rangle$, that is coupled to the excited state by the cavity.

2.2.3.2. Decay Channel Decomposition

In the theoretical description of the cavity, κ is the rate of field decay from the cavity mode. It is well-known [113, 114] that this rate must be decomposed into multiple channels to differentiate between the coupling of photons through the cavity mirror into the desired free space mode and losses. Those losses consist of photons which are coupled out through the wrong cavity mirror and absorption and scattering losses by the mirror substrate. This leads to the natural definition of the escape efficiency [114],

$$\eta_{\mathrm{esc}} = \frac{\kappa_c}{\kappa} \ , \tag{2.19}$$

also referred to as output directionality [86], where κ_c is the coupling rate through the output-coupler mirror, and κ_l are all other loss channels such that the total losses from the cavity are given by

$$\kappa = \kappa_c + \kappa_l \ . \tag{2.20}$$

The integration of the modified κ in the input-output relation 2.13 and the differential equation of the intra-cavity field 2.14 is straightforward: The two terms associated with the interface between the free-space mode and the cavity mode must be modified,

$$\kappa \to \eta_{\mathrm{esc}}\kappa \ , \tag{2.21}$$

while the term which represents the decay of the intra-cavity field is maintained,

$$\epsilon_{\mathrm{out}}(t) = \sqrt{2\eta_{\mathrm{esc}}\kappa}\epsilon(t) - \epsilon_{\mathrm{in}}(t) \ , \tag{2.22}$$

$$\dot{\epsilon}(t) = -\kappa\epsilon(t) + igP + \sqrt{2\eta_{\mathrm{esc}}\kappa}\epsilon_{\mathrm{in}}(t) \ . \tag{2.23}$$

This decomposition only affects the conversion efficiency between the cavity mode and the free-space mode and thus results in a well-known rescaling of the production efficiency with the escape efficiency [86],

$$\eta \to \eta_{\mathrm{esc}}\eta = \eta_{\mathrm{esc}}\frac{C}{C+1} \ . \tag{2.24}$$

Gianelli *et al.* [108] recently demonstrated this result explicitly for the Gorshkov model.

2.2.4. Photonic Temporal Mode Reconstruction

The temporal mode $\epsilon_{\text{out}}(t)$ of a single photon is a complex-valued function which can be experimentally accessed by a homodyne technique, which utilizes quantum interference of the photonic mode with a known reference field [115, 116]. Here, a technique developed by Morin *et al.* [117] is presented which extracts the individual temporal mode components and their amplitude from a series of quadrature measurements. This technique not only allows the verification of the purity of a photonic mode but also enables its reconstruction.

By repeatedly interfering the emitted temporal mode with a known local oscillator field on a photodiode, a set of k quadrature signals $x_k(t)$ are acquired. From the autocorrelation-function

$$\langle x_k(t)x_k(t')\rangle_k = K(t,t')\,\sigma_0^2 \ , \tag{2.25}$$

the kernel $K(t,t')$ normalized by the fluctuations of the vacuum field σ_0^2 can be extracted. A temporal photonic mode $f(t)$ is defined such that it is created by the operator $\hat{a}^\dagger_{f(t)}(t)$, which results from integrating the creation operator for a photonic excitation $\hat{a}^\dagger$ scaled with $f(t)$,

$$\hat{a}^\dagger_{f(t)} = \int f(t)\hat{a}(t)^\dagger dt \ . \tag{2.26}$$

For a single-photon state $|1\rangle$ with the corresponding photonic mode $f(t)$, the kernel of the autocorrelation-function is given by

$$K(t,t') = \delta(t,t') + 2\Re\left(f(t)f^*(t)\right) \ , \tag{2.27}$$

where the first term containing the δ-operator corresponds to the vacuum contributions of all other modes. Consequently, a mixed photonic state with $\bar{n} \leq 1$ average photons can be written as

$$K(t,t') = \delta(t,t') + 2\bar{n}\Re\left(f(t)f^*(t')\right) \ . \tag{2.28}$$

If the photonic mode $f(t)$ is a real-valued function, it is also an eigenfunction of the kernel $K(t,t')$ with the eigenvalue $2\bar{n}+1$. It becomes clear that if the temporal mode is filled by a single-photon state mixed with vacuum, the kernel has exactly one eigenvalue larger than one, with the corresponding photonic mode f as an eigenfunction. To extend this rather simple method to complex-valued photonic modes, the expression for the kernel (see Equation 2.27) can be rewritten to

$$K(t,t') = \delta(t,t') + 2\Re(f(t))\Re(f(t')) + 2\Im(f(t))\Im(f(t')) \ . \tag{2.29}$$

Using the fact that the $K(t,t')$ is symmetric by definition and Mercers theorem, for a temporal mode function,

$$f(t) = |f(t)|e^{i\phi(t)} \ , \tag{2.30}$$

the kernel has two eigenfunctions $f_{1,2}$ with eigenvalues $2n_{1,2}+1 = k_{1,2}$,

$$f_1(t) = \frac{n_1}{n_1+n_2}|f(t)|\cos\left(\phi(t)+\phi_0\right) \ , \tag{2.31}$$

$$f_2(t) = \frac{n_2}{n_1+n_2}|f(t)|\sin\left(\phi(t)+\phi_0\right) \ . \tag{2.32}$$

Here, one eigenfunction corresponds to the real and the other to the imaginary part of the complex photonic mode, respectively. Each part is weighted by the photon numbers associated with the eigenvalues

$$f(t) = \frac{1}{\sqrt{n_1 + n_2}} \left(\sqrt{n_1} f_1(t) + i\sqrt{n_2} f_2(t)\right) \ . \tag{2.33}$$

Note that there is an ambiguity concerning the roles of the two eigenfunctions. This can be lifted by applying an additional measurement with a detuned local oscillator. However, here this method is used to verify the suppression of the complex part of the temporal mode for a known shape. Therefore, prior knowledge about the temporal mode can be applied to efficiently lift the ambiguity without further measurements. See Section 2.5.3 for the application of this method to experimental data.

2.3. Multi-Level Model

In this section, the model by Gorshkov *et al.* is extended to incorporate multiple excited states to achieve a better resemblance between the theoretical model and the experimental conditions. First, the equation system presented in the previous section is extended to include the coupling to multiple excited states. The assumptions used in [90], which are inherited to derive an analytical solution are also discussed. Subsequently, the dynamics of the atomic population and the cavity mode are solved, and an expression for the efficiency is derived. Finally, the mapping between the control pulse and the produced photon is identified.

Note that the extension derived in this section is kept general such that it applies to various quantum systems besides the one used throughout this thesis. The impact of the incorporation of multiple excited states depends on the actual system and will be discussed in the subsequent section, in which the theory is applied to the specific system used for light-matter interfacing in the context of this work.

2.3.1. Equation system

To add multiple excited states into the differential equation system, the coupling of the cavity mode to the N individual states must be incorporated into the equation of motion of the cavity population (see Equation 2.22). The equation of motion of the excited state (see Equation 2.15) is extended to a set of N differential equations. The equation for the population dynamics of the storage state S must incorporate the couplings to all excited states. Finally, the differential equation for the input-output relation remains unchanged. The N+3 differential equations for the state and cavity populations become

$$\epsilon_{\text{out}}(t) = \sqrt{2\eta_{\text{esc}}\kappa}\epsilon(t) - \epsilon_{\text{in}}(t) \ , \tag{2.34}$$

$$\dot{\epsilon}(t) = -\kappa\epsilon(t) + \sum_i \left(i g_i P_i\right) + \sqrt{2\eta_{\text{esc}}\kappa}\epsilon_{\text{in}}(t) \ , \tag{2.35}$$

$$\dot{P}_i = -\left(\gamma + i\delta_i\right) P_i + i g_i \epsilon(t) + i\Omega_{c,i}(t) S \ , \tag{2.36}$$

$$\dot{S} = -i \sum_i \left(\Omega^*_{c,i}(t) P_i\right) . \tag{2.37}$$

After the application of suitable assumptions, this system of equations will be solved throughout this section.

2.3.1.1. Assumptions

To find an analytical solution for the dynamics of the system, two significant assumptions are inherited from [90]. Firstly, it is assumed that the photonic shapes of the produced and incoming photon $\epsilon_{\text{in/out}}(t)$ and the corresponding control Rabi frequency $\Omega_{c,i}(t)$ are smooth. According to [90], this guarantees that the population of the excited states is small at all times and changes slowly such that P_i can by adiabatically eliminated

$$\dot{P}_i \to 0 \ . \tag{2.38}$$

Secondly, the bad-cavity limit (weak coupling regime),

$$\kappa \gg g \ , \tag{2.39}$$

is applied which allows the adiabatic elimination of the time derivative of the cavity field,

$$\dot{\epsilon}(t) \to 0 \ . \tag{2.40}$$

This step seems to be not applicable to the system used throughout this thesis. In the context of a collaboration with the group of Giovanna Morigi, it was numerically verified that the predictions of Gorshkov hold true even for resonators within the intermediate coupling regime ($g \approx \kappa$) [108]. Those results can be understood by a comparison of time scales: For the production of photons with a temporal extent in the order of microseconds, the cavity decay rate $\kappa \approx 3\,\text{MHz}$ is fast compared to the cavity population rate. Hence, at any time the cavity is only weakly populated, and the population is only slowly changing since the photons are assumed to be smooth. Therefore, it is reasonable to neglect $\dot{\epsilon}(t)$.

After the application of both eliminations, the differential equation system reduces to,

$$\epsilon_{\text{out}}(t) = \sqrt{2\eta_{\text{esc}}\kappa}\epsilon(t) - \epsilon_{\text{in}}(t) \ , \tag{2.41}$$

$$\epsilon(t) = \frac{1}{\kappa}\left(\sum_i \left(ig_i\hat{P}_i\right) + \sqrt{2\eta_{\text{esc}}\kappa}\epsilon_{\text{in}}(t)\right) \ , \tag{2.42}$$

$$P_i = \frac{1}{(\gamma + i\delta_i)}\left(ig_i\epsilon(t) + i\Omega_{c,i}(t)S\right) \qquad \forall i \in [1,\ldots,N] \ , \tag{2.43}$$

$$\dot{S} = -i\sum_i \left(\Omega^*_{c,i}(t)P_i\right) \ , \tag{2.44}$$

and it can be analytically solved. The impact of the applied assumptions is numerically tested in Section 2.4.5.1.

2.3.2. Population Dynamics

In this section, the equations of motion for the storage state S, the excited states P_i, and the cavity mode $\epsilon(t)$ are solved.

2.3.2.1. Excited State Dynamics

Analogous to the derivation of the three-level model [90], the case of photon production is considered such that there is no incoming photonic field coupled to the cavity mode,

$$\epsilon_{\text{in}}(t) = 0 \ . \tag{2.45}$$

This reduces the Equation 2.42 and 2.43 to a set of N coupled linear equations which are only a function of the population of the storage state S and the Rabi driving profile $\Omega_{c,i}(t)$. In matrix representation, the system can be expressed as

$$\underbrace{\begin{pmatrix} \alpha_1 & \beta_{1,2} & \beta_{1,3} & \dots & \beta_{1,N} \\ \beta_{2,1} & \alpha_2 & \beta_{2,3} & \dots & \beta_{2,N} \\ \beta_{3,1} & \beta_{3,2} & \alpha_3 & \dots & \beta_{3,N} \\ \vdots & \vdots & \vdots & \ddots & \vdots \\ \beta_{N,1} & \beta_{N,2} & \alpha_3 & \dots & \alpha_N \end{pmatrix}}_{\boldsymbol{A}} \underbrace{\begin{pmatrix} P_1 \\ P_2 \\ P_3 \\ \vdots \\ P_n \end{pmatrix}}_{\vec{P}} = i \underbrace{\begin{pmatrix} c_{s,1} \\ c_{s,2} \\ c_{s,3} \\ \vdots \\ c_{s,N} \end{pmatrix}}_{\vec{c}_s} \Omega_c(t) S \ , \tag{2.46}$$

with the abbreviations

$$\alpha_i = \gamma\,(1 + C_i) + i\Delta_i \qquad \beta_{i,j} = \frac{g_j g_i}{\kappa} \ , \tag{2.47}$$

and the normalized Rabi frequencies and the definition of the state-specific cooperativity

$$\Omega_{c,i}(t) = c_{s,i}\Omega_c(t) \ , \quad C_i = \frac{g_i^2}{\gamma\kappa} \ . \tag{2.48}$$

See (A.1) for further details. Given that the matrix $\boldsymbol{A}$ has the full rank such that it can be inverted, a solution for P can be found which has the general form

$$\vec{P} = i \underbrace{\boldsymbol{A}^{-1}\vec{c}_s}_{\vec{Q}} \Omega_c(t) S(t) \ . \tag{2.49}$$

Note that the time-independent vector $\vec{Q} = \vec{Q}(g_i, c_{s,i}, \Delta_i, \gamma, \kappa)$ includes all the information about the specifics of the system, including the cavity-coupling strengths g_i, the single-photon detunings Δ_i, the coupling strengths of the control laser $c_{s,i}$ and the atomic and cavity decay rates γ and κ, respectively.

2.3.2.2. Population Dynamics of the Storage State

With the solution for the population dynamics of the excited states, the dynamics of the storage state can be solved. By inserting the solution P in the equation of motion for the storage state S (see Equation 2.44) a linear differential equation emerges,

$$\dot{S}(t) = \underbrace{\vec{c}_s \cdot \vec{Q}}_{K \in \mathbb{C}} |\Omega_c(t)|^2 S(t) \ . \tag{2.50}$$

Note that all properties of the system are exclusively contained in the one-dimensional complex time-independent factor $K(\Delta_i, c_{g,i}, c_{s,i})$. Therefore, the resulting differential equation is of the same form for all systems independent of the specific configuration and number of states considered. Consequently, the structure of the differential equation must also resemble the structure of the three-level system discussed in [90], and the same solution approach can be applied,

$$S(t) = S(t_0) \exp\left(-K \int_{t_0}^{t} |\Omega(t')|^2 dt'\right) \tag{2.51}$$

$$= \exp\left(-K h(t)\right) \ , \tag{2.52}$$

with an initially entirely populated storage state $S(t_0) = 1$ and the integral of the applied Rabi driving intensity

$$h(t) := \int_{t_0}^{t} |\Omega(t')|^2 dt' \ . \tag{2.53}$$

As can be seen in the solution for S, the population of the storage state is entirely depleted if a control pulse with a sufficiently large pulse area is applied.

2.3.2.3. Cavity Free-Field Mode Dynamics

The dynamics of the free-field mode coupled to the cavity can directly be expressed with the solutions found for S and P,

$$\begin{aligned} \epsilon_{\text{out}}(t) &= \sqrt{2\eta_{\text{esc}}\kappa}\,\epsilon(t) \\ &= i\sqrt{2\eta_{\text{esc}}\kappa}\sum_i g_i P_i \\ &= \underbrace{i\sqrt{2\eta_{\text{esc}}\kappa}\,\vec{g}\cdot\vec{Q}}_{L\in\mathbb{C}}\,\Omega_c(t)\exp\left(-Kh(t)\right) \ . \end{aligned} \tag{2.54}$$

Again, the one-dimensional complex constant $L = L(\Delta_i, C, \eta_{\text{esc}}\gamma, c_{g,i}, c_{s,i})$ contains all the details of the physical system.

At this point, an analytical expressions for the population dynamics of the full system is derived. In the subsequent part of this section, the photon production efficiency and the mapping between the control Rabi frequency and the produced photon are investigated.

2.3.3. Photon Production Efficiency

The photon emission efficiency is defined as the probability to retrieve a photon in the free-field mode coupled to the cavity, that was emitted by the atom. It is calculated by integrating the retrieved energy from the cavity mode [90],

$$\begin{aligned} \eta_R &= \int_{t_0}^{\infty} |\epsilon_{\text{out}}(t)|^2 dt = |L|^2 \int_{t_0}^{\infty} \partial_t h(t)\cdot e^{-2\Re(K\cdot h(t))} dt \\ &= \frac{-|L|^2}{2\Re(K)}\left[e^{-2Kh(t\to\infty)} - e^{-2Kh(t_0)}\right] \\ \eta_R &\approx \frac{|L|^2}{2\Re(K)} \ , \end{aligned} \tag{2.55}$$

for a sufficiently large pulse area with the control pulse which does not start before t_0,

$$h(t_0) = 0 \quad \text{and} \quad h(t\to\infty) \gg 1 \ . \tag{2.56}$$

For the simple case of a three-level system with only one excited state (N=1) this expression resembles the efficiency identified by Gorshkov *et al.* [90] scaled by the escape efficiency (see Section 2.2.3.2),

$$\eta_R^{(N=1)} = \eta_{\text{esc}}\frac{C_1}{C_1+1} \ . \tag{2.57}$$

In this scenario, the efficiency is only a function of the cooperativity C_1. However, for more complex systems including multiple excited levels, the population transfer can be mediated by multiple excited levels if multiple Λ-systems are present in the configuration. Consequently, the efficiency becomes a function of the single-photon detunings due to the interfering excitation paths. Examples for this dependency can be found in Section 2.4.2 where the theory is applied to the atom-cavity system used throughout this thesis.

2.3.4. Photon Shape Control

With the dynamics of the storage state and the excited states and the photon production efficiency η, the mapping between the created photonic mode $\epsilon_{\text{out}}(t)$ and the time-dependent Rabi frequency $\Omega_c(t)$ can be extracted using Equation 2.54. With the normalized retrieved mode,

$$e(t) = \sqrt{\eta_R}^{-1}\epsilon_{\text{out}}(t) \ , \tag{2.58}$$

the mapping is given by

$$\Omega_c(t) = \frac{e(t)}{\sqrt{2\Re(K)\int_t^\infty |e(t')|^2 dt'}} \exp\left(-i\frac{\Im(K)}{2\Re(K)}\ln\left(\int_t^\infty |e(t')|^2 dt'\right)\right) \ . \tag{2.59}$$

See Appendix A.2 for more details. The complex control shape $\Omega_c(t)$ allows the emission of an arbitrary smooth photon shape $\epsilon_{\text{out}}(t)$ with an efficiency $\eta(\delta) = \frac{|L|^2}{2\Re(K)}$ which is a function of the single-photon detunings Δ_i. Note that the mapping between photon shape $\epsilon_{\text{out}}(t)$ and the Rabi frequency Ω_c is reversible,

$$\epsilon_{\text{out}}(t) = \Omega_c(t) L \exp\left(-K\int_{t_0}^t \left|\Omega_c(t')\right|^2 dt'\right) \ , \tag{2.60}$$

and gives access to the temporal mode created by the application of an arbitrary control pulse. The reverse mapping will be useful when the impact of neglecting coupled excited states will be discussed in Section 2.4.3.

2.3.5. Photon Absorption

The coherent absorption of an incoming photon can be described as the time-reserved process of the photon emission [90]. The time-reversal relation between photon emission and absorption has been formally proven for the three-level system in [90] and is not separately demonstrated here for the multi-level system. Using the transformations

$$\epsilon_{\text{out}}(t) \to \epsilon^*_{\text{out}}(-t) = \epsilon_{\text{in}}(t) \ , \tag{2.61}$$

$$\Omega_c(t) \to \Omega^*_c(-t) = \Omega_c^{\text{write}}(t) \ , \tag{2.62}$$

the control pulse Rabi frequency for photon storage can be directly obtained,

$$\Omega_c^{\text{write}}(t) = \frac{\epsilon_{\text{in}}(t)}{\sqrt{2\Re(K)\int_0^t |\epsilon_{\text{in}}(t')|^2 dt'}} \exp\left(i\frac{\Im(K)}{2\Re(K)}\ln\left(\int_0^t |\epsilon_{\text{in}}(t')|^2 dt'\right)\right) . \tag{2.63}$$

It directly follows from the time-reversal argument that the storage efficiency equals the retrieval efficiency for an incoming photon which is perfectly coupled to the cavity mode.

2.3.6. Conclusion

In this section the model by Gorshkov *et al.* for the coherent absorption and emission of a single photon from a single atom was extended to incorporate an arbitrary number of excited states. No further assumptions have been made, and the derivation of the model was kept general such that it can be applied to various quantum systems. The impact of the coupling to multiple excited states is investigated in the next section where the model is applied to the atom-cavity system used throughout this thesis.

2.4. Application to a Specific Atom-Cavity System

In the previous section, a generalization of the formalism of Gorshkov *et al.* was derived which allows the incorporation of multiple excited states. In this section, the formalism is applied to incorporate the full relevant level structure of the ^{87}Rb atom for the cavity-assisted photon production and storage process (see Section 2.2.1).

At first, the level scheme and the cavity used for the storage of a single photon is introduced. The significance of the additional coupled excited states is then demonstrated regarding the predicted efficiency and the temporal modes of photons produced from the atom-cavity system. Further, the impact of an incorrectly tailored control pulse on the photon storage efficiency is investigated.

2.4.1. Level Scheme and Atom-Cavity System

The cavity system used throughout this thesis has the following characteristic parameters:

$$(g, \kappa, \gamma) = 2\pi\,(4.9, 2.75, 3.03)\,\mathrm{MHz}\ . \tag{2.64}$$

An important property of the cavity is its pair of asymmetric mirrors. The *coupler* mirror has a transmission of $T_{\mathrm{oc}}{\approx}101\,\mathrm{ppm}$ and the *high-reflector* mirror has a transmission of $T_{\mathrm{hr}}{\approx}4\,\mathrm{ppm}$. The resulting directionality is an important feature of this light-matter interface since it allows for the predominant coupling to one specific free-space mode. The cavity losses κ are the sum of the output-coupling rate through the coupler-mirror $\kappa_c{\approx}2\pi\,2.42\,\mathrm{MHz}$ and the residual losses $\kappa_l{\approx}2\pi\,0.33\,\mathrm{MHz}$due to the coupling through the high-reflector mirror and absorption and scattering losses. This yields an escape efficiency of $\eta_{\mathrm{esc}}{\approx}0.88$. For more details on the resonator system, please refer to previous research reports of project performed on the same experimental apparatus [118].

In the protocol used for photon-emission and photon-absorption, the σ^+-mode of the cavity is near resonant to the

$$|F{=}1,\ m_F{=}0\rangle \leftrightarrow \left|F'{=}1, m_F{=}1\right\rangle \tag{2.65}$$

transition, with a single-photon detuning between the atomic resonance and the cavity mode of Δ_1. The classical π-polarized control beam couples the

$$|F{=}2,\ m_F{=}1\rangle \leftrightarrow \left|F'{=}1, m_F{=}1\right\rangle \tag{2.66}$$

transition with the same single-photon detuning Δ_1, forming a Λ-system in two-photon resonance. Both the cavity mode and the classical beam also couple the corresponding

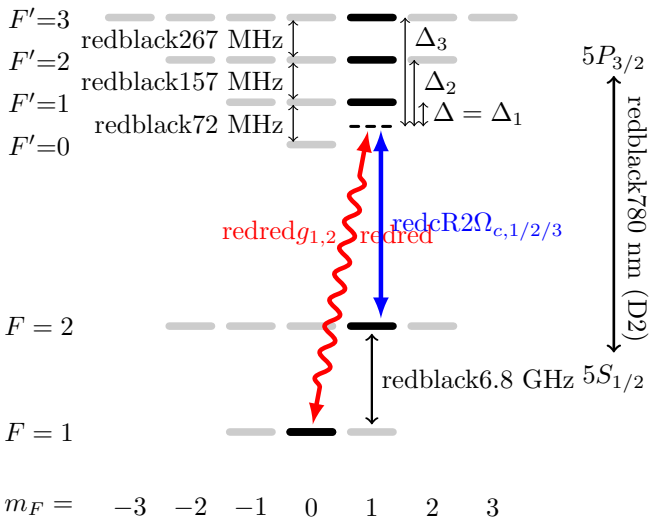

Figure 2.3.: Atomic-level structure for the photon production and storage processes. The atomic population is initialized in the $|F{=}2,\, m_F{=}1\rangle$ ground state. An intense control beam is aligned perpendicular to the quantization axis of the cavity mode and couples the initial state to the three excited states $|F'{=}1/2/3, m_F{=}1\rangle$, with Rabi frequencies $\Omega_{C,1/2/3}$ and single-photon detunings $\Delta_{1/2/3}$. The first two of these excited states are coupled to the target ground state $|F{=}1,\, m_F{=}0\rangle$ via the cavity mode. Thus a total of two Λ-systems are formed when both the $|F'{=}1\rangle$ and $|F'{=}2\rangle$ excited states are considered. The photon absorption process is considered to be the time-reversal of the emission process.

ground states to the $|F'{=}2, m_F{=}1\rangle$ state, with a single-photon detuning $\Delta_2{=}\Delta_1{-}157\,\mathrm{MHz}$, such that a second Λ-system is formed. Additionally, the control beam couples the

$$|F{=}2,\ m_F{=}1\rangle \leftrightarrow \left|F'{=}3, m_F{=}1\right\rangle \tag{2.67}$$

transition, but due to the dipole selection rules the cavity mode does not couple this excited state to the $|F{=}1\rangle$ ground state. Therefore, this excited state is not closing a third Λ-system. The normalized Clebsch-Gordan coefficients of the individual transitions are listed in Table 2.1. For the photon emission protocol, the atomic population is initialized in the $|F{=}2,\, m_F{=}1\rangle$ or in the $|F{=}1,\, m_F{=}0\rangle$ state for photon storage, respectively.

In the notation of the theory derived in the previous section, the relevant states can be identified as

$$|s\rangle = |F{=}2,\ m_F{=}1\rangle\ , \tag{2.68}$$
$$|e_1\rangle = \left|F'{=}1, m_F{=}1\right\rangle\ , \tag{2.69}$$
$$|e_2\rangle = \left|F'{=}2, m_F{=}1\right\rangle\ , \tag{2.70}$$
$$|e_3\rangle = \left|F'{=}3, m_F{=}1\right\rangle\ . \tag{2.71}$$

The corresponding level scheme is depicted in Figure 2.3. For the rest of this section, the single-photon detuning is defined as the detuning to the $\left|5^2P_{3/2}, F'{=}1\right\rangle$ manifold,

$$\Delta := \Delta_1\ . \tag{2.72}$$

Note that the σ^--mode of the cavity creates a symmetric coupling scenario with the $m_F{=}{-}1$ states. This aspect is crucial for the storage of a polarization qubit as it will be discussed in the next chapter. However, for now only the σ^+-mode is considered.

Table 2.1.: Normalized Clebsch-Gordan coefficients for the relevant transitions for the photon storage and production protocol.

	$\|F{=}1,\, m_F{=}0\rangle$	$\|F{=}2,\, m_F{=}1\rangle$
$\|F'{=}1, m_F{=}1\rangle$	$c_{g,1} = \sqrt{\frac{5}{24}}$	$c_{s,1} = \sqrt{\frac{1}{40}}$
$\|F'{=}2, m_F{=}1\rangle$	$c_{g,2} = \sqrt{\frac{1}{8}}$	$c_{s,2} = \sqrt{\frac{1}{24}}$
$\|F'{=}3, m_F{=}1\rangle$	$c_{g,3} = 0$	$c_{s,3} = \sqrt{\frac{4}{15}}$

2.4.2. Photon Production Efficiency

In the scenario investigated by Gorshkov *et al.* where only one excited state is taken into account, the photon production efficiency is constant and can be equated merely from the cooperativity (see Section 2.2.3). The cavity parameters used in this thesis yields the cooperativity $C_1{\approx}3.13$ for the transition $|g\rangle \leftrightarrow |e_1\rangle$. The resulting photon production efficiency is

$$\eta^{(N=1)} = \eta_{\text{esc}} \frac{C_1}{C_1 + 1} \approx 66\% \quad \text{with} \quad \eta_{\text{esc}} \approx 0.872 \; . \tag{2.73}$$

Once the second excited state $|e_2\rangle$ is considered - which also forms a separate λ-system with $|g\rangle$ and $|s\rangle$ - the transfer efficiency becomes a function of the single-photon detuning Δ due to the interference of the two competing transfers. Since all involved Clebsch-Gordan coefficients are positive (see Table 2.1), the population transfers interfere destructively if the cavity frequency is in between the resonance frequencies of the $|g\rangle \leftrightarrow |e_1\rangle$ and the $|g\rangle \leftrightarrow |e_2\rangle$ transition, such that $\text{sgn}(\Delta_1) \neq \text{sgn}(\Delta_2)$. The destructive interference of the 4-level system results in a dip of the storage efficiency for a single-photon detuning in between the $\left|5^2P_{3/2}, F'{=}1\right\rangle$ and $\left|5^2P_{3/2}, F'{=}2\right\rangle$ transition, as it can be seen in Figure 2.4 (shown in orange). If the atom-cavity detuning is not in between the two optical transitions, the transfers interfere constructively, and the light-matter interface becomes more efficient compared to the 3-level scenario with only one excited state mediating the transfer. As discussed above, the third excited state $|e_3\rangle = |F'{=}3, m_F{=}1\rangle$ does not form a λ-scheme. Nevertheless, it affects the efficiency by contributing an additional decay channel to the system: Although off-resonant, the control field populates the state, which can incoherently decay with the rate γ as expressed in the differential equation system 2.15.

Within the theory, only coherent processes contribute to the emission (or absorption) of a photon and every decay is a loss of the excitation. If the single-photon detuning is chosen such that the control field becomes resonant with the $|s\rangle \leftrightarrow |e_3\rangle$ transition, the atomic population is predominantly transported to the $|e_3\rangle$ state and lost over the excitation decay channel (shown in green, Figure 2.4). In the regime where the single-photon detuning brings one of the other excited states close to resonance, the population transfer is efficiently mediated by the two excited states forming a Λ-system and the third excited state $|e_3\rangle$ does not significantly affect the efficiency. In the regime of high single-photon detunings, the difference in the detunings of the individual states becomes neglectable such that all states are, up to the Clebsch-Gordan coefficients, equally coupled by the control beam. Therefore, an excitation of the $|e_3\rangle$ becomes more likely again. For this reason, the transfer efficiency for the 5-level system has a local maximum as shown in Figure 2.4.

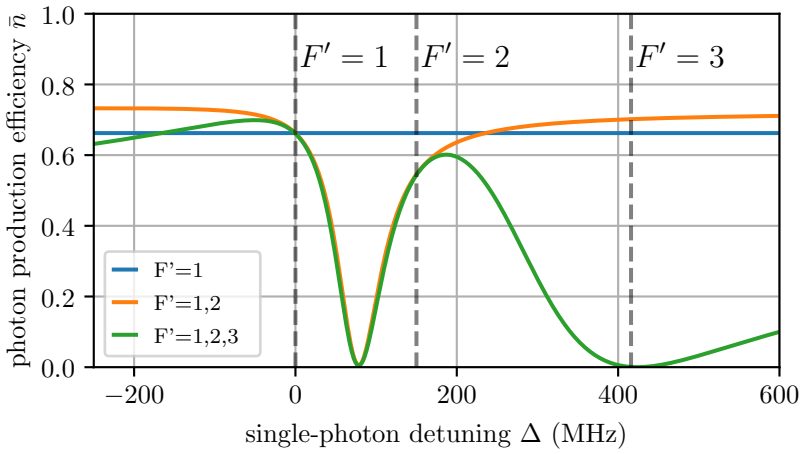

Figure 2.4.: Predicted photon production efficiency over the single-photon detuning. The photon production efficiency is evaluated as a function of the single-photon detuning Δ. The different curves correspond to three different models which incorporate either only one excited state ($|F'{=}1\rangle$), two excited states ($|F'{=}1,2\rangle$) or all three coupled states ($|F'{=}1,2,3\rangle$). The dashed lines mark the spectral position of the $|F'{=}1\rangle$ and $|F'{=}2\rangle$ transitions, meaning that for this single-photon detuning the cavity system is in resonance with the atomic $\left|5^2S_{1/2}, F{=}1\right\rangle \mapsto \left|5^2P_{3/2}, F'{=}1/2/3\right\rangle$ transitions.

Note that within the theory, every incoherent decay process removes the excitation from the system such that only coherent processes contribute to the transfer efficiency. In the physical reality, the population can decay back to a state which then contributes to the photon production process. The effect of those second-order processes will be investigated in a later Section (see Section 2.4.6).

2.4.3. Photon Shapes

In the generalized theory, a reversible mapping between the produced photon $\epsilon_{\text{out}}(t)$ and the control Rabi frequency $\Omega_c(t)$ was identified (see Equations 2.60, 2.59). For a non-vanishing single-photon detuning between the atomic resonance and the cavity mode, the contributions of additional Λ-systems change the effective coupling strength due to an interference of the driving paths. This interference ultimately affects the Rabi frequency and therefore the photonic shape that is produced or stored.

Here, the impact of the contributions of the additional excited states is probed by utilizing the mapping between the control pulse and the produced photonic shape. To this extent, the following notation is used:

$$\Omega_{c,\Delta}^{(F')}\left(\epsilon_{\text{out}}(t)\right) \tag{2.74}$$

defines the control pulse to generate the photonic shape $\epsilon_{\text{out}}(t)$ in the theoretical system which incorporates the excited states F' and a single-photon detuning Δ. Analogously,

$$\epsilon_{\text{out},\Delta}^{(F')}\left(\Omega_c(t)\right) \tag{2.75}$$

is the photonic mode which is emitted when $\Omega_c(t)$ is applied to the theoretical system with the excited states F'. For clarity,

$$\Omega_{c,\Delta}^{(F')}\left(\epsilon_{\text{out},\Delta}^{(F')}\left(\Omega_c(t)\right)\right) = \Omega_c(t), \quad \epsilon_{\text{out},\Delta}^{(F')}\left(\Omega_{c,\Delta}^{(F')}\left(\epsilon_{\text{out}}(t)\right)\right) = \epsilon_{\text{out}}(t) \tag{2.76}$$

are both identities. For now, it is assumed that

$$\Omega_{c,\Delta}^{(F'=1,2,3)}\left(\epsilon_{\mathrm{out}}(t)\right) \tag{2.77}$$

generates the correct control pulse since all relevant excited states are considered and

$$\epsilon_{\mathrm{out},\Delta}^{(F'=1,2,3)}\left(\Omega_c(t)\right) \tag{2.78}$$

correctly predicts the mode which is emitted when $\Omega_c(t)$ is applied to the system (see Section 2.5.3 for an experimental test of this assumption). To probe the deformation of the produced photon by incorrectly neglecting the additional excited states,

$$\epsilon_{\mathrm{out},\Delta}^{(F'=1,2,3)}\left(\Omega_{c,\Delta}^{(F'=1)}\left(\epsilon_{\mathrm{out}}(t)\right)\right) \tag{2.79}$$

is evaluated and shown in Figure 2.5 for a hyperbolic secant photon (top row) and a double hyperbolic secant photon (bottom row), for different single-photon detunings Δ. The amplitude of the resulting photons is shown on a) and c) and the time-derivation of the phase angle on b) and d). In the regime of constructive interference between the two Λ-systems ($\Delta < 0$), the Rabi frequency $\Omega_c(t)$ is enhanced. In this case, the control pulse generated for the three-level system is too intense and consequently, the photon is produced too fast resulting a deformed shape. Analogously, in the regime of destructive interference ($0<\Delta<157\,\mathrm{MHz}$), the intensity of the control pulse is too weak resulting in a delayed and deformed photon. For a vanishing single-photon detuning the system converges against the system with only one excited state on resonance, and the produced shape matches the intended target shape. The effect becomes even more pronounced for a double secant hyperbolic shape as it can be seen in Figure 2.5c.

Besides the effect on the photonic intensity profile, the coupling of the control pulse to the excited states induces light-shifts of the atomic states and thereby shifting the system out of the two-photon resonance condition. In the case of the photon-production protocol, this shift imprints an additional phase term onto the temporal mode. This leads to a time-dependent shift of the center frequency of the photon. In Figure 2.5b and 2.5d this chirp is shown for various single-photon detunings for the secant hyperbolic shaped photon and the double secant hyperbolic one, respectively. Note that for larger single-photon detunings, this frequency chirp is significant with regard to the bandwidth of the cavity.

When all relevant atomic states are incorporated in the control pulse, the effects are compensated by adjusting the intensity and dynamically shifting the frequency of the control pulse to maintain the two-photon resonance condition. The control pulses for the three- ($F' = 1$), four- ($F' = 1, 2$) and five-level ($F' = 1, 2, 3$) systems for the two different photon shapes and a single-photon detuning of $\Delta{=}{-}200\,\mathrm{MHz}$ are shown in Figure 2.6. When the second excited state $F' = 2$ is incorporated, the intensity of the control beam changes significantly due to the constructive interference (blue and orange lines). A frequency chirp on the control pulse mostly compensates the addition of the third excited state $F' = 3$, since this level does not contribute to the population transfer but causes additional light shifts (orange and green dotted lines).

2.4.3.1. Absorption Efficiency

There is a direct mapping between the control pulse and the temporal mode which is produced and stored. It was shown above that neglecting excited states affects the mapping between the photonic mode and the control pulse. This argument is further expanded

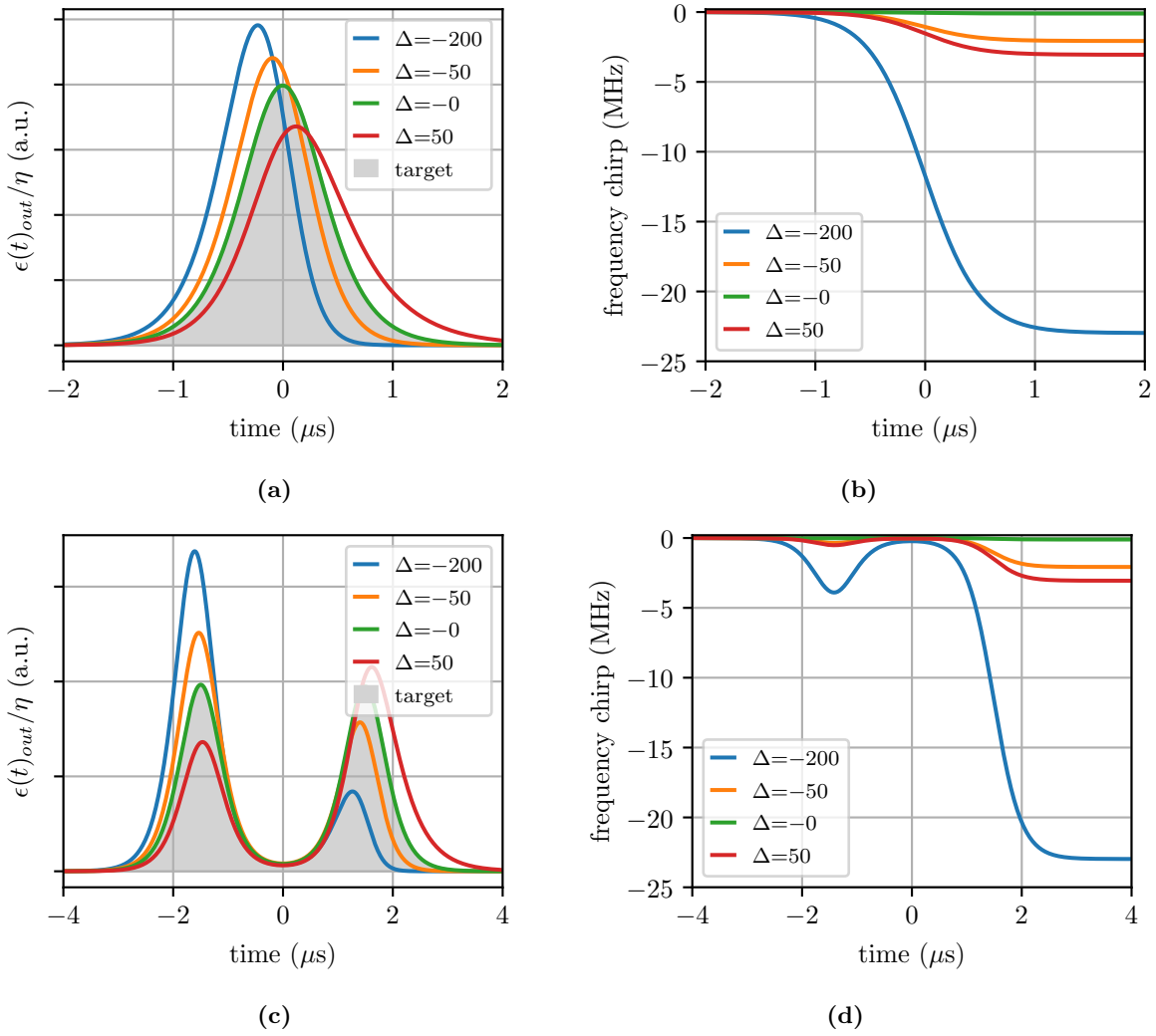

Figure 2.5.: Photon intensity amplitudes and phase chirps resulting from only considering one excited state. The profile of the Rabi control beam is generated using the model which incorporates only one excited state. When those profiles are applied to the system which incorporates all significant excited states, the resulting photon becomes deformed (Figures **(a)**,**(c)**), and the photon's center frequency is dynamically shifted (Figures **(b)**,**(d)**) depending on the single-photon detuning.

to investigate the storage efficiency achievable with the model by Gorshkov *et al.* [90]. Here, the notation from above is used for the photon absorption process. The reverse mappings,

$$\Omega_{c,\Delta}^{(F',\mathrm{write})}\left(\epsilon_{\mathrm{in}}(t)\right), \quad \epsilon_{\mathrm{in},\Delta}^{(F')}\left(\Omega_c^{\mathrm{write}}(t)\right) , \tag{2.80}$$

provide the control pulse to store the incoming mode $\epsilon_{\mathrm{in}}(t)$ or respectively provide the stored mode when the control pulse $\Omega_c^{\mathrm{write}}(t)$ is applied, for a system with the excited states F'. Assuming that a certain control $\Omega_c^{\mathrm{write}}(t)$ pulse only stores the corresponding mode, but does not store a mode orthogonal to $\epsilon_{\mathrm{in}}(t)$ (see Section 2.5.4 for an experimental test), and assuming again that the system with $F' = 1, 2, 3$ is close to the physical reality. The stored temporal mode for a control pulse calculated in the over-simplified system ($F' = 1$)

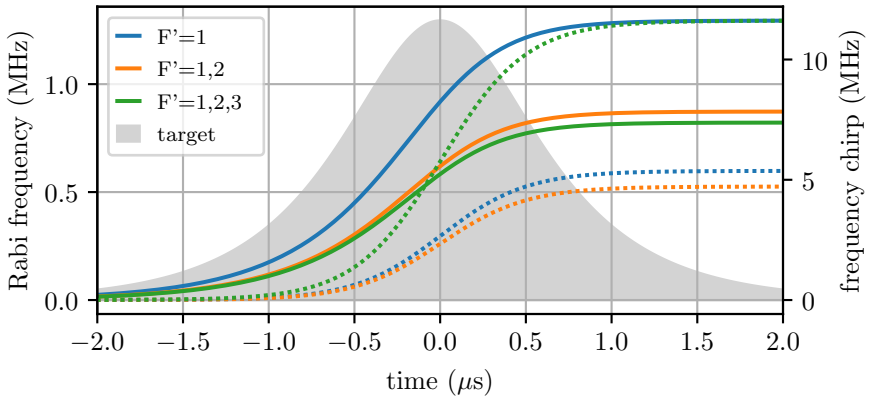

(a)

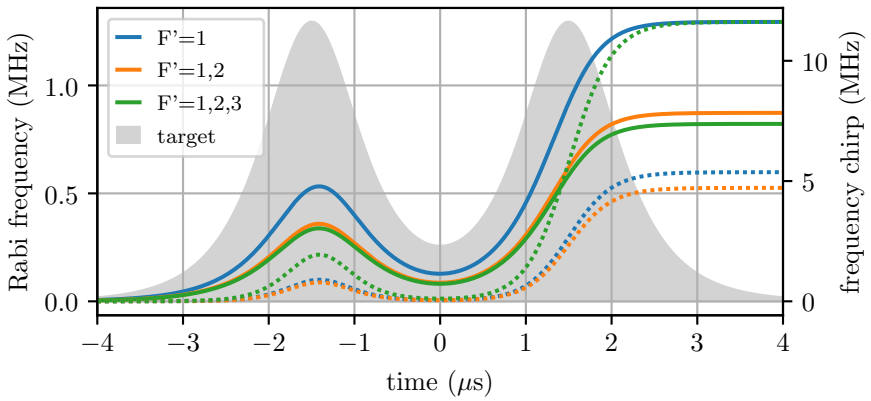

(b)

Figure 2.6.: Control pulses with frequency chirp compensation. Control pulses for the production of two different target photon shapes **a)** hyperbolical secant, **b)** double hyperbolical secant shown by the filled area. The solid lines show the Rabi driving amplitudes (left scale) and the dashed lines correspond to an additional phase profile in terms of a phase chirp (right scale). The color coding corresponds to the model either incorporating only a single excited state, two excites states or all three relevant excited state each for a single-photon detuning of $-200\,\mathrm{MHz}$.

can be evaluated using the reverse mappings,

$$\tilde{\epsilon}_{\mathrm{in}}(t) = \epsilon_{\mathrm{in},\Delta}^{(F'=1,2,3)}\left(\Omega_{c,\Delta}^{(\boldsymbol{F'=1},\mathrm{write})}\left(\epsilon_{\mathrm{in}}(t)\right)\right) \ . \tag{2.81}$$

The achievable absorption efficiency is given by the overlap of the two temporal modes.

$$\eta_w = |\langle\epsilon_{\mathrm{in}}|\tilde{\epsilon}_{\mathrm{in}}\rangle|^2 = \int |\epsilon_{\mathrm{in}}(t)\cdot\tilde{\epsilon}_{\mathrm{in}}(t)^*|^2\,dt \ . \tag{2.82}$$

As shown in Figure 2.7a the overlap between the target mode and the absorbed mode due to the wrong control pulse rapidly degrades with an increasing single-photon detuning. The resulting storage efficiency is shown in Figure 2.7b.

In this section, it was shown that for large single-photon detunings, neglecting the coupling to additional excited states significantly affects the photonic mode produced and stored. For the specific light-matter interface used here, even a modest single-photon detuning of several cavity line widths significantly degrades the storage efficiency due to a

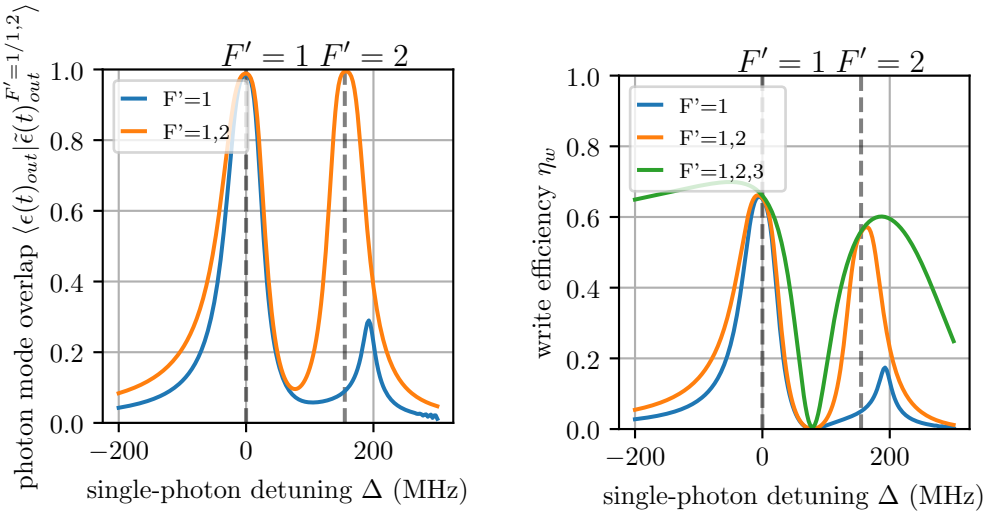

Figure 2.7.: Impact of additional excited states to the absorption efficiency as a function of the single-photon detuning: a) The theoretical overlap between the photonic mode stored by a control pulse generated by incorporating only a single $|F' = 1\rangle$ excited state and the target mode according to the system incorporating all coupled excited states. **b)** The resulting total storage efficiency as a function of the single-photon detuning.

mode-mismatch between the target mode and the absorbed mode. In the context of quantum networks, the control of the temporal modes of photons exchanged between network nodes is a requirement to maintain compatibility between physical systems.

2.4.4. Population Dynamics Atomic Decay

The time-dependent population of the individual atomic states and the cavity mode is an important property which must be evaluated to determine the impact of incoherent processes and to allow for a comparison of the model discussed here and the STIRAP model (see Section 2.2.2). In the latter, the excited states are not populated during the population transfer, and therefore the system is not subject to any atomic decay and allows for unity transfer efficiency. However, this is neither expected for the model by Gorshkov *et al.* nor the generalized multi-level extension described in this chapter. As it can be seen in the differential Equation 2.44 in Section 2.3, the entire population flow, from or into the storage state S, goes through the excited states P_i

$$\dot{S} = -i \sum_i \left(\Omega_{c,i}^*(t) P_i \right) . \tag{2.83}$$

Consequently, the excited states are temporally populated and the atomic decay rate γ competes with the light-matter interaction rate g to depopulate the excited states in the photon production process (see Equation 2.36).

By numerically integrating the differential equation system (2.35, 2.36, 2.37) with the control pulse $\Omega_c(t)$ extracted from the Equation 2.59, the time-dependent population of the individual states can be evaluated and the dynamics for the production of a 1 μs long photon with a single-photon detuning Δ=−150 MHz are shown in Figure 2.8. As expected, the population of the initial state $|s\rangle$ (purple line) is fully depleted throughout the photon

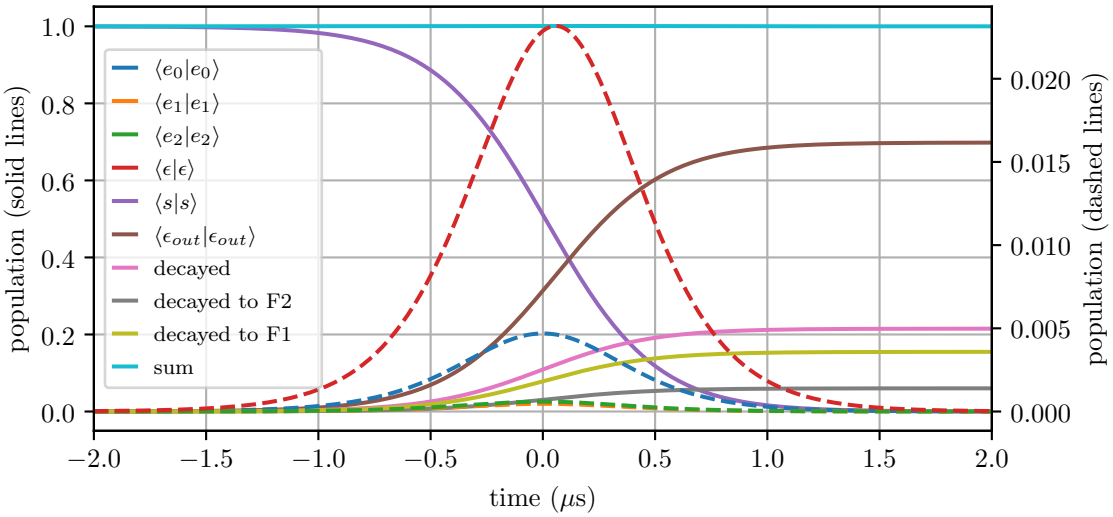

Figure 2.8.: Population dynamics during photon production. The dynamics of the system are extracted from the solution of the differential equation system from Section 2.3. The initially fully populated storage state (solid purple line) is entirely depleted and the population is transferred either to the out-coupled mode (solid brown line) or incoherently decays to either the $|5^2S_{1/2}, F{=}1\rangle$ or $|5^2S_{1/2}, F{=}2\rangle$ manifold (grey, yellow and pink solid lines). The intermediate population of the cavity mode and the excited states resemble the target shape of the produced photon (dashed lines).

production process. The population of the cavity mode resembles the shape of the photon which is produced during the process, rescaled with the out-coupling rate κ_c. Note that the population of the out-coupled mode must be rescaled with the escape efficiency η_{esc} to find the photon production efficiency (see Section 2.2.3). The probability for an atomic decay from the individual excited states P_i is given by the integral of the state's population scaled with the atomic decay rate γ,

$$P_{\text{decay}} = \sum_{i}^{\text{ex. states}} \int_{t_0}^{t_e} 2\gamma |P_i|^2 \, dt \ . \tag{2.84}$$

Both the hyperfine manifold to which the population decays to, as well as the manifold from which the decayed population originates from are a function of the single-photon detuning as depicted in Figure 2.9. By comparing the total decay probability (Figure 2.9, solid blue line) and the photon production efficiency (Figure 2.4, solid green line) it becomes apparent that the non-unity photon production efficiency is caused by a combination of the escape efficiency and the incoherent atomic decay. Besides degrading the efficiency of the coherent process, this decay can lead to the production of a deformed and incoherent photon which is a statistical mixture of various temporal modes due to the emission of a photon in a higher-order process. This will be discussed in Section 2.4.6.

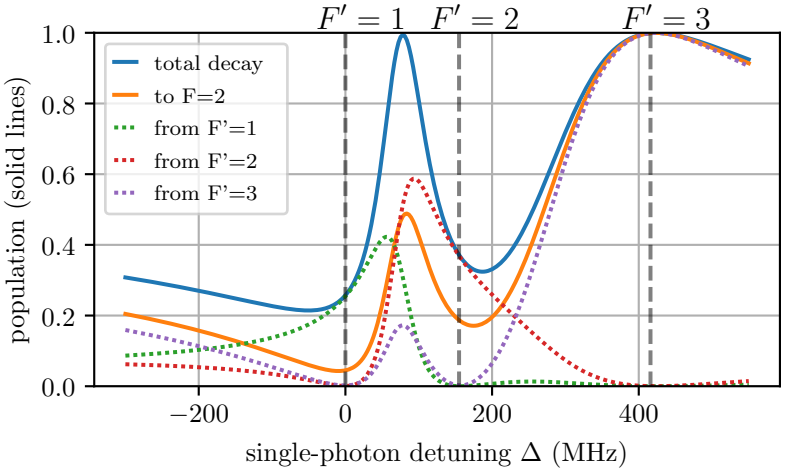

Figure 2.9.: Atomic decay probability. In the photon production process, the atomic population is transferred between two stable ground states via multiple excited states. The excited states are intermediately populated, and this population is subject to incoherent atomic decay. The total probability for an incoherent decay is shown as a function of the single-photon detuning (solid blue line). Atomic decay to the $|5^2S_{1/2}, F{=}2\rangle$ manifold (orange solid line) can further contribute to the production of a photon while atomic decay to the $|5^2S_{1/2}, F{=}1\rangle$ manifold just removes the excitation from the system. The contribution of the individual excited states as the source of the decay process (dashed lines) depends on the single-photon detuning. Note that the scattering probability exactly resembles the missing efficiency from the photon production process (see Figure 2.4).

2.4.5. Numerical Verification

To test the results of this chapter, the dynamics of the atom-cavity system are simulated using the master equation solver of the Python QuTiP Package[1]. The simulation implements the light-matter interaction Hamiltonian presented in Section 2.2.1 and therefore does not include the assumptions used to derive the analytical solution introduced in the previous section. Further, the simulation is aimed to incorporate incoherent processes associated with atomic decay as they will be discussed in the next chapter. To this end, not only the five-atomic states used in the model are included, but the full level-structure of the ^{87}Rb $|5^2S_{1/2}, F{=}2\rangle$ ground state, all coupled Zeeman states of the $|5^2P_{3/2}\rangle$ excited state, as well as both the σ^+- and the σ^-- cavity modes.

2.4.5.1. Numerical System

In the context of a collaboration with the research group of Prof. Giovanna Morigi a simulation package had been provided to calculate the dynamics of the photon storage process in the three-level atom-cavity system, as it has been used in [108]. This package was initially used to simulate the coherent photon absorption process, but had to be replaced as it could not be extended to incorporate incoherent processes and the full level-structure. However, the method for the reduction of the computation complexity by using a Fock basis and trail-conserving transfer matrices was directly inherited from the provided package. Note that in contrast to the package used by Giannelli *et al.* the system used here does not support the simulation of the photon storage process but only the production.

In this section, the basis to describe the system and the operators for the dynamic evolution are described. For the coupling between the cavity and the excited states, both polarization

[1] http://qutip.org/

modes of the cavity are decomposed into a set of coupled ground states,

$$|\sigma^+, m_F\rangle, \quad |\sigma^-, m_F\rangle \qquad \text{with} \quad m_F \in \{-1, 0, 1\} \ . \tag{2.85}$$

The coupling of these decomposed cavity modes to the free-space mode is modeled by the set of operators,

$$\hat{c}_{\kappa_c,\sigma^{+/-},m_F} = \frac{\kappa_c}{2}|\text{free-space}, \sigma^{+/-}, m_F\rangle\langle\sigma^{+/-}, m_F| \ , \tag{2.86}$$

which describe the collapse of the cavity modes to a set of free-space states,

$$|\text{free-space}, \sigma^{+/-}, m_F\rangle \ , \tag{2.87}$$

with the out-coupling rate κ_c of the cavity field. For the parasitic losses of the cavity field, a similar set of collapse operators is given by

$$\hat{c}_{\kappa_l,\sigma^{+/-},m_F} = \frac{\kappa_l}{2}|\text{losses}, \sigma^{+/-}, m_F\rangle\langle\sigma^{+/-}, m_F| \ , \tag{2.88}$$

with the corresponding set of states and the rate for parasitic cavity losses κ_l.

Atomic decay is modeled depending on the target state and the purpose of the simulation. To resemble the analytical system where incoherent decay results in a loss of the population, the collapse operator should transfer the population into dark atomic-decay states,

$$\hat{c}^{\text{decay state}}_{\gamma,F',m'_F,F=2,m_F} = \frac{\gamma_{F'm'_F,F=2,m_F}}{2}|F2-\text{decay}, m_F\rangle\left\langle F', m'_F\right| \ , \tag{2.89}$$

with the decay rate from a $|F', m'_F\rangle$ to $\left|5^2S_{1/2}, F{=}2, m_F\right\rangle$. However, in the more realistic scenario of repopulating the bright atomic states (see Section 2.4.6) the collapse operators should repopulate the ground state manifold,

$$\hat{c}^{\text{repopulate}}_{\gamma,F',m'_F,F=2,m_F} = \frac{\gamma_{F'm'_F,F=2,m_F}}{2}\,|F{=}2, m_F\rangle\left\langle F', m'_F\right| \ . \tag{2.90}$$

The decay to the dark $\left|5^2S_{1/2}, F{=}1\right\rangle$ manifold can be modelled as a transfer of the population to a decay state since the states in this manifold are not coupled by the control field and therefore can't further contribute to the photon production process,

$$\hat{c}_{\gamma,F',m'_F,F=1,m_f} = \frac{\gamma_{F'm'_F,F=1,m_F}}{2}|F1-\text{decay}, m_F\rangle\left\langle F', m'_F\right| \ . \tag{2.91}$$

Note, the choice of basis states and operators allows the $\left|5^2S_{1/2}, F{=}1\right\rangle$ ground states not to be included explicitly since their population is always the sum of the population of the atomic-decay states, the cavity modes, and the associated free-space modes. This drastically reduces the computation complexity since the sum of the population of all included states is 1, and the whole numerical system can be described in the Fock basis with trace-preserving transfer matrices [2]. This limits the validity of the simulation in the regime of having only a single excitation in the system but allows the computation of the dynamics within the full relevant level-structure of the ^{87}Rb atom in a reasonable time.

[2] Resounding thanks to Luigi Giannelli for providing this technique.

The unitary Hamiltonian $\hat{H}$ has the form:

$$\hat{H} = \sum_{\substack{F'=1,2,3 \\ m_F=-F'...F'}} \left|F', m'_F\right\rangle \left\langle F', m'_F\right| \tag{2.92}$$

$$+ \sum_{\substack{F'=1,2 \\ m_F=-1,0,1}} g_{|F=1,m_F\rangle\leftrightarrow|F',m_F-1\rangle} \left|F', m_F-1\right\rangle \left\langle \sigma^-, m_F\right| + h.c. \tag{2.93}$$

$$+ \sum_{\substack{F'=1,2 \\ m_F=-1,0,1}} g_{|F=1,m_F\rangle\leftrightarrow|F',m_F+1\rangle} \left|F', m_F+1\right\rangle \left\langle \sigma^+, m_F\right| + h.c. \tag{2.94}$$

$$+ \sum_{\substack{F'=1,2,3 \\ m_F=-F'...F'}} \Omega_c(t)\, c_{\left|F=2,m'_F\right\rangle\leftrightarrow\left|F',m'_F\right\rangle} \left|F', m'_F\right\rangle \left\langle F{=}2, m'_F\right| + h.c.. \tag{2.95}$$

The first term corresponds to the energy associated with the 13 coupled Zeeman substates of the $5^2P_{3/2}$ states. The second term describes all the 6 coupling terms for the σ^--cavity mode with the light-matter interaction strength of the specific transitions,

$$g_{|F=1,m_F\rangle\leftrightarrow|F',m_F-1\rangle}. \tag{2.96}$$

Analogously, the third term corresponds to the 6 couplings of the σ^+-cavity mode. And the last term includes the 13 driving terms of the π-polarized control field Ω_c with the Clebsch-Gordan coefficients of the individual transitions:

$$c_{\left|F=2,m'_F\right\rangle\leftrightarrow\left|F',m'_F\right\rangle}. \tag{2.97}$$

The complete system which is integrated by the QuTiP master equation solver[3] is given by the Lindblad master equation with the reduced density matrix $\hat{\rho}$ (see Section 2.2.1),

$$\frac{d}{dt}\hat{\rho} = \frac{1}{i\hbar}\left[\hat{H}, \hat{\rho}\right] - \sum_{\hat{c}} \hat{\mathcal{L}}(\hat{c}), \tag{2.98}$$

with the collapse operators $\hat{c}$ defined above and the initial state $|s\rangle = |F{=}2,\, m_F{=}1\rangle$. The control pulse Rabi frequency $\Omega_c(t)$ that is applied in the simulation is taken from the analytical model.

2.4.5.2. Numerical Results

To achieve agreement between the system represented by the simulation and the model which was analytically solved in this chapter, atomic decay is treated as a loss of the excitation from the system. This simplification is lifted in the next section when the impact of incoherent processes are investigated (see Section 2.4.6). For a single-photon detuning of -150 MHz, the numerical results (lines) for the population dynamics of the production of a 1 μs long photon are shown along with the analytical predictions (dots) in Figure 2.10. The remarkably good accordance between the simulation and the model demonstrates that the assumptions that have been applied in order to obtain an analytical solution are applicable even for multiple excited states. This is especially important since the bad-cavity limit ($\kappa \gg g, \gamma$) was assumed which is not fulfilled for the cavity parameters used here. For the three-level system, the feasibility of the application of the bad-cavity limit even for cavity systems in the intermediate coupling regime was already verified in [108]. Further, this

[3] http://qutip.org/docs/3.1.0/guide/dynamics/dynamics-master.html

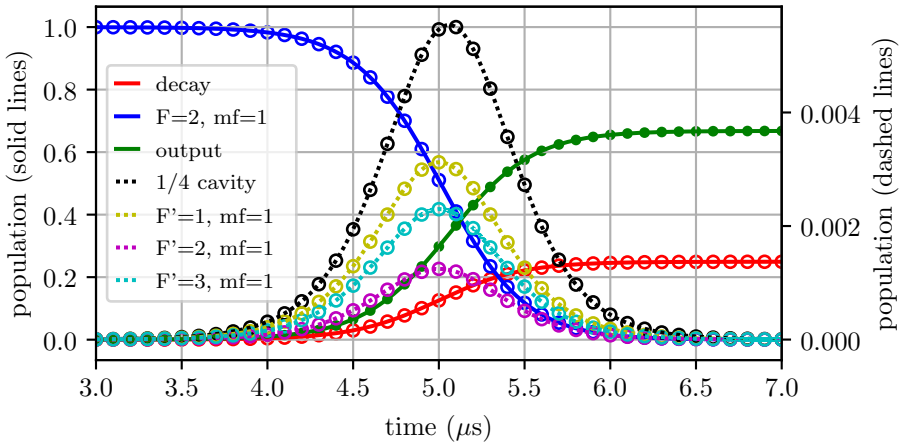

Figure 2.10.: Numerically evaluated population dynamics. By using the master equation solver of the QuTiP package, the dynamics of the system are numerically integrated without the assumptions which have been used to derive the analytical solution presented in the preceding section (lines). For comparison, the prediction of the analytical model is shown as the dots.

confirms that the simulation is likely to be implemented correctly. This is important since the same numerical system only with exchanged decay operators is used in the next section to simulate the impact of the incoherent decay, without the possibility for a analytical cross-check.

2.4.6. Incoherent Processes

In the formalism discussed in this chapter, all incoherent decay processes are treated as a loss of the excitation from the system, even though a photon can be produced even after such an incoherent decay process. Therefore, this simplification will result in an underestimation of the photon production efficiency in the theoretical prediction. Furthermore, due to the random nature of atomic decay, the resulting temporal mode becomes a statistical mixture of various temporal modes and consequently, the emitted photon will exhibit a deformed shape. Therefore, the investigation and quantification of both effects are crucial to allow for an experimental test of the model. This quantification is the subject of this section.

In the differential equation for the population amplitude of the excited states (see Equation 2.36)

$$P_i = \frac{1}{(\gamma + i\delta_i)} \left(i g_i \epsilon(t) + i\Omega_{c,i}(t) S \right) \ , \tag{2.99}$$

the atomic decay rate γ simply removes the population from the system. In reality, for the system used throughout this thesis, the atomic population decays to one of several different ground states either in the $|F{=}1\rangle$ or $|F{=}2\rangle$ manifold as depicted in Figure 2.11a. While all states in the $|F{=}1\rangle$ manifold are dark and do not further contribute to the photon production process, every state in the $|F{=}2\rangle$ manifold is coupled by the control pulse and form at least one Λ-system with one of the excited states and one of the two possible cavity modes. For the production of well-shaped and indistinguishable photons, this is problematic in multiple ways. Firstly, even if the population decays back to the initial state, the starting time of the second production process is random and therefore results in a deformed photon on success. For a decay to any other Zeeman state within the $|F{=}2\rangle$ manifold, the produced photon must have a deformed shape as the Clebsch-Gordan coefficients are

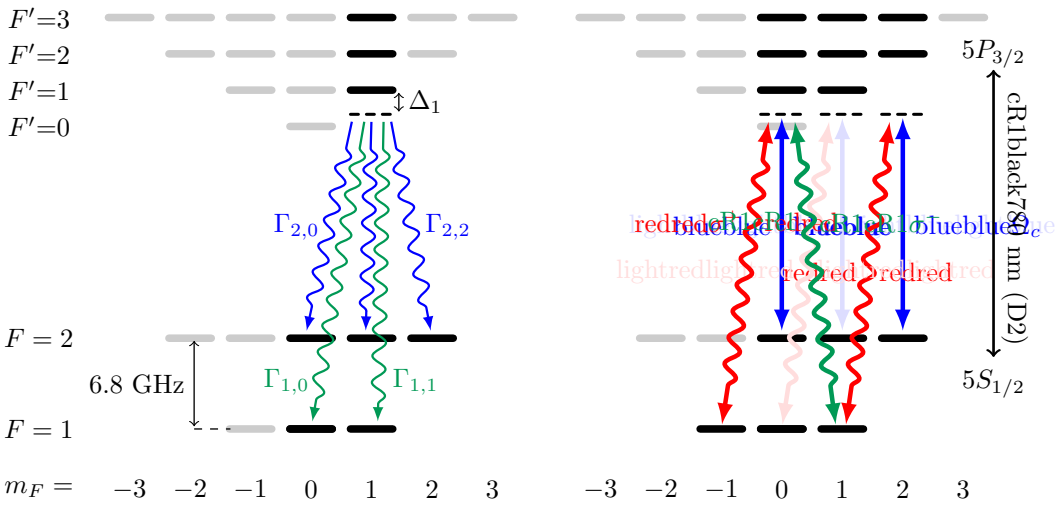

(a) Incoherent decay **(b)** Second photon production attempt

Figure 2.11.: Incoherent photon production processes. a) During the photon production process, the atomic population can incoherently decay to states either in F=1 (green arrows) or in F=2 (blue arrows). Decay to F=1 simply removes the excitation from the system while atomic decay to F=2 can lead to an incoherent production process shown in **b)**. The population can decay to one of three possible states. While only two of those contribute to the production of a σ^- photon, starting at a random time, the population which decayed to the state $|F{=}2, m_F{=}0\rangle$ can also contribute to the creation of a σ^+ photon. The ratio of the different subprocesses depends on the single-photon detuning Δ. With a second incoherent decay, the $|F{=}2, m_F{=}{-}1\rangle$ state may become involved resulting in a higher ratio of σ^+ photons produced.

different for all other possible Λ-systems. For a population decay to $|F{=}2, m_F{=}0\rangle$, the σ^+-mode of the cavity opens the possibility to generate a photon with an orthogonal polarization, as depicted in Figure 2.11b by the green curly line. The redistribution of the population in the $|F{=}2\rangle$ manifold by incoherent decay events can happen multiple times, opening even more possible Λ-systems which can contribute to the production of a photon.

For a meaningful comparison between the theoretical predictions and experimental results, both the ratio of incoherently produced photons and the associated photonic shape must be evaluated. To this end, the simulated system must incorporate the full ground state level structure of ^{87}Rb, 13 excited states of the D_2 transition (only the $m_F = \pm 3$ states and $|F{=}1, m_F{=}0\rangle$ are not coupled) and both cavity modes to support σ^-- and σ^+-transitions. In contrast to the simulation from the previous Section 2.4.4, atomic decay must not be treated as a loss of the single excitation from the system, but it must repopulate the ground states according to the branching ratios given by the Clebsch-Gordan coefficients. To this end, the collapse operators for the atomic decay to the $|F{=}2\rangle$ manifold are exchanged to repopulate the states rather than removing the excitation from the system (see Section 2.4.5.1).

By the application of the otherwise same simulation method as before, the dynamics of the production process for a single-photon detuning $\Delta = 300\,\text{MHz}$ for a $1\,\mu\text{s}$ long photon is shown in Figure 2.12. The time-dependent population of the relevant atomic states is shown in the first four rows as the solid blue lines. The last row shows the population of the σ^+ (red) and σ^- (dark blue) cavity modes decomposed to the three ground states in the $|F{=}1\rangle$ manifold where the population was transferred to, due to the coupling between the ground states and the excited states by the cavity. Note that only the $m_F = 1$ states and

the σ^+ cavity mode coupled to the $|F{=}1, m_F{=}0\rangle$ ground state are part of the analytical model. For those states, the orange line indicates the difference between the simulated dynamics and the theoretical prediction. The green line shows the population of the initial state scaled by a factor of 1/5 to fit the same scale. As described above, the atomic decay distributes population among the states in the ground state manifold, resulting in the formation of additional Λ-systems and an intermediate population of almost all excited states of the $5^2P_{3/2}$ state. As seen in the last row, this results in the overly efficient production of a photon with a deformed envelope, which is also partly emitted into the wrong polarization mode of the cavity.

The single-photon detuning depending photon production efficiency (see Section 2.4.2) only incorporates the fully coherent production processes. For a quantum network application, a coherent interface is desired as it allows for indistinguishability between subsequently created photons and for coherence between the orthogonal photonic polarization modes [58]. However, the seemingly increased efficiency due to atomic decay processes is not beneficial, but rather diminishes the indistinguishability due to the randomness of the decay process, and affects the coherence between the photonic polarization modes. Therefore, it is not sufficient to experimentally optimize the photon production efficiency as a function of the single-photon detuning to choose the working point, because this method is unable to distinguish between coherent and incoherent emissions.

For the specific system used here, only an atomic decay to the $|F{=}2\rangle$ manifold can result in the production of a photon after an incoherent process. Therefore, with regard to the coherence of the production process, it is best to maximize the ratio between coherent production efficiency and the decay probability to $|F{=}2\rangle$. As it can be seen in Figure 2.9 the decay probability to $|F{=}2\rangle$ is minimized when the resonator is on resonance with the $|F{=}1\rangle \leftrightarrow |F'{=}1\rangle$ transition. For this single-photon detuning, the population transfer via the $|F'{=}1, m_F{=}1\rangle$ excited state is maximized. From all coupled excited states this specific state exhibits the most beneficial branching ratios between the $|F{=}1\rangle$ and the $|F{=}2\rangle$ ground state manifolds. However, for more advanced applications with multiple atoms coupling to the same cavity mode, a non-vanishing single-photon detuning is a requirement to allow for individual control over the light-matter coupling. In such a scenario, the suppression of the cross-talk between the individual emitters is traded against the coherence of the interface, and the choice of the working point must be carefully evaluated. See Figure 2.13 in Section 2.5.1 for the photon production efficiency including incoherent processes over the single-photon detuning along with experimental data. In Figure 2.15 in Section 2.5.2 simulation results for the photon shapes for different single-photon detuning along with experimental results are shown.

So far the cavity based light-matter interface was investigated analytically and numerically. For the rest of this chapter, the model is tested with experimental results, and some applications of this light-matter interface are experimentally demonstrated.

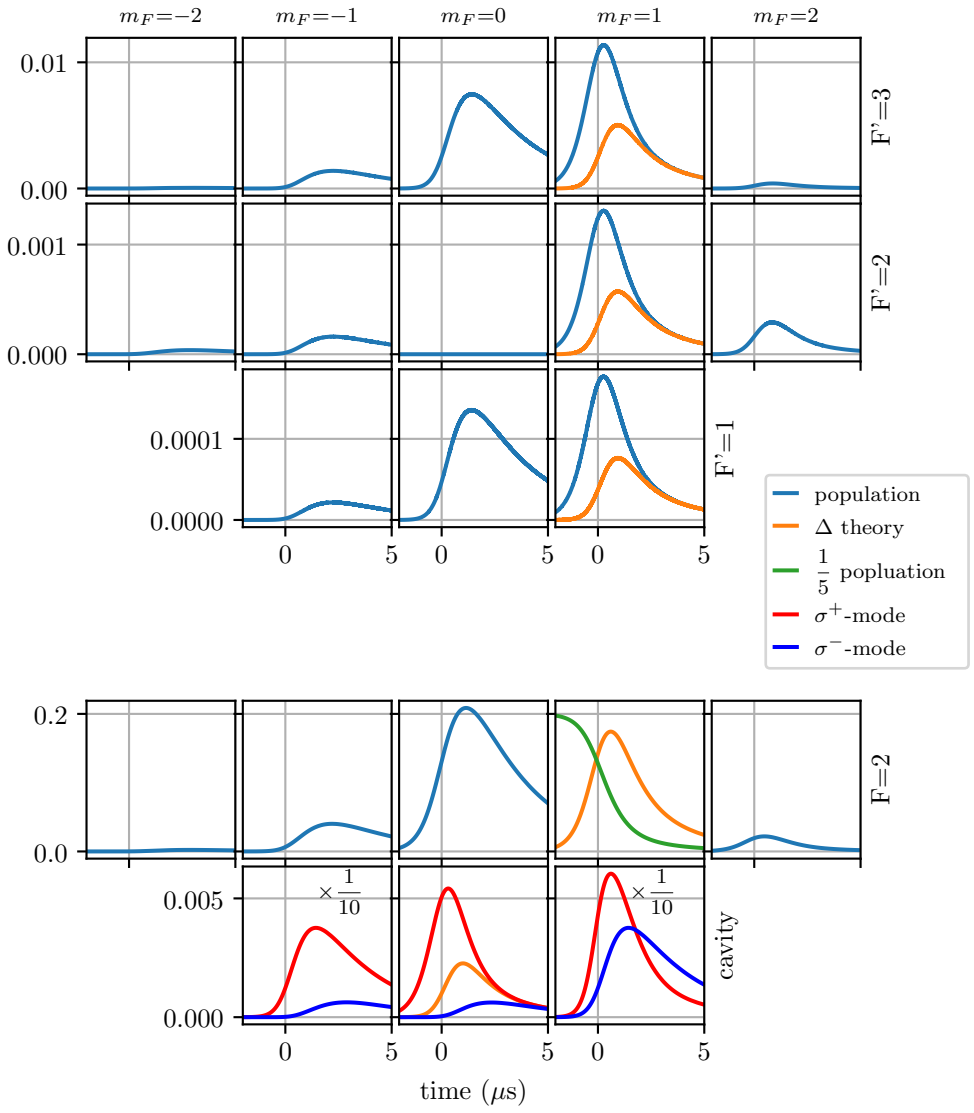

Figure 2.12.: Population dynamics including incoherent decay. The structure of the plot resembles the D_2 line and the $|F{=}2\rangle$ manifold of the ^{87}Rb atom. In the first row, the population dynamics of the individual Zeeman states of the $|5^2P_{3/2}, F'{=}3\rangle$ manifold is shown (blue lines) along with the deviation from the analytical model, which treats incoherent decays as complete removal of the excitation from the system. The second and third rows correspond to the $|5^2P_{3/2}, F'{=}2\rangle$ and $|5^2P_{3/2}, F'{=}1\rangle$ manifolds of the D_2 line. The fourth row corresponds to the $|F{=}2\rangle$ manifold and the last row does not show the $|F{=}1\rangle$ manifold but the population of the cavity which is linked to transfers in the different Zeeman substates of the $|F{=}1\rangle$ manifold. The population of the cavity directly resembles the shape of the produced photon. The initial population in $|F{=}2, m_F{=}1\rangle$ (green line) is scaled by a factor 1/5 and the population of the cavity mode which corresponds to a transfer into the $m_F = \pm 1$ states is scaled by a factor 10. The chosen single-photon detuning is +300 MHz. Here, due to the incoherent decay, the population of other states outside of the states included in the model can be observed as well as an overly efficient production of a deformed photon.

2.5. Experimental Test of the Multi-Level Model

In the previous sections, an analytical solution for the single-photon absorption and emission process was derived and numerical methods were applied to quantify the impact of incoherent processes. Here, multiple aspects of the model are tested experimentally and compared to the analytical and numerical results. Firstly, the predicted photon production

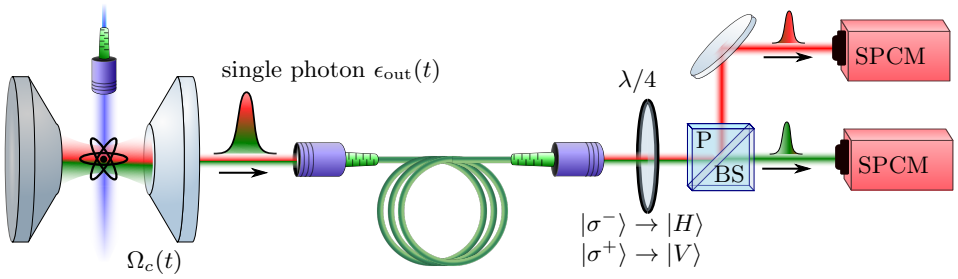

Figure 2.13.: Polarization-resolving single photon detection. By the application of the control Rabi frequency $\Omega_c(t)$, a single photon with the temporal shape $\epsilon_{\mathrm{out}}(t)$ is emitted into the cavity mode, and predominantly leaves the cavity through the out-coupler mirror. The free-space mode is subsequently coupled to a 10 meter long birefringence-compensated optical fiber which guides the photon to the detection setup. In the detection setup, the polarization of the photon is rotated by a $\lambda/4$ waveplate which maps the left and right circular polarization components onto horizontal and vertical linear polarizations, respectively. A polarizing beamsplitter subsequently splits the two linear polarization components into two different optical paths and a set of time-resolved single-photon counting modules is used to record the arrival time for each polarization component.

efficiency is probed as a function of the single-photon detuning. The amplitude profiles of the produced single photons are then determined and compared to numerical predictions. Finally, the phase profiles of the single-photon envelopes are measured with a homodyne setup to demonstrate the accuracy of the derived model. Following the experimental test of the formalism, the mapping between the control pulse and the photonic mode is utilized to demonstrate mode selective storage and the ability to convert the shape of a single photon for quantum network applications.

2.5.1. Photon Production Efficiency

To probe the photon production efficiency, a single atom is loaded and trapped at the center of the cavity. The atom is first initialized in the $|F{=}1,\ m_F{=}0\rangle$ ground state employing optical Zeeman pumping. Subsequently, the atomic population is transferred to the $|F{=}2,\ m_F{=}1\rangle$ state by a microwave-driven magnetic-dipole transition,

$$|F{=}1,\ m_F{=}0\rangle \leftrightarrow |F{=}2,\ m_F{=}1\rangle \ . \tag{2.100}$$

The microwave field does not exhibit a clean polarization to exclusively drive the targeted transition. To suppress driving the atomic population to the $|F{=}2,\ m_F{=}{-}1\rangle$ and $|F{=}2,\ m_F{=}0\rangle$ ground states, a magnetic guiding field is applied which shifts these undesired transitions out of resonance. The overall initialization fidelity is determined to be $0.90{\pm}0.02$. After the initialization process, the single-photon detuning specific control Rabi frequency $\Omega_c(t)$ to produce a 2 μs long hyperbolic secant shaped photon is applied, and the out-coupled single-photon is split into its circular polarization components, that are subsequently detected by a pair of time-resolving single-photon counting modules. After a few hundred repetitions, the photon production efficiency is determined by first compensating for the non-unity detection and coupling efficiency η_D (see Section A.6) and then dividing the number of detected photons *clicks* by the total number of trials,

$$\eta(\Delta) = \frac{\mathrm{clicks}(\Delta)}{\eta_D \times \mathrm{trials}(\Delta)} \ . \tag{2.101}$$

The experimental procedure is repeated for various single-photon detunings Δ.

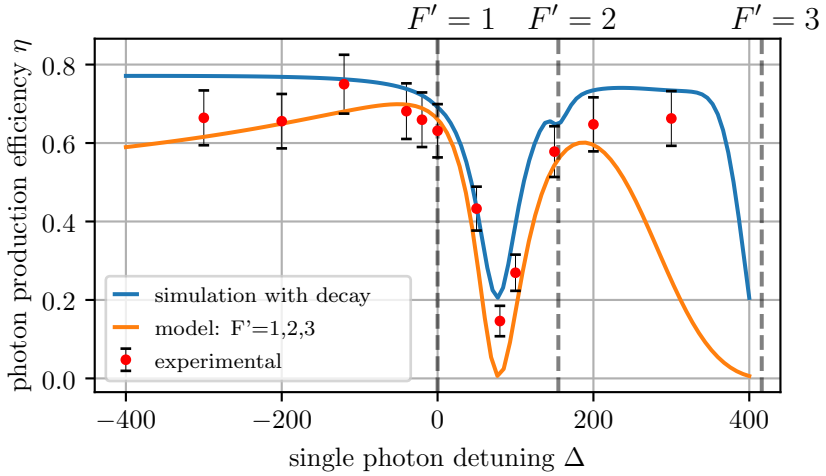

Figure 2.14.: Experimentally determined photon production efficiency. The atom is initialized in the $|F{=}2, m_F{=}1\rangle$ ground state. Subsequently, the control Rabi frequency $\Omega_c(t)$, which is tailored for a specific single-photon detuning Δ is applied, and a photon may be emitted into the cavity mode. After the photon leaves the resonator through the out-coupler mirror, it is detected by a set of single-photon counting modules. The measured detection efficiency is compensated for the non-unity detection efficiency of the counting modules and shown as a function of the single-photon detuning (red dots) along with the statistical uncertainty. Additionally, the prediction of the analytical model (orange line) is shown which only includes fully coherent photon production processes.

The resulting photon production efficiency is shown in Figure 2.14 as a function of the single-photon detuning (red dots) along with the efficiency for the coherent process as it is predicted by the analytical model (orange line) and the results from the numerical simulation (blue line) which incorporates incoherent processes. It is expected that the observed photon production efficiency is above the predictions by the analytical model since the model only includes the fully coherent process. The model used in the simulation does not incorporate the finite bandwidth of the resonator system. As it can be seen from Figure 2.5, for larger single-photon detunings the shift of the center frequency of the photon can exceed the bandwidth of the cavity when the light-shifts are not compensated correctly. Although the control pulse $\Omega_c(t)$ is tailored to not result in frequency shifted photons, an incoherent decay process to another level within the $|5^2S_{1/2}, F{=}2\rangle$ manifold will result in a new set of Λ-systems with different Clebsch-Gordan coefficients (see Section 2.4.6). In this scenario, the compensation of the frequency chirp breaks down, and for large enough shifts, the photon is not resonant with the resonator anymore and cannot be efficiently produced into the cavity mode. Since the simulation does not include this decremental effect, it is expected that especially for larger single-photon detunings, the experimentally measured efficiency is lower than predicted by the simulations. This is in good agreement with the determined data (see Figure 2.14).

The most pronounced effect due to the coupling to multiple excited states is the destructive interference for a single-photon detuning in between the $|5^2P_{3/2}, F'{=}1\rangle$ and $|5^2P_{3/2}, F'{=}2\rangle$ states, as it is clearly observable in the experimental data. Again, the destructive interference is not perfect due to the possibility of atomic population decay to another state within the $|5^2S_{1/2}, F{=}2\rangle$ manifold with different Clebsch-Gordan coefficients such that the interference condition is no longer fulfilled.

2.5.2. Intensity Profiles and Polarizations

The model derived in Section 2.3 provides a bijective mapping between the produced photonic shape $\epsilon_{\text{out}}(t)$ and the control Rabi frequency $\Omega_c(t)$. As it has been discussed in Section 2.4.6, incoherent decay of the atomic population will result in a deviation from the target shape as it can be inferred from simulations. Here, the experimentally produced photon is decomposed into its circular polarization components and the intensity profiles of the two components are compared to the simulation results.

The experimental procedure is similar to the determination of the photon production efficiency. Firstly, the atom is prepared in the $|F{=}2,\, m_F{=}1\rangle$ state. By the application of the control pulse $\Omega_c(t)$, a photon may be emitted into the cavity mode and out-coupled to the free-space mode, that is subsequently coupled into an optical fiber guiding the photon to the polarization-resolved single-photon detection setup.

Here, the photon *click* is also detected time-resolved and the intensity of the photonic profile is reconstructed from the histogram of binned arrival times for both circular polarization components. This is shown for three different single-photon detunings in Figure 2.15, where the solid line indicates the histogram of binned arrival times for the σ^+ mode (red) and the σ^- mode (green). The red and green filled areas show the results from the simulation and the grey area indicates the normalized target shape. For all single-photon detunings, the experimentally extracted intensities are in good qualitative agreement with the numerical predictions and the shapes of both polarization components match well. The measured amount of photons in the σ^- mode is slightly above the expectation which may be explained by the considerable error bar in the calibration of the detection efficiencies (see Section A.6).

As expected from the simulations, a single-photon detuning $\Delta{=}{+}300$MHz results in the most significant deviation between the target shape and the measured shape since the incoherent processes are most pronounced for this detuning (see Section 2.4.6). In contrast, for $\Delta{=}{-}20\,$MHz the incoherent decay to the $\left|5^2S_{1/2}, F{=}2\right\rangle$ manifold is minimal (see Figure 2.9) resulting in the best overlap with the target shape. For the large red detuning (-300 MHz) the amount of scattering to the $\left|5^2S_{1/2}, F{=}2\right\rangle$ manifold and the associated incoherent processes rise again compared to $\Delta{=}{-}20\,$MHz. The overall good agreement between simulations and experimental results suggest that the decremental processes are well understood. Moreover, the intermediate population of the excited states and the inevitable population decay limits the coherence and efficiency of the light-matter interface. Note that this is in contrary to the predictions of the STIRAP (see Section 2.2.2) model.

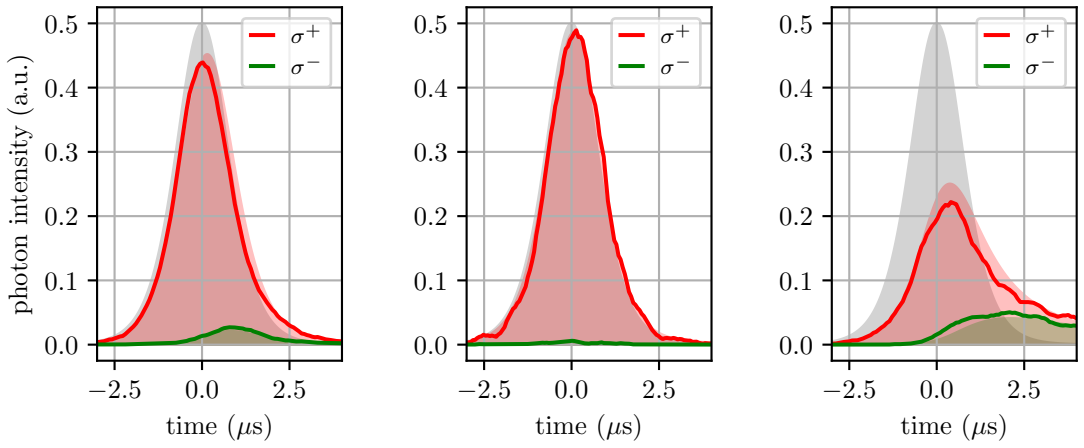

(a) Δ=−300 MHz **(b)** Δ=−20 MHz **(c)** Δ=+300 MHz

Figure 2.15.: Intensity profile of produced single photons. After the atom is initialized in the $|F{=}2, m_F{=}1\rangle$ ground state, the control pulse $\Omega_c(t)$ to produce a 2 μs long hyperbolic secant shaped photon is applied for three different single-photon detunings Δ. The resulting photon is decomposed into its two circular polarization components which are subsequently detected by a pair of time-resolved single-photon counting modules. The solid red line shows the histogram of arrival times for the σ^+-polarized component and the solid green line for the σ^- component. The red and green filled area indicate the expectation from numerical simulations in which photon production processes after incoherent decay events are considered (see Section 2.4.6).

2.5.3. Produced Complex Photonic Mode

2.5.3.1. Experimental Results

To reconstruct the temporal shape of the produced photon $\epsilon_{\text{out}}(t)$ the homodyne technique presented in Section 2.2.4 is applied. To minimize the impact of incoherent photon contributions (see Section 2.4.6), the single-photon detuning is chosen to be Δ=-20 MHz. After the atom is initialized in the $|F{=}2, m_F{=}1\rangle$ state, a photon is produced into the cavity by applying one of two specially-tailored control fields on an axis perpendicular to the cavity axis. The produced photon is coupled-out through the out-coupler mirror and guided to the detection setup through an optical fiber. Subsequently the photon is combined with a strong local-oscillator reference on a non-polarizing 50 : 50 beamsplitter. The mode of both output-ports of the beamsplitter is directed onto a set of fast photo diodes. Note that due to the π-phase shift caused by the reflection within the beamsplitter, the interference between the produced photon and the local-oscillator field has an opposite direction for each output mode. This fact is used to suppress technical intensity fluctuations of the local-oscillator field by recording the difference signal of both photo diodes [119].

After the acquisition of around two thousand intensity curves, the autocorrelation-function and the eigenfunctions and eigenvalues of the resulting kernel are calculated. The experiment is performed twice with two different control fields. Firstly, the frequency chirp of the produced photon should be suppressed by using the derived formalism (see Section 2.3) to generate a control Rabi frequency $\Omega_c^{\text{comp.}}$ which should yield a real-valued photonic mode by correctly compensating the effect of light-shifts linked to the coupling of the control beam to the excited levels. Secondly, the compensation of those light-shifts is deliberately neglected. The latter should result in a significant frequency chirp of the photon. Note that such a frequency chirp corresponds to an evolving phase angle of the temporal mode (see Section 2.4.3) and implies the existence of an imaginary-valued part of the photonic

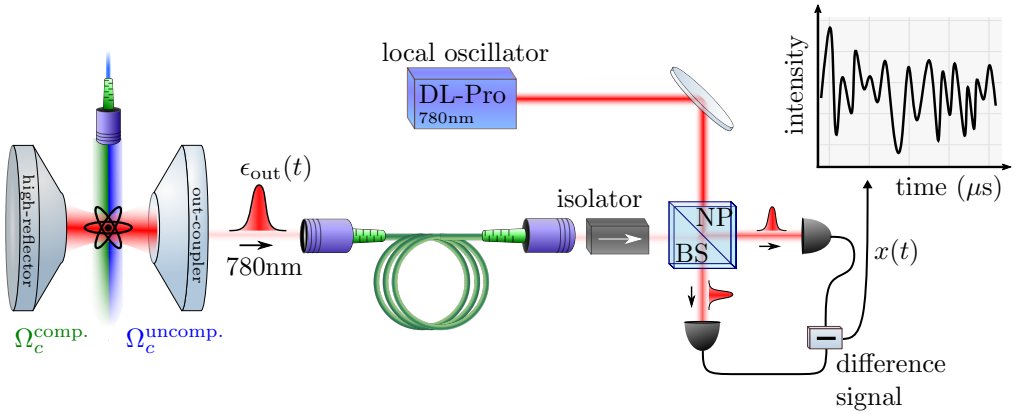

Figure 2.16.: Homodyne setup for complex shape reconstruction. The mode of the produced photon is combined with a strong local-oscillator field by means of a non-polarizing beamsplitter and the resulting intensities behind the two output-ports are measured by a set of balanced photo diodes. Due to the phase shift caused by the reflection within the beamsplitter, the direction of interference between the two fields has an opposite sign on both output ports. By using the difference of the signal of both photo diodes the effect of technical noise within the local oscillator field can be canceled out, and therefore the visibility of the interference can be maximized. The data acquisition of the resulting intensity curve $x(t)$ is synchronized with the photon production protocol and measured with a fast oscilloscope. An optical isolator behind the cavity blocks reflected light from the local oscillator from reflecting on the cavity and from entering the cavity to interact with the atom.

envelope. As it has been previously discussed (see Section 2.2.4), a single complex-valued temporal mode mixed with vacuum results in two eigenvalues of the kernel greater than 1. The corresponding eigenfunctions represent the real and imaginary part of the temporal mode, scaled by the magnitude of the eigenvalues minus 1. Consequently, a temporal mode with no frequency chirp is a purely real-valued mode and should not exhibit an imaginary part and therefore should result in a kernel with only one eigenvalue (significantly) larger than one.

As it can be seen from the measurement data (Figure 2.17, right side) the produced photon with no light-shift compensation exhibits a kernel with two eigenvalues significantly above one. From the eigenfunctions, the real and imaginary part of the temporal mode can be reconstructed and compared to the theoretical predictions from the mapping between the applied control Rabi frequency and the produced shape. For the control pulse $\Omega_c^{\text{comp.}}$ the produced photonic mode results in only one eigenvalue of the kernel which is significantly larger than 1. This shows, that the photon does not exhibit a significant frequency chirp and therefore, that the compensation of light-shifts was successful. The overlap of the experimentally measured photonic mode with the expected mode according to the analytical model is $(90\pm1)\,\%$. However, if a constant detuning from the two-photon resonance of 150 kHz is assumed the overlap between the produced mode and the prediction is $(98\pm1)\,\%$ (red lines in Figure 2.17). Imperfections are expected due to the residual incoherent part and the imperfect initialization of the atom. Overall, this demonstrates the precision and applicability of the derived mapping between the photonic mode $\epsilon_{\text{out}}(t)$ and the control Rabi frequency $\Omega_c(t)$.

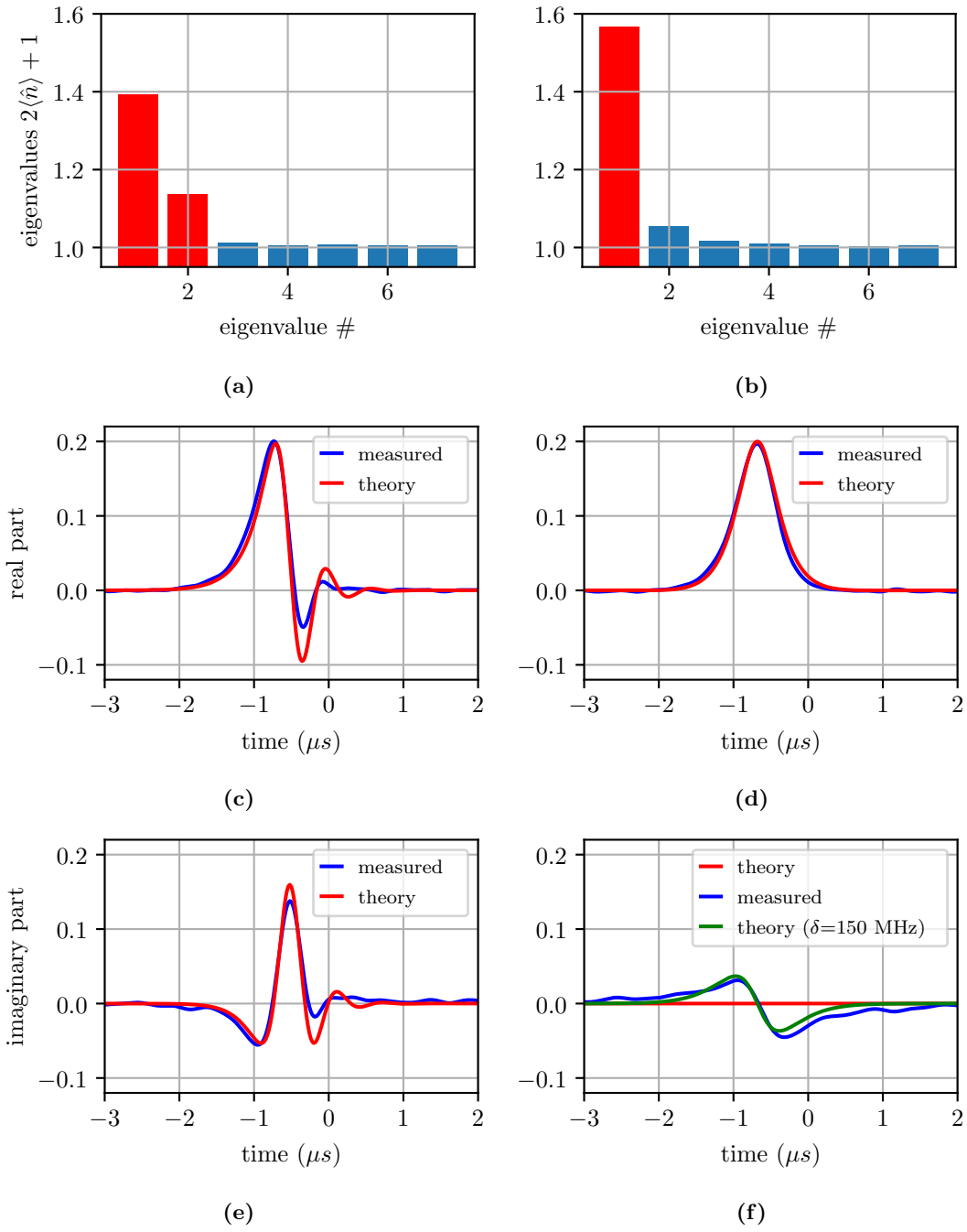

Figure 2.17.: Reconstructed photonic modes. The temporal modes of a produced single photon either with a compensated frequency chirp (**b**,**d**,**f**) or without compensation (**a**,**c**,**e**) are measured with a homodyne setup. The first row shows the magnitude of eigenvalues of the autocorrelation-kernel acquired with the homodyne measurement. The values above 1 correspond to the proportion of orthogonal modes present in the produced photon. A single eigenvalue witnesses a photon in a single real-valued temporal mode and therefore a non-existing frequency chirp. The second and third row show the reconstructed real and imaginary part of the photons (blue lines) along with the theoretical expectation (red line). The green line indicate the theoretical predictions for a constant two-photon detuning of 150 kHz.

2.5.4. Mode-Selective Photon Storage

The formalism derived, simulated and tested in this chapter provides a reversible mapping between the applied control pulse $\Omega_c(t)$ and the temporal photonic mode $\epsilon_{\text{in/out}}(t)$ to be

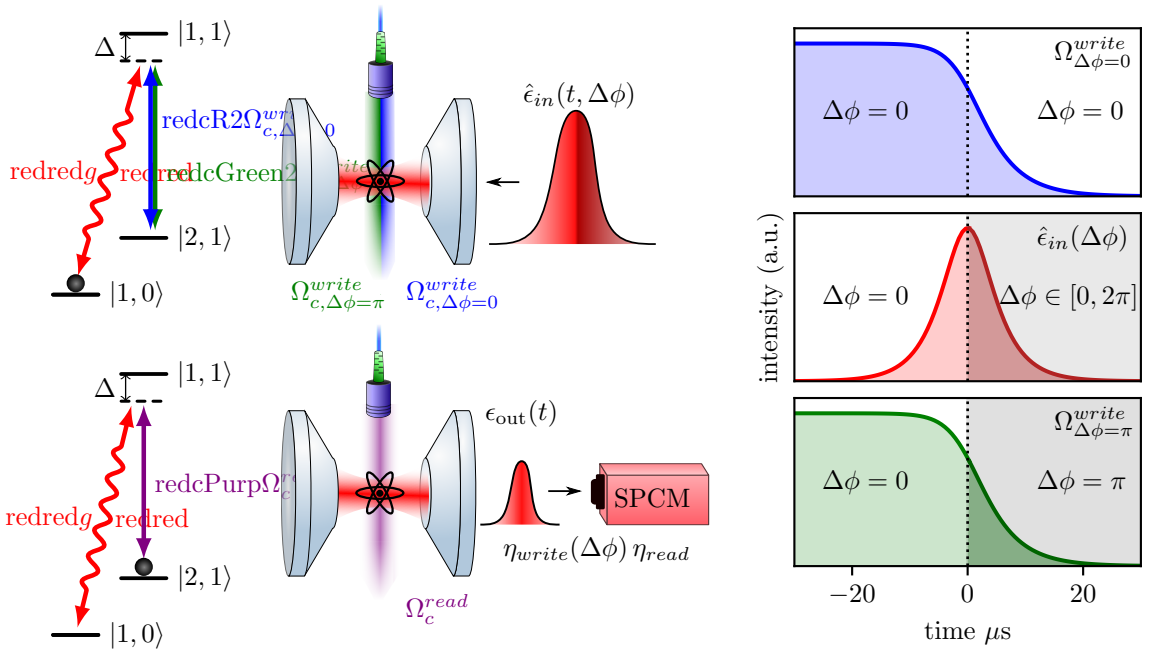

Figure 2.18.: Temporal mode selective storage. Schematic of the experiment to probe the temporal mode selective storage by measuring the storage efficiency for a photon with a variable phase jump in the center of its temporal mode. A single photon with a phase jump of $\Delta\phi$ is directed on the cavity (red curve) and one of two control fields is applied: Either a control field $\Omega^{\text{write}}_{c,\Delta\phi=0}$ (blue) which stores the temporal mode with a phase jump $\Delta\phi = 0$, or a control field $\Omega^{\text{write}}_{c,\Delta\phi=\pi}$ with a phase jump of π is applied. Subsequently, the photon is retrieved by the application of some suitable control pulse Ω^{read}_c. A single-photon counting module (SPCM) is used to evaluate the efficiency of the total process. The intensity profiles of the incoming photon (red) and the two control fields (blue, green) are shown on the right side. The storage efficiency for the two control pulses with (green) and without (blue) the phase jump of π is shown as a function of the applied phase jump $\Delta\phi$ in the center of the temporal mode of the photon.

stored or retrieved from an atom-cavity system. In the previous section, it was demonstrated that the produced photonic mode $\epsilon_{\text{out}}(t)$ can be selected by the choice of the control pulse $\Omega^{\text{read}}_c(t)$. Here, it is shown that in the case of photon storage, the absorbed temporal mode can also be controlled by the choice of the control pulse $\Omega^{\text{write}}_c(t)$. This is significant in multiple regards: It demonstrates that the knowledge of the actual temporal mode function including its phase term and the application of a suitable control pulse is important to achieve efficient light-matter interactions. Also, in a quantum network information can be multiplexed onto a set of orthogonal temporal modes given the ability to specify the temporal mode to interact with at a network node. Further, the ability to measure the overlap between the unknown temporal mode of an incoming single photon and a temporal mode specified by the control pulse applied yields a toolkit to analyze the complex shape of the incoming photon.

All previous experiments discussed in this chapter so far were based on the production of a single photon. In this experiment, an incoming photon is first stored and subsequently retrieved from the atom-cavity system. As motivated by the previous experiment, a single-photon detuning of $\Delta{=}{-}20\,\text{MHz}$ is chosen to maximize the efficiency while minimizing incoherent processes. By means of optical Zeeman pumping, the atom is initialized in the $|F{=}1, m_F{=}0\rangle$ ground state. Using a σ^+-polarized weak coherent pulse shaped by an acousto-optical modulator (AOM) an input pulse with $\bar{n}{=}1$ photons on average is generated and directed into the cavity system. The input mode $\epsilon_{\text{in},\phi}(t)$ has a characteristic time of

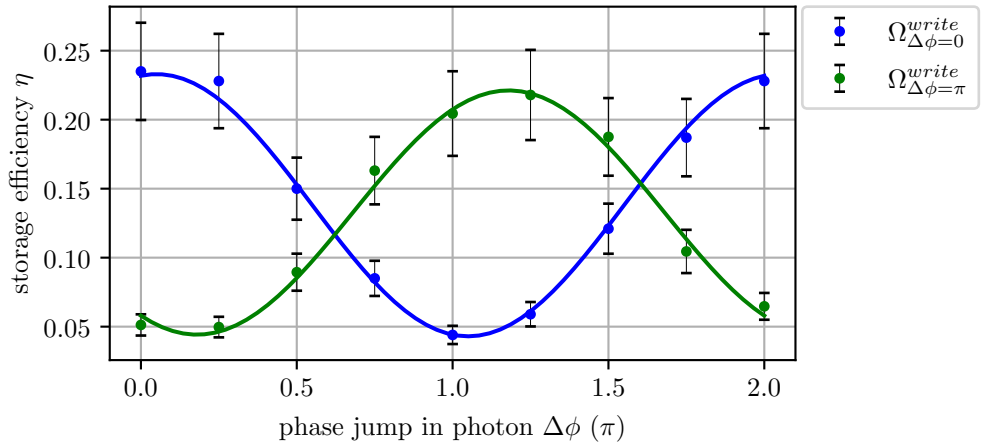

Figure 2.19.: Results for temporal mode selective storage. The efficiency for storing an incoming temporal mode with a phase shift of $\Delta\phi$ in the center of the temporal mode by applying one of two control fields is shown. The first control field $\Omega^{\text{write}}_{c,\Delta\phi=0}(t)$ is tailored to store the incoming mode with no phase shift ($\Delta\phi = 0$). The corresponding storage efficiency η is shown in blue as a function of the applied phase shift $\Delta\phi$. Alternatively, a control field to store the temporal mode with a phase shift $\Delta\phi = \pi$ in the center is applied, and the resulting efficiency is shown in green.

$T_C = 20\,\mu$s and a hyperbolic secant shaped amplitude with an additional phase term which exhibits an instantaneous shift of $\Delta\phi$ at the center of the temporal mode (see Figure 2.18, red curve). Over the course of many experimental repetitions, the phase shift $\Delta\phi$ is scanned from 0 to 2π. Note that the temporal mode with a phase shift $\Delta\phi = 0$ is orthogonal to the mode with a phase shift $\Delta\phi{=}\pi$. By leveraging the time-reversal argument (see Section 2.3.5) a control pulse $\Omega^{\text{write}}_{c,\Delta\phi=0}(t)$ to store the incoming mode without a phase shift and a second control pulse for the incoming mode with a phase shift $\Delta\phi{=}\pi$ are generated. Both control fields are applied in the storage process in independent experimental runs for all chosen actual phase shifts within the incoming photonic mode $\epsilon_{\text{in},\phi}(t)$ (see Figure 2.18, blue and green curves). Afterward, the efficiency of the storage attempt for a given phase shift $\Delta\phi$ with one of the two possible control fields $\Omega^{\text{write}}_{c,\Delta\phi=0}(t)$ and $\Omega^{\text{write}}_{c,\Delta\phi=\pi}(t)$ is probed. To this end, a suitable control field $\Omega^{\text{read}}_{c}(t)$ to perform a photon production attempt with a subsequent detection using a single-photon counting module (SPCM) is applied.

As it can be seen in Figure 2.19, the storage efficiency for both control pulses oscillates with the overlap of the target mode. Since the two modes with and without the π phase shift are orthogonal to each other and form a complete basis for all intermediate phase jumps, it is expected that each incoming temporal mode $\epsilon_{\text{in},\phi}(t)$ can be decomposed into the two components which are efficiently stored by two control pulses. Consequently, it is expected that the sum of the two curves is constant. However, the green curve for the storage of the shifted photon with $\Omega^{\text{write}}_{c,\Delta\phi=\pi}(t)$ is shifted by approximatively $0.2\,\pi$. Without further investigations, this may be explained by the incapability of the experimental setup to react to an instantaneous phase jump. Also, the storage efficiency for a temporal mode with a phase shift of π and the control field $\Omega^{\text{write}}_{c,\Delta\phi=0}(t)$ to store the photon without a phase shift is significantly above 0 although the two modes should be fully orthogonal.

The initialization fidelity to the $|F{=}1,\, m_F{=}0\rangle$ state is determined to be 0.9 ± 0.02 and the rest of the population is roughly equally distributed among the $|F{=}1,\, m_F{=}\pm 1\rangle$ states. These two states also form Λ-systems for photon storage (see Section 2.4.6), but due to the different set of Clebsch-Gordan coefficients result in a different temporal mode for the ap-

plied control field, which is not orthogonal to the incoming mode. The same is equally valid for the reversed scenario with an unshifted photon and the $\Omega^{\text{write}}_{c,\Delta\phi=\pi}(t)$ control field. The population dynamics of the storage process of an orthogonal mode have not been examined in depth, but the instantaneous phase jump, which makes the temporal mode orthogonal to the target mode stored by $\Omega^{\text{write}}_{c,\Delta\phi=0}(t)$, happens only after the first half of the photon has already interacted with the cavity-system. Hence, it is reasonable to assume that atomic decay processes are involved even if the photonic mode is not stored. Consequently, incoherent decay to the $\left|5^2S_{1/2}, F{=}2\right\rangle$ manifold also contributes to the non-zero observable storage efficiency.

2.5.5. Temporal Mode Conversion

In the last two sections, it was demonstrated that the control fields $\Omega^{\text{read}}_c(t)$ and $\Omega^{\text{write}}_c(t)$ for both the storage and the retrieval processes can be used to individually control the temporal modes that are absorbed and emitted, respectively. This can be leveraged for a temporal mode conversion node in a quantum network. Such a conversion between different temporal modes is a significant feature to create compatibility between quantum systems which may have significantly different internal properties and therefore emit and absorb photons with vastly different shapes and temporal extents. In prior work, conversion between different temporal modes has been demonstrated but was reliant on *cutting out* the desired shape from an incoming photon. Unfortunately, this technique cannot efficiently convert between modes with highly different temporal extents. In this section, the efficient interconversion between photons with a temporal extent of $0.5\,\mu$s and $500\,\mu$s is demonstrated.

To bridge three orders of magnitude in temporal extent, a single atom is loaded into the center of the optical resonator and initialized into $|F{=}1, m_F{=}1\rangle$ ground state by means of optical Zeeman pumping. A photon with a characteristic time of $T_C = 0.5\,\mu$s impinges the cavity, and a corresponding control field $\Omega^{\text{write}}_{c,T_C=0.5\mu\text{s}}(t)$ for this specific temporal mode is applied. After a short storage duration, the photon is emitted again by using the control field $\Omega^{\text{read}}_{c,T_C=500\mu\text{s}}(t)$ to generate a photon with a characteristic time of $T_C = 500\,\mu$s (see Figure 2.20a). The emitted photon is detected by a time-resolved single-photon counting module and the resulting intensity profile of the photonic mode is reconstructed from the binned arrival times after a sufficient number of experimental repetitions. To demonstrate the conversion in both directions, the same experiment is performed for the storage of a long photon with the subsequent emission of a short photon.

The experimental results for the retrieved intensity profiles for both conversion directions are shown in Figure 2.20c. The conversion efficiency from a short photon to a long photon ($0.5\,\mu\text{s} \rightarrow 500\,\mu\text{s}$) is found to be $\eta = 0.22{\pm}0.02$. For the conversion direction from a long to a short photon ($500\,\mu\text{s} \rightarrow 0.5\,\mu\text{s}$), the conversion efficiency is found to be slightly lower with $\eta = 0.17{\pm}0.02$.

As for the mode-selective storage, the efficiency of the absorption process must be lower than expected to explain the missing efficiency in the overall absorption and emission process. Please refer to Section 2.6 for an analysis of the absorption efficiency.

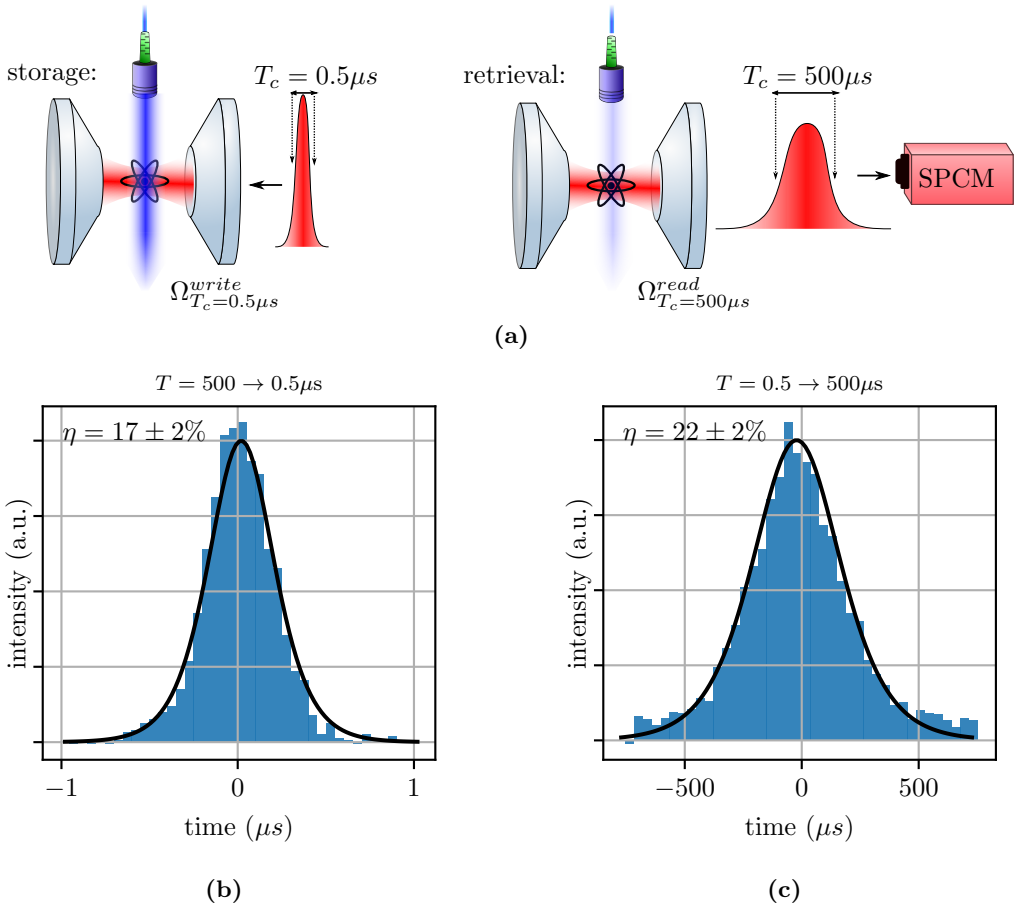

Figure 2.20.: Efficient temporal mode conversion. a) A single σ^+-polarized photon with a characteristic time T_C=0.5 μs is sent into the cavity system and stored by applying a suitable control pulse $\Omega^{\text{write}}_{c,T_C=0.5\mu s}(t)$ on an axis perpendicular to the cavity. Subsequently, the storage process is then reversed and a photon is retrieved from the system by applying a significantly less intense second control pulse $\Omega^{\text{read}}_{c,T_C=500\mu s}(t)$ to create a photon with a characteristic time T_C=500 μs. The photon predominantly leaves the cavity through its output-coupler mirror and is collected by a time-resolved single-photon counting module (SPCM) to evaluate the intensity profile and the efficiency of the process. To demonstrate the conversion in both directions, the experiment is repeated by first storing a photon with a long characteristic time T_C = 500 μs with the subsequent retrieval of a short photon with T_C = 0.5 μs. **b,c)** show the intensity profile and the conversion efficiencies for both conversion directions.

2.6. Photon Absorption Efficiency

As it has been seen in the experimental test of the model, the absorption efficiency is significantly lower than predicted by the model (see Section 2.5.4, 2.5.5). Here, this is further investigated by first checking the impact of using weak coherent pulses on the light-matter interface storage efficiency followed by an investigation of the dependence on the single-photon detuning.

2.6.1. Weak Coherent Pulses

In this section, the implications of using weak coherent pulses instead of single-photon Fock states for the input states are discussed.

The efficiency of the light-matter interface η_{int} is defined as the probability to retrieve

a photon from the cavity when there initially was a single-photon input in the free-space mode which is coupled to the cavity. Due to the lack of a single-photon source, the light-matter interface is probed with weak coherent pulses with an average photon number $\bar{n}$ and a Poissonian distribution of the expectation value of photon number statistics $p_i^{\bar{n}}$ in the individual pulses,

$$p_i^{\bar{n}} = \frac{\bar{n}^i e^{-\bar{n}}}{i!} \ . \tag{2.102}$$

Therefore, the above-mentioned definition is not directly applicable. For $\bar{n}$=1 a significant number of pulses contain more than one photon. Hence, the interface efficiency will be underestimated because at most one excitation can be stored in the atom. In principle, the interface efficiency for single photons can be deduced by using coherent pulses with a low average photon number such that multi-photon events are suppressed by a factor χ compared to the single-photon events,

$$\chi = \frac{p_1^{\bar{n}}}{\sum_{i>1} p_i^{\bar{n}}} = \frac{p_1^{\bar{n}}}{1 - p_0^{\bar{n}} - p_1^{\bar{n}}} = \frac{\bar{n}}{e^{\bar{n}} - 1 - \bar{n}} \ . \tag{2.103}$$

For the suppression of $\chi = 100$ an average photon number of $\bar{n} \approx 0.02$ has to be used.

However, in the later chapter of this work, the interface is used to store polarization qubits. Unfortunately, for $\bar{n} = 0.02$ the combined SPCM dark count rate $\Gamma_{\text{d.c.}} \approx 120\,\text{Hz}$ becomes significant. With a memory efficiency of $\eta_{\text{mem}} \approx 0.22$, a total photon detection efficiency of $\eta_{\text{det}} \approx 0.4$ and a detection interval of $\tau = 6\,\mu\text{s}$ the ratio ζ of measured dark counts to photon counts is given by

$$\zeta = \frac{\Gamma_{\text{d.c.}} \cdot \tau}{\eta_{\text{mem}} \eta_{\text{det}} \cdot \bar{n}} \approx \frac{0.01}{\bar{n}} \tag{2.104}$$

for small $\bar{n}$ such that multi-photon events are suppressed.

Although dark counts can be compensated well in an efficiency calibration, high contributions of dark counts will affect the measured coherence of the retrieved qubit state. To characterize qubit fidelities and for reasonable data rates, an higher average photon number is preferable, and most of the measurement shown in the next chapter have been performed with an input pulse containing $\bar{n} = 1$ photons.

By using ultra-weak coherent pulses with suppressed multi-photon events, the interface efficiency for single-photon Fock state can be determined, and the ratio to the efficiency for weak coherent pulses with $\bar{n} = 1$ can be used to normalize measured efficiencies with weak coherent pulses to resemble the scenario of single-photon Fock states.

2.6.2. Simple Markovian Model

The development of a suitable model to describe the storage efficiency of weak coherent pulses was subject to current research with a recently published result [120]. However, in this work, a simple Markovian model is used to fit the data points.

A Fock state containing multiple photons is modeled as successive storage attempts of single-photon pulses. Each attempt has three possible outcomes: the atomic population is either coherently transferred to the storage S where it remains despite subsequent arriving photons, the population resides in the initial state I, or the population is incoherently

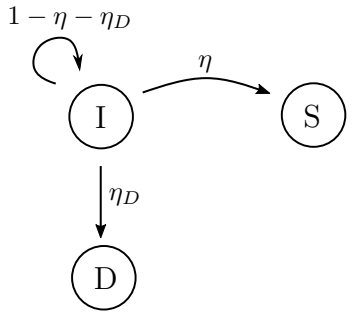

Figure 2.21.: Simple Markovian model for absorption efficiency of weak coherent pulses. The storage of a Fock state containing multiple photons is modeled as the successive storage attempt of single photons with the probability η to actually absorb the photon and transfer the atom to the storage state S, the probability η_D to pump the atom to a dark state D and the remaining likelihood to stay in the initial state I.

transferred to some other state D, where it is unavailable for subsequent storage attempts. The corresponding Markovian chain is depicted in Figure 2.21. The accumulated transfer efficiencies for the n^{th} trial is given by

$$\eta_{S,n} = \eta \sum_{i}^{n} \eta_{I,n}, \quad \eta_{I,n} = (1-\eta-\eta_D)^n, \quad \eta_{D,n} = \eta_D \sum_{i}^{n} \eta_{I,n} \ , \tag{2.105}$$

with the efficiency $\eta_{I,n}$ to remain in the initial state after the n^{th} absorption attempt, the efficiency $\eta_{D,n}$ for the atom to be incoherently transferred to a state unavailable the efficiency $\eta_{S,n}$ for a successful transfer into the storage state after the n^{th} attempt.

A weak coherent pulse is a statistical mixture of Fock states, and within this simple model, the absorption efficiency can be determined by calculating the efficiencies for the individual Fock state components and calculate the weighted sum according to the Poisson distribution.

2.6.3. Interface Efficiency over Average Photon Numbers

To experimentally determine the absorption efficiency for single-photon Fock states, weak-coherent pulses with different average photon numbers $\bar{n}$ are absorbed by the atom-cavity system with a single-photon detuning of Δ=−20 MHz. Subsequently, the photon production protocol is applied, and the overall efficiency is measured by recording the produced photon with a single-photon counting module with a well-calibrated detection efficiency. The resulting efficiency shown in Figure 2.22 is normalized by the average photon number $\bar{n}$. The data points are fitted to the simple Markovian model explained above with the write efficiency η and the efficiency η_D to pump the atom into a dark-state as free parameters.

The fit shows a good agreement with the acquired data points and yields $\eta_D = 0.19$. The absorption efficiency for single-photon Fock states $\eta = 0.365$ can be extracted from the limit $\bar{n} \to 0$ and by normalizing the resulting curve with the known photon emission efficiency. Further, a correction factor of approximatively 1.3 for the ratio between η and the absorption efficiency for weak-coherent pulses with $\bar{n} = 1$ is determined by dividing the normalized efficiency for $\bar{n} \to 0$ by the efficiency for $\bar{n}$=0.

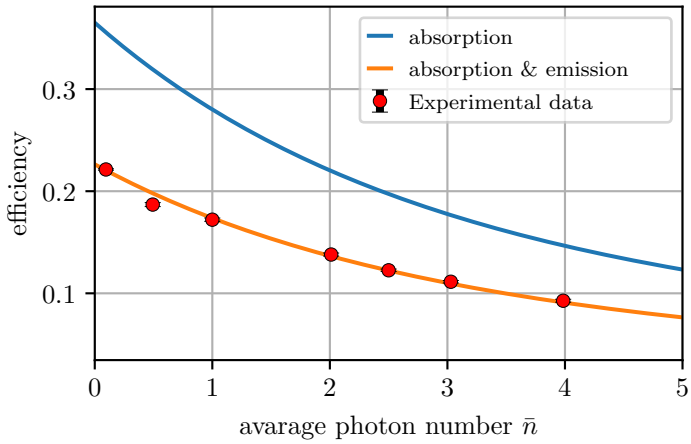

Figure 2.22.: Combined absorption and emission efficiency for weak coherent pulses of different average photon numbers. A weak coherent pulse containing $\bar{n}$ photons on average is impinged onto the cavity and stored by applying the control pulse corresponding to the temporal mode of the photon. Subsequently, the photon emission protocol is performed, and the total efficiency (red points) is measured by detecting the successful emission with a single-photon counting module. The data points are fitted to the Markovian model given in Section 2.6.2 (orange line). By normalizing the total efficiency with the known emission efficiency, the absorption efficiency can be determined (blue line). The error bars correspond to one standard deviation estimated from the sample size and are hidden behind the data points.

This shows that the use of weak coherent pulses with an average photon number $\bar{n} = 1$ underestimates the absorption efficiency by a factor of approximately 1.3. Further, the absorption efficiency is almost a factor 2 smaller than expected. This discrepancy remains unexplained and cannot be attributed to higher photon number components in the weak coherent pulse used to probe the memory.

2.6.4. Absorption Efficiency over Single-Photon Detuning

Here, the absorption efficiency of the light-matter interface is probed for different single-photon detunings, in order to verify that the multi-level model derived in this chapter resolves vanishing absorption efficiency for larger single-photon detunings.

The absorption efficiency is probed for different single-photon detunings Δ by first absorbing a weak-coherent pulse with $\bar{n}$=1 photons with a subsequent emission and detection of the overall efficiency with a single-photon counting module. The experiment is performed with the control field for the absorption $\Omega_c^{\text{write}}(t)$ given by the analytical model presented in Section 2.3 and a second time with the control field $\Omega_G^{\text{write}}(t)$ from the 3-level-model by Gorshkov *et al.* [90]. The photon emission is always performed with the control pulse $\Omega_c^{\text{read}}(t)$ from the multi-level model. The acquired efficiencies are normalized by the expected photon emission efficiency and corrected by the factor 1.3 to resemble the single-photon scenario as discussed in the last section.

The results are shown in Figure 2.23: The green dots indicate the absorption efficiency achieved with the control pulse $\Omega_c^{\text{write}}(t)$ and the blue dots with the control pulse $\Omega_G^{\text{write}}(t)$ from the three-level model by Gorshkov *et al.*. The green line is the theoretical expectation within the multi-level model, scaled by a factor 0.53. The blue line results from rescaling

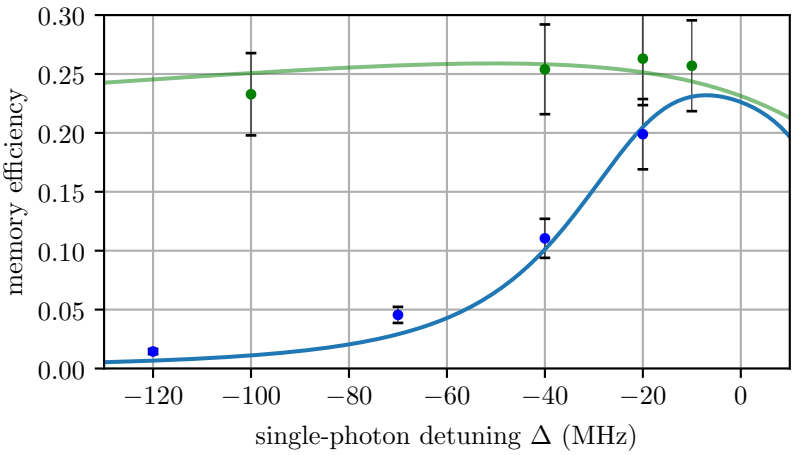

Figure 2.23.: Combined photon absorption and emission efficiency over the single-photon detuning. The photon absorption efficiency is probed as a function of the single-photon detuning with the control field $\Omega_c^{\text{write}}(t)$ acquired from the model derived in the context of this thesis (green dots) and for the control field Ω_G^{write} taken from the 3-level-model by Gorshkov *et al.*. The green line shows the theoretical expectation from the model derived here rescaled by a factor 0.53 to match the experimental results. By calculating the mode overlap between the temporal mode which should be stored within the model by the application of the control pulse Ω_G^{write} with the actual incoming mode the theoretical expectation (green curve) is rescaled (blue curve) to provide the theoretical expectation for the absorption efficiency for the control field Ω_G^{write} within the model derived here.

the green line with the mode overlap between the incoming temporal mode and the mode which should be stored by the $\Omega_G^{\text{write}}(t)$ control field within the multi-level model (see Section 2.4.3.1).

The achieved storage efficiency for the control field $\Omega_c^{\text{write}}(t)$ is a factor 0.53 smaller than expected independent of the single-photon detuning. The origin of this effect had been subject to extensive investigation but could not be resolved in the time-frame of this thesis. It has been found, that decremental effects associated with fluctuations of the control field intensity or phase noise of the laser system scale with the single-photon detuning, but this scaling is not observable rendering the missing absorption efficiency an unresolved issue. The independence of the missing efficiency from the single-photon detuning also suggests the correct compensation of all involved light-shifts.

Despite the unresolved constant factor in the absorptions efficient, the control pulse generated with the theory derived in this chapter performs dramatically better for large single-photon detunings when compared to the achieved efficiency for the control field from the three-level model by Gorshkov *et al.*. By this, the regime of high single-photon detuning becomes available for future experiments relying on controllable light-matter interactions of multiple atoms with the same cavity mode.

2.7. Conclusion

In this chapter, an analytical model for the absorption and emission process of a single photon from a single atom trapped in a high-finesse optical cavity was derived, simulated and experimentally tested. Although a model for those processes has already been derived by Gorshkov *et al.* [90] for a three-level system, it was shown that the predictions diverge

drastically from the physical reality with an increasing single-photon detuning due to the coupling to multiple excited states. Since large single-photon detunings are a necessary requirement for various applications, the existing model [90] was extended to incorporate an arbitrary number of excited states.

The acquired solution correctly predicts the efficiency of the emission process for all single-photon detunings and provides the correct reversible mapping between the emitted and absorbed temporal mode $\epsilon_{\mathrm{in/out}}(t)$ of the photon and the applied control pulse $\Omega_c(t)$. The correctness of the complex-valued emitted temporal modes was verified employing a homodyne detection and decremental effects due to atomic decay processes were studied by numerically integrating the master equation of the full atomic level-structure.

As it has been experimentally demonstrated, the obtained control over the absorbed and emitted temporal modes is not only crucial to achieving an efficient light-matter interface but also enables the selection of a specific temporal mode to be stored. This allows for the multiplexing of quantum information onto a set of orthogonal photonic modes in future quantum network applications. Further, it was demonstrated that the ability to precisely and dependently control the temporal modes to be absorbed and emitted allows for the formation of a temporal mode converter. Such a temporal mode converted can be leveraged to achieve compatibility between different quantum systems in future heterogeneous quantum networks. The obtained model enables to work with large single-photon detunings while maintaining efficient light-matter interactions, and thereby allows for the scaling of atom-cavity systems to multiple atoms with individually controllable cavity interactions.

3.Qubit Storage

The content of this chapter is based on the prior publication:

Decoherence-protected memory for a single-photon qubit
M. Körber, O. Morin, S. Langenfeld, A. Neuzner, S. Ritter & G. Rempe
Nature Photonics, volume **12**, pages 18–21 (2018)

3.1. Motivation and Structure

The efficient exchange of photonic qubits between network nodes and their long-lived storage is essential for the formation of future quantum networks [30, 47, 49]. Hence, the efficiency and the coherence time are the two most important figures of merit for a photonic quantum memory for quantum network applications. In the previous chapter, the efficiency of the atom-cavity based light-matter interface and the control over the temporal modes for the exchange of photonic qubits between network nodes was addressed. Here, the second figure of merit is subject to improvements since the prevailing storage times achievable for photonic qubits memories are insufficient for quantum networks on the global scale.

Photonic quantum memories rely on strong light-matter interactions, and an alternative approach to reach strong light-matter interactions rates without high-finesse resonators is to increase the optical density by employing atomic clouds. In such an ensemble, the photon is stored in a superposition of excitations of the individual atoms, a so-called spin wave. Those systems have been successfully employed to store both photonic qubits [121, 122] or single-photon Fock states [123–127] for DLCZ based protocols [128]. The performance of such systems is limited due to various effects like relative movements, collisions or an inhomogeneous environment like spatial dependent magnetic fields, affecting the phase relation between the excitation stores in the individual atoms. Such collective dephasing mechanisms degrade both the achievable qubit coherence times and the retrieval efficiency of the photonic excitations.
One remarkable advantage of employing a single atom as the matter-based carrier for qubit storage is the abstinence of such collective dephasing mechanisms resulting in time-independent retrieval efficiencies and very large T_1 times, which should in principle allow for long storage times of single-photon Fock states. However, here only the more demanding storage of photonic qubit states is discussed and various mechanisms causing the dephasing of the qubit basis are addressed to prolong the qubit coherence time significantly.

The chapter is structured as follows: First, the original single-atom quantum memory protocol is applied to evaluate improvements achieved since its initial report [96], and for reference. After a short discussion of the dominant decoherence mechanisms, a scheme to transfer the qubit to a decoherence-protected base is investigated. Subsequently, the experimental realization is discussed, and the scheme is applied to the quantum memory. With the experimental results, residual decoherence mechanisms are identified, and their reversibility is discussed. Afterward, a second Raman transfer scheme is implemented, and the experiment is repeated with the application of a spin-echo pulse. Finally, residual decoherence mechanisms are examined and strategies for further improvements are identifies.

3.2. Theoretical Background

In this section, the theoretical background for the storage of polarization qubits is explored. After a brief description of quantum bits, the polarization encoding of a single-photon carrier is introduced. Subsequently, the phase rotation of a qubit due to an energy difference of it's basis states as it is relevant for encoding the qubit state on atomic levels is discussed, followed by the definition of the qubit fidelity which is used to describe the quality of the retrieved qubit state after the storage. The degradation of the fidelity stems from different physical effects on the qubit state and the associated time scales are enumerated. Since an non-ideal quantum memory does not release identical qubit states although the input states where identical, the density formalism to describe statistical mixtures is introduced, followed by the description of the correspondence to the Stokes vector which is used to describe the polarization of an ensemble of photons. Afterwards, the Ramsey spectroscopy is introduced as it is used in this thesis to probe the coherence between atomic states. Finally, the influence of magnetic field fluctuations to the energy of atomic levels as described by the Zeeman effect is introduced and the magnetic guiding technique to reduce the effect of those fluctuation is discussed.

3.2.1. Qubits

In classical information theory, the smallest unit of information is the state of a single entity which is always in one of two discrete states, which are often referred to as *0* and *1*. Such an indivisible piece of information is known as a bit. Analogously, in quantum information theory the quantum bit (qubit) was introduced [129] as the smallest unit of quantum information. In contrast to a classical bit, a qubit is not necessarily in one of the two mutually excluding states, but possibly in a coherent quantum superposition of its basis states. In general, quantum information describes the state of a quantum system and the simplest non-trivial system is the two-level system. By factoring out the global phase term and by using the normalization conditions, $|\alpha|^2 + |\beta|^2 = 1$. a single qubit can be parameterized using two real-valued parameters, the mixing angle θ and the relative phase $\phi_{\text{rel.}}$ [130]:

$$|\psi\rangle = \underbrace{\cos\left(\frac{\theta}{2}\right)}_{\alpha}|0\rangle + \underbrace{\sin\left(\frac{\theta}{2}\right)}_{\beta} e^{i\phi_{\text{rel.}}(t)}|1\rangle \tag{3.1}$$

A pure qubit state can be represented geometrically using the so-called Bloch sphere, where every state corresponds to a point on the surface of the unit sphere (see Figure 3.1).

3.2.1.1. Polarization Qubits

In this work, the polarization degree of freedom is used to encode a qubit onto a single photon. The basis states are chosen to be the left- and right-circular polarization components.

$$|0\rangle \leftarrow |L\rangle \quad \hat{=} \quad \text{left-circular polarization component} \tag{3.2}$$
$$|1\rangle \leftarrow |R\rangle \quad \hat{=} \quad \text{right-circular polarization component} \tag{3.3}$$

Although the choice of basis is in principle arbitrary, here it coincides with the composition used when the photon is mapped on two hyperfine spin-states of a single atom (see Section 3.3).

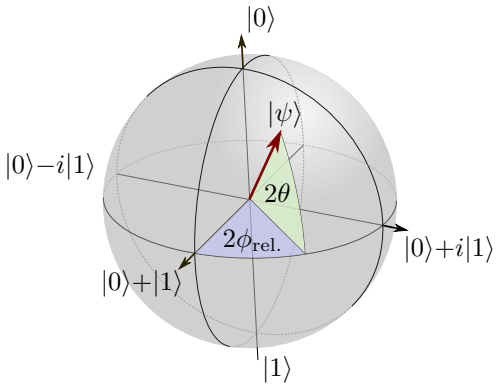

Figure 3.1.: The Bloch sphere. It serves as a geometric representation of pure qubit states. The polar coordinate encodes the mixing angle of the basis states populations, while while the azimuth angle represents the relative phase relation between the basis states.

A balanced superposition of a left- and a right-circular polarization state results in linear polarization state, which is further defined by the phase-relation between the individual components. Those purely linear polarization states can be found in the equatorial plane of the Bloch sphere, while the circular components are located at the poles. The four linearly polarized states are the principle points in the equatorial plane with a relative phase spacing of $\frac{\pi}{2}$. Those linear polarization states are given by

$$|H\rangle := \frac{1}{\sqrt{2}}\left(|R\rangle + |L\rangle\right) \quad \hat{=} \quad \text{horizontal polarization} \tag{3.4}$$

$$|D\rangle := \frac{1}{\sqrt{2}}\left(|R\rangle + i|L\rangle\right) \quad \hat{=} \quad \text{diagonal polarization} \tag{3.5}$$

$$|V\rangle := \frac{1}{\sqrt{2}}\left(|R\rangle - |L\rangle\right) \quad \hat{=} \quad \text{vertical polarization} \tag{3.6}$$

$$|A\rangle := \frac{1}{\sqrt{2}}\left(|R\rangle - i|L\rangle\right) \quad \hat{=} \quad \text{anti-diagonal polarization} \tag{3.7}$$

3.2.1.2. Phase Evolution

For any eigenstate $|\Psi\rangle$ of a quantum system, only the phase evolves in time with a velocity proportional to the energy of the state E_Ψ [131]

$$|\Psi(t)\rangle = |\Psi(t_0)\rangle e^{-iE_\Psi\, t/\hbar}\ . \tag{3.8}$$

For a single eigenstate, the phase term is not an experimentally accessible quantity. However, the state of a qubit is an arbitrary coherent superposition of two such eigenstates and the relative phase between the individual eigenstates evolves with their energy difference

$$\phi_{\text{rel}}(t) = \frac{\Delta E}{\hbar} t \quad \text{with} \quad \Delta E = E_{|1\rangle} - E_{|0\rangle}\ . \tag{3.9}$$

Note, the relative phase defines the azimuthal coordinate on the Bloch sphere and in case of the storage and retrieval of polarization qubits in the $|R\rangle/|L\rangle$ basis, it defines the difference between all linear polarization components. The relation between the relative phase evolution speed and the energy difference of the basis states is the challenging aspect of storing a qubit over an extended period because fluctuations of the energy difference can directly translate into a loss of the phase relation in the ensemble of qubit realizations.

The identification and elimination or compensation of effects associated with a fluctuating energy difference ΔE is the most vital aspect to increase the coherence time of the qubit storage and is a reoccurring theme throughout this chapter.

3.2.1.3. Qubit Fidelity

In contrast to classical information which can be stored almost indefinitely, a qubit is very susceptible to information loss. The purity of an ensemble of qubits can be degraded either by an uncontrolled change of the basis state amplitude coefficients α, β or by the loss of the phase relation $\phi(t)$. The latter is associated with a fluctuating energy difference between the basis states and often referred to as dephasing. The fidelity is the figure of merit to describe the deviation of the qubit state $|\psi_{\text{out}}\rangle$ from the initial state $|\psi_{\text{in}}\rangle$:

$$\mathcal{F} = |\langle\psi_{\text{in}}|\psi_{\text{out}}\rangle|^2, \qquad \mathcal{F} = \langle\psi_{\text{in}}|\rho_{\text{out}}|\psi_{\text{in}}\rangle \ , \tag{3.10}$$

for a pure state $|\psi_{\text{out}}\rangle$ or a mixed state characterized by the density matrix of the state ρ_{out}, respectively. For a constant energy splitting ΔE, the fidelity of a pure state oscillates due to the time evolution of the relative phase:

$$\mathcal{F}(t) = \alpha^4 + \beta^4 + \alpha\beta \cdot \cos\left(\frac{\Delta E}{\hbar} \cdot t + \phi_0\right). \tag{3.11}$$

If the energy splitting fluctuates between experimental realizations, the initially well-defined phase relation $\phi(t)$ becomes a statistical mixture resulting in a degradation of the qubit from a pure state into a mixed state in the ensemble of memory realizations. For a balanced superposition ($\alpha = \beta = 1/\sqrt{2}$) the fidelity oscillates with full contrast, rendering the qubit most susceptible to dephasing. In contrast, a maximally unbalanced state, e.g. $\alpha = 1, \beta = 0$, has no phase relation and therefore cannot dephase. Further analysis of dephasing mechanisms will concentrate on linearly polarised input photons:

$$\mathcal{F}_{\text{linear}}(t) = \frac{1}{2} \cdot \left(1 + \cos\left(\frac{\Delta E}{\hbar} \cdot t + \phi_0\right)\right) \tag{3.12}$$

3.2.1.4. Fidelity Decay Timescales and Reversibility

There are different timescales associated with the decay of the fidelity. Superposition states are susceptible to a loss of the relative phase relation and the associated timescale is referred to as the T_2 time. There are two different classes of processes contributing to the dephasing of an ensemble of spins: the timescale associated with fluctuations in the time domain during the evolution of the phase, T_2^*, and the timescale associated with differences of the phase evolution speeds between different qubits within the ensemble, $T_2^{\text{inhom.}}$. The relation between them is given by

$$\frac{1}{T_2} = \frac{1}{T_2^*} + \frac{1}{T_2^{\text{inhom.}}} \ . \tag{3.13}$$

The description originates from the nuclear magnetic resonance community, where inhomogeneous magnetic fields cause a spatial dependence of the phase evolution speed. For the memory scenario described here, the inhomogeneity corresponds to phase evolution speeds which change between memory realizations but are constant during the evolution time of the qubit. Those inhomogeneous dephasing mechanisms can be compensated by reversing the phase evolution by the application of the spin echo technique [132]. In contrast, fluctuations during the phase evaluation which result in a different net evolution before and after

the spin echo pulse are not compensated. By the application of multiple spin-echo pulses up to a continuous driving, faster noise contributions can be eliminated [133, 134].

In contrast, states which are stored on a single eigenstate of the memory system cannot dephase. However, the fidelity of all states can also degrade by a change of the population amplitudes $|\alpha|$, $|\beta|$. The associated timescale, the so-called relaxation-time, is referred to as the T_1 time. In general, the dephasing time is always shorter than twice the relaxation time [135],

$$2T_1 > T_2 \ . \tag{3.14}$$

3.2.1.5. Representation of Mixed States

In the case of a non-ideal quantum memory, the qubits in the ensemble of memory realizations do not behave identically but diverge over time. As described above, this will result in a degradation of the qubits fidelity since the state of this ensemble becomes a statistical mixture. To express such a quantum state, which can be described as a probabilistically weighted incoherent sum of pure states [136], the density matrix formalism is a suitable description [137–139]:

$$\hat{\rho} = \sum_i p_i |\psi_i\rangle\langle\psi_i| = \begin{pmatrix} A & Ce^{i\phi} \\ Ce^{-i\phi} & B \end{pmatrix}_{|0\rangle,|1\rangle} \text{ with } \sum p_i = A + B = 1,\ C \leq \sqrt{AB} \tag{3.15}$$

Here, A is the probability of finding the system in $|0\rangle$ and B the probability for $|1\rangle$, respectively and the off-diagonal terms describe the coherence between $|0\rangle$ and $|1\rangle$. In the $|R\rangle$ and $|L\rangle$ basis, the density matrix of an incoherent mixture with equal probabilities of $1/2$ is given by

$$\hat{\rho}_{\text{mixed}} = \frac{1}{2}\begin{pmatrix} 1 & 0 \\ 0 & 0 \end{pmatrix} + \frac{1}{2}\begin{pmatrix} 0 & 0 \\ 0 & 1 \end{pmatrix} = \frac{1}{2}\begin{pmatrix} 1 & 0 \\ 0 & 1 \end{pmatrix}. \tag{3.16}$$

In contrast, the fully coherent superposition state $|H\rangle$ has the density matrix

$$\hat{\rho}_{\text{coherent}} = \frac{1}{2}\begin{pmatrix} 1 & 1 \\ 1 & 1 \end{pmatrix}. \tag{3.17}$$

Note that due to the normalization, the diagonal elements of a density matrix always sum up to unity. The trace of the square of the density matrix is a measure for the purity of the state, which is 1 for pure states and $1/2$ for incoherent mixtures:

$$Tr\left(\hat{\rho}\right) = 1, \quad 1 \geq Tr\left(\hat{\rho}^2\right) \geq \frac{1}{2} \tag{3.18}$$

3.2.1.6. Stokes Parameter & Photonic Qubit Tomography

The density matrix of a polarization qubit can be expressed by the so-called Stokes vector [96, 136, 140]

$$\hat{\rho} = \frac{1}{2}\sum_{i=0}^{3} S_i \hat{\sigma}_i \tag{3.19}$$

with the Pauli matrices

$$\hat{\sigma}_0 = \begin{pmatrix} 1 & 0 \\ 0 & 1 \end{pmatrix}, \quad \hat{\sigma}_1 = \begin{pmatrix} 0 & 1 \\ 1 & 0 \end{pmatrix}, \quad \hat{\sigma}_2 = \begin{pmatrix} 0 & -i \\ i & 0 \end{pmatrix}, \quad \hat{\sigma}_3 = \begin{pmatrix} 1 & 0 \\ 0 & -1 \end{pmatrix}. \tag{3.20}$$

The first entry of the Stokes vector, S_0, corresponds to the intensity of the light field and in the case of single photons, it is set to 1. The other three entries correspond to the outcome of a projective measurement,

$$S_1 = P_{|H\rangle} - P_{|V\rangle} = 2P_{|H\rangle} - 1 \ , \tag{3.21}$$

$$S_2 = P_{|D\rangle} - P_{|A\rangle} = 2P_{|D\rangle} - 1 \ , \tag{3.22}$$

$$S_3 = P_{|R\rangle} - P_{|L\rangle} = 2P_{|R\rangle} - 1 \ , \tag{3.23}$$

with the projection operator

$$P_{|\psi\rangle} = \langle\psi|\hat{\rho}|\psi\rangle \ . \tag{3.24}$$

Here, S_1 represent the probability to detect a $|H\rangle$ photon when measured in the $|H\rangle/|V\rangle$ basis and S_2 and S_3 for the $|D\rangle/|A\rangle$ and $|R\rangle/|L\rangle$ bases accordingly. The length of the vector formed by those three components $|S_{1,2,3}|$ is called *the degree of polarization* and corresponds to the purity of the polarization state of the photon and can be related to the trace of the square of the density matrix of the qubit state [96, 136, 140]:

$$2Tr(\hat{\rho}^2) - 1 = |\vec{S}| \ . \tag{3.25}$$

The qubit tomography allows reconstructing the density matrix of a qubit state in multiple measurements given the ability to create a sufficiently large ensemble of qubits. With the definition of the Stokes vector, the reconstruction is obtained by repeatedly measuring the polarization of the qubit in three linear independent basis sets which correspond to the individual entries of $S_{1,2,3}$.

3.2.1.7. Coherence Time Measurement with a Ramsey Sequence

Originally developed to accurately measure resonance frequencies, the Ramsey sequence became a standard tool to measure dephasing times (T_2) of two-level systems [141–143]. To this end, the system is prepared in one of the basis states corresponding to the poles of the Bloch sphere. By the application of a $\pi/2$-pulse, the system is prepared in a coherent superposition $|\psi\rangle = \sqrt{2}^{-1}\left(|0\rangle + e^{-i\phi}|1\rangle\right)$ which corresponds to a state in the equatorial plane of the Bloch sphere. During a variable-length free-evolution period τ the state evolves before a second $\pi/2$-pulse is applied. Finally, the population of the basis states is projectively measured. The sequence is depicted in Figure 3.2.

As discussed in Section 3.2.1.2, the azimuthal angle is given by the relative phase relation ϕ_0 between the basis states and evolves with a velocity proportional to the energy difference of basis states, $\phi(t) = \frac{\Delta E}{\hbar}t + \phi_0$. In the rotating frame of the driving field, the phase evolution speed is reduced to the frequency difference between the transition and the driving field. For a non-vanishing phase evolution, the result of the final population measurement performed after the second $\pi/2$-pulse oscillates due to the rotation of the state vector around the equatorial plane during the free-evolution time. Those oscillations are known as Ramsey fringes and can be utilized to determine the transition frequency with high precision [141]. As discussed above (see Section 3.2.1.4), dephasing is linked to a fluctuating energy splitting of the basis states. Over time, those fluctuations result in an increasingly uniform distribution of state vectors within the equatorial plane. Consequently, the oscillation amplitude of the Ramsey fringes is damped on a time scale corresponding to the dephasing time (T_2).

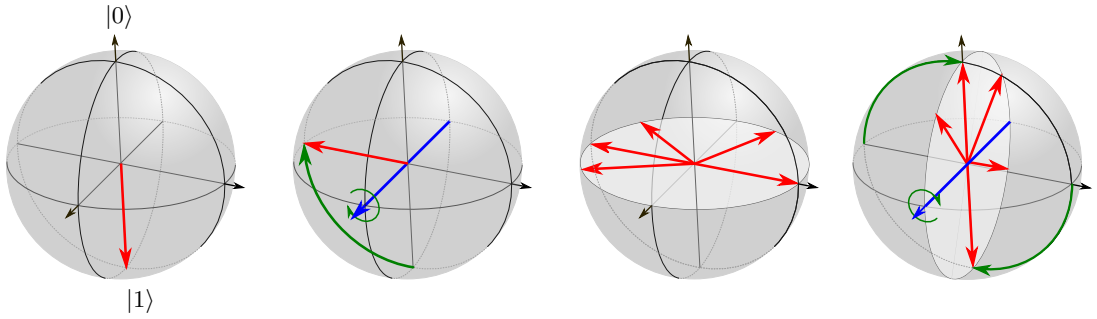

Figure 3.2.: Ramsey sequence. To probe the coherence time of a pair of states, a coherent superposition is prepared by the application of a $\pi/2$-pulse. This rotates the state into the equatorial plane (green arrow) around a given axis (blue arrow). Due to dephasing mechanisms, the state vectors (red arrows) are increasingly uniformly distributed after a variable-length free-evolution time. Subsequently, a second $\pi/2$-pulse is applied, and the population distribution of the basis states is probed.

In the context of this thesis, this method is used to determine the coherence between qubit basis pairs which are not compatible with photonic qubit storage. Experimental results obtained with this method can be found in Section 3.3.4.1 and Section 3.4.4.

3.2.2. Zeeman Splitting

In this work, a photonic polarization qubit is mapped onto a superposition of two atomic Zeeman substates. Since the relative phase of the qubit, $\phi_{\text{rel.}}(t)$ evolves with the energy difference of the qubit's basis states, the differential Zeeman shift and its dependence on the magnetic field is of crucial importance for the coherence properties of the memory.

Given a magnetic field along the quantization axis y, $|\vec{B}| = B_y$, the Zeeman splitting for the substates in the $5^2S_{1/2}$ hyperfine ground-state manifold with $F = I \pm 1/2$ and $m_F \in \{-1, 0, 1\}$ is given by the Breit-Rabi formula [144]:

$$\Delta E\left(I \pm 1/2, B_y, m_F\right) = -\frac{\Delta E_{\text{hfs}}}{8} + g_I \mu_B m_F B_y \pm \frac{\Delta E_{\text{hfs}}}{2}\sqrt{1 + m_F \frac{\left(g_J - g_I\right)\mu_B B_y}{\Delta E_{\text{hfs}}} + \left(\frac{\left(g_J - g_I\right)\mu_B B_y}{\Delta E_{\text{hfs}}}\right)^2}\,. \quad (3.26)$$

Here, ΔE_{hfs} is the hyperfine splitting, μ_B the Bohr magneton, g_I is the nuclear g-factor, g_J is the fine-structure Landé g-factor and $I = 3/2$ is the nuclear angular momentum. The $5^2S_{1/2}$ ground state has no orbital momentum L such that only the spin $S = 1/2$ contributes to the total electron angular momentum J. The nuclear and electronic angular momenta can be either in a parallel or anti-parallel configuration resulting in a total of two possible configurations of the total atomic angular momentum $F \in \{1, 2\}$. In the regime of weak magnetic fields, the Breit-Rabi formula for states with $m_F \in \{-1, 0, 1\}$ can be linearly approximated [145].

$$\Delta E\left(I \pm 1/2, B_y, m_F\right) = -\frac{\Delta E_{\text{hfs}}}{8} + g_I \mu_B m_F B_y \pm \left(\frac{\Delta E_{\text{hfs}}}{2} + \frac{1}{4} m_F (g_J - g_I)\mu_B B_y\right) \quad (3.27)$$

3.2.3. Magnetic Guiding Field

A well-known technique to reduce the effects of magnetic field fluctuations to the coherence of a qubit is the application of a bias magnetic field B [96]. For a given field strength

$$|B| = \sqrt{(B_x + \delta_x)^2 + (B_y)^2} \tag{3.28}$$

with a variation δ_x in x-direction, which is small compared to the total field strength, $|\delta_x| \ll |B|$, the sensitivity of the energy splitting to the variation is given by

$$\frac{\partial \Delta E}{\partial \delta_x} \propto \frac{\partial |B|}{\partial \delta_x} = \frac{B_x + \delta_x}{|B|} = \begin{cases} 1 & \text{for} \quad B_y = 0 \rightarrow \delta_x \parallel B \\ \delta_x/|B| \approx \delta_x/|B_y| & \text{for} \quad B_x = 0 \rightarrow \delta_x \perp B \end{cases} . \tag{3.29}$$

For a variation δ_x orthogonal to the magnetic guiding field B, the influence to the total magnetic field and the energy splitting is suppressed by the strength of the magnetic field. In contrast, for a variation aligned with the magnetic field, the influence is independent of the field strength. Conclusively, a bias field linearly suppresses the sensitivity of the energy splitting ΔE to contributions of magnetic field noise orthogonal to the direction of the magnetic field B. Unless permanent magnets are used [146] instead of magnetic field coils, the creation of the guiding field introduces additional noise due to imperfections of the involved currents sources. Since the amplitude of fluctuations increases with the applied field strength, the guiding field can have an adverse effect when chosen thoughtlessly.

3.3. Single-Atom Quantum Memory

In this section, the storage of a single-photon polarization qubit on two spin-states of a single ^{87}Rb atom trapped in a high-finesse optical resonator is introduced. The protocol was initially realized by Specht *et al.* [96, 147] and builds the foundation for the more advanced decoherence-protected storage demonstrated in this thesis. Therefore, the discussion is kept brief and will be focused on improvements and changes. Further details can be found in the aforementioned initial reports [96, 147].

3.3.1. Photonic polarization qubit storage

An incoming single photon encodes a qubit state $|\psi\rangle$ in a coherent superposition of its left- and right-circular polarization components,

$$|\psi\rangle = \alpha|\sigma^-\rangle + \beta e^{-i\phi}|\sigma^+\rangle \quad \text{with} \quad \alpha^2 + \beta^2 = 1 . \tag{3.30}$$

To map this qubit onto a single atom, the light-matter interface discussed in chapter 2 is utilized in a dual-rail configuration: The atom is initialized in the $|F{=}1,\, m_F{=}0\rangle$ state and both the left- and right-circular polarization components of the cavity mode couple to an excited state. By the application of a π-polarized control field with Rabi frequency $\Omega_c(t)$, a Λ-system is formed for both polarization components and the atomic population is coherently transferred to a coherent superposition of two Zeeman substates $|F{=}2,\, m_F{=}\pm 1\rangle$ (see Figure 3.3),

$$\alpha|\sigma^+\rangle + \beta e^{-i\phi}|\sigma^-\rangle \mapsto \alpha\,|F{=}2,\ m_F{=}{-1}\rangle + \beta e^{-i\phi}\,|F{=}2,\ m_F{=}1\rangle \ . \tag{3.31}$$

After a variable storage time, the photonic qubit can be retrieved by reversing the storage process i.e., by applying the time-reversed and complex-conjugated control pulse used for the storage process (see Section 2.3).

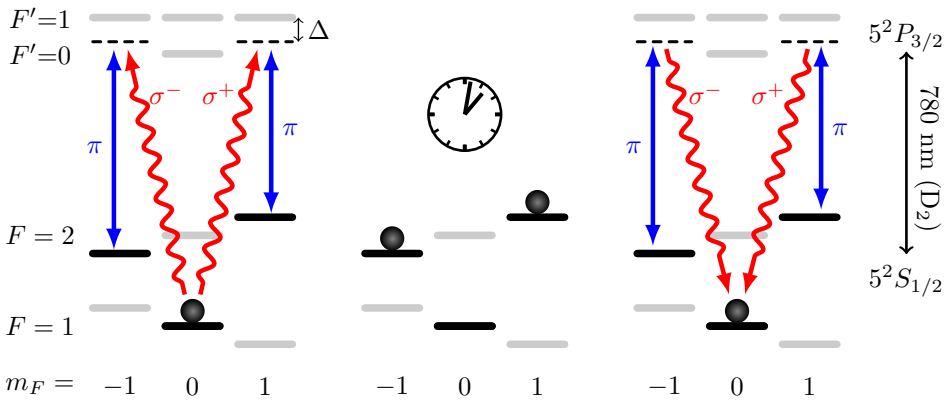

Figure 3.3.: Protocol for the photonic polarization qubit memory. After the ^{87}Rb atom was initialized in the $|F{=}1, m_F{=}0\rangle$ ground state, the incoming photonic polarization qubit (red curly arrows) enters the cavity. Up to a single-photon detuning Δ, depicted as the dashed black lines, the cavity is resonant with the $|F{=}1\rangle \leftrightarrow |F'{=}1\rangle$ transition of the D_2 line. Simultaneously with the entering photon, a π-polarized control field (blue arrow) impinges onto the atom on an axis perpendicular to the cavity axis. The photon in the cavity and the control field are in two-photon resonance with the $|F{=}1\rangle \leftrightarrow |F{=}2\rangle$ ground state transition. The left- and right-circular polarization components (σ^- and σ^+) are individually mapped onto the two Zeeman substates, $|F{=}2, m_F{=}{-}1\rangle$ and $|F{=}2, m_F{=}1\rangle$, respectively. After a variable-length storage duration, the mapping process is reversed by impinging the time-reversed control field, and the photon is emitted into the cavity mode.

3.3.2. Experimental Realization

3.3.2.1. Atomic-State Preparation

Before every individual storage and retrieval attempt, optical molasses cooling [148] is applied for 1 ms to a single atom trapped in the center of a Fabry-Pérot high-finesse optical resonator. Subsequently, the atom is cooled into the motional ground state along the motional principle axis parallel to the cavity axis by means of Raman sideband cooling [118, 149, 150]. To this end, a sequence cooling cycles is applied, and in each cooling cycle, the atomic population is coherently pumped from $|F{=}1\rangle$ to $|F{=}2\rangle$ by removing one motional quantum. Due to the magnetic guiding field applied in the direction of the cavity axis, the Raman sideband transfer is Zeeman state resolving. Therefore, a series of three π pulses are applied, each addressing one of the three possible Zeeman substates. Subsequently, the atomic population is reinitialized to the $|F{=}1\rangle$ manifold employing incoherent hyperfine pumping [118]. After 30 cooling cycles less than 0.01 motional quanta are left along the cavity axis. Finally, a sequence of 10 Zeeman pumping cycles is applied to initialize the atom in the $|F{=}1, m_F{=}0\rangle$ with a residual atomic population of in the $|F{=}1, m_F{=}\pm 1\rangle$ state of approximatively $(4 \pm 1)\%$.

3.3.2.2. Input State Generation

Due to the lack of a single-photon source, the memory is probed with weak coherent pulses. An accousto optical modulator (AOM) is used to shift the light into resonance with the optical resonator and to cut-out a hyperbolic secant shaped amplitude profile with a characteristic time of $T_c{=}1$ ms for the input state. Subsequently, the pulse is attenuated by a neutral density filter down to a single-photon level. A polarization filter is used to reduce the pulse to a well defined linear polarization, and a motorized $\lambda/2$ and $\lambda/4$ waveplate is used to rotate the input photon to the desired polarization state. Through a 99:1 beam-

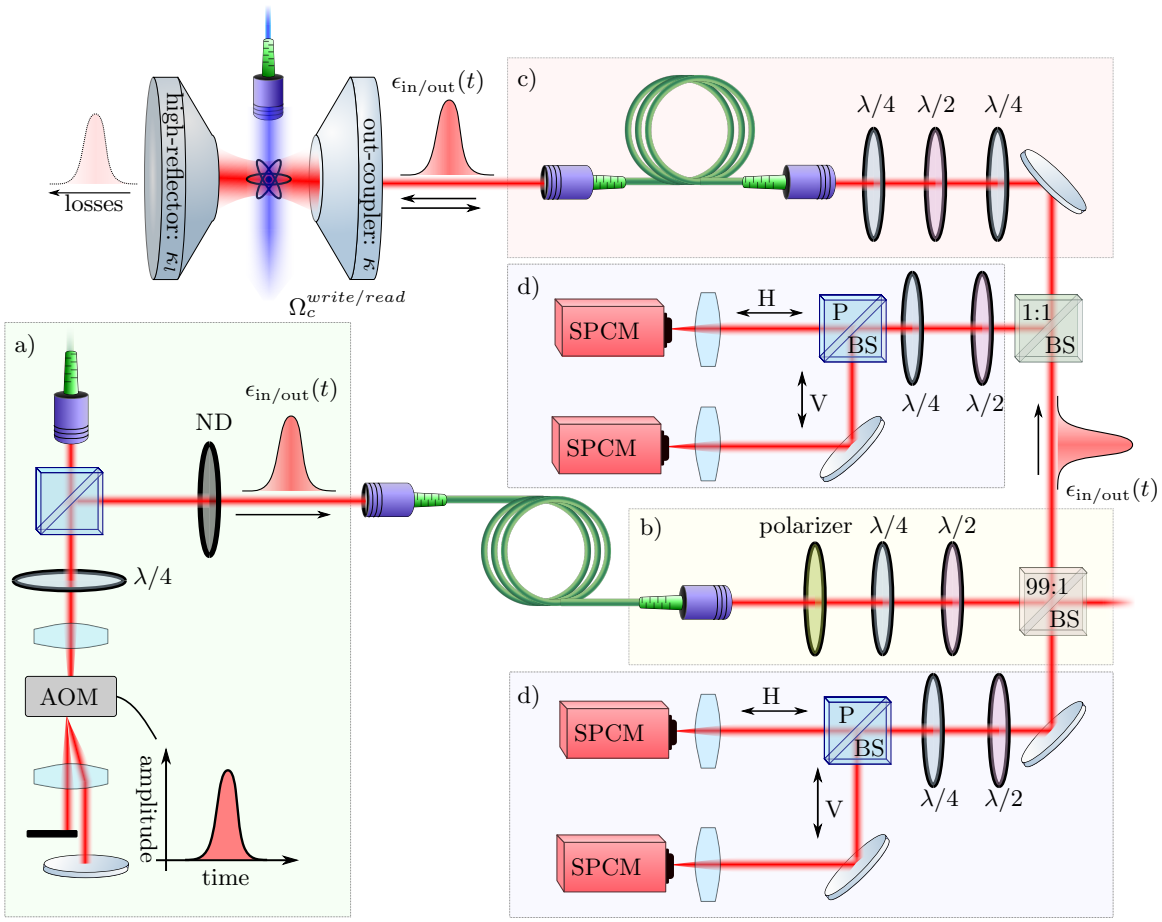

Figure 3.4.: Polarization qubit creation and detection setup. For the creation of a qubit input state, the desired temporal mode is created with an acousto-optical modulator (AOM) from a macroscopic beam which is subsequently reduced to a single-photon level with a neutral density filter (ND) (**a**, green box). Subsequently, the input state is reduced to a well-defined linear polarization utilizing a polarizer and set of a $\lambda/4$ and a $\lambda/2$ waveplate allows to rotate the state into the desired polarization. With a 99:1 beamsplitter, the created state is injected into the free-space mode (**b**, yellow box) which is subsequently coupled to a birefringence-compensated optical fiber (**c**, red box) which guides the photon to the free-space mode that couples to the cavity. In the read-out process, the same fiber guides the created photon to the detection setup in which a set of motorized waveplates (**d**, blue boxes) allows for the selection of the detection basis by splitting the photon into two orthogonal components which are individually detected by a single-photon counting module (SPCM).

splitter, the pulse is injected into the beam path which is guided to the cavity (see Figure 3.4).

The weak coherent pulse in the free-space mode coupled to the cavity contains $\bar{n}$=1 photons on average. The amplitude of the incoming pulse can be controlled via the amplitude of the radio-frequency input of the AOM. By reflecting an input state on the unlocked cavity with a subsequent detection with the single-photon detectors, the photon amplitude can be calibrated given that the transmission to the SPCMs and their quantum efficiency is known (see Section A.6). Note that the overlap between the mode reflected on the cavity which is coupled back to the fiber and the free field mode coupled to the cavity is not unity and must be carefully evaluated.

3.3.2.3. Qubit Storage and Retrieval

To optimize the efficiency of the photon absorption and emission process while minimizing incoherent scattering processes (see Section 2.3 and 2.4.6), a single-photon detuning of Δ=−20 MHz between the cavity mode and the $|F{=}1,\, m_F{=}0\rangle \rightarrow |F'{=}1, m_F{=}1\rangle$ transition is chosen. Simultaneously with the impinging input state, the π-polarized control pulse $\Omega_c^{\mathrm{write}}(t)$ tailored for storing the temporal mode (see Section 2.4.3) of the incoming photon is applied to the atom on an axis perpendicular to the cavity. After a variable storage duration, the qubit is retrieved by applying the time- and phase-reversed control pulse $\Omega_c^{\mathrm{read}}(t)$ (see Section 2.4.3).

3.3.2.4. Polarization Qubit Detection

A single photonic excitation in the cavity mode is predominantly coupled out through the high-transmission mirror of the cavity (T_{OC} = 101ppm). The corresponding free-space mode is subsequently coupled to a non-polarization maintaining optical fiber with a coupling efficiency $\eta_{\mathrm{fc}} = \frac{I_{\mathrm{output}}}{I_{\mathrm{input}}} \approx 0.9$. The fiber guides the single photon to an optically isolated box in which a set of two $\lambda/2$ waveplates and a $\lambda/4$ waveplate is used to compensate for the birefringence induced by the guiding fiber. Further downstream, the beam is divided into two optical paths employing a non-polarizing beamsplitter. In each path, a polarizing beamsplitter is used to decompose the incoming photon into its horizontal and vertical polarization components which are subsequently focused down to the detection area of a total of four single-photon counting modules (SPCM). The SPCMs have an average quantum efficiency of $\eta_{\mathrm{det}} \approx 0.4$ with an average dark count rate of $\Gamma_{\mathrm{d.c.}} \approx 20\,\mathrm{Hz}$. Before the polarizing beamsplitter, a pair of a motorized $\lambda/2$ waveplate and a $\lambda/4$ waveplate rotates the incoming polarization state to set the detection basis to an arbitrary set of orthogonal components. A 99:1 non-polarizing beamsplitter allows injecting counterpropagating light into the beam path. By this, the input state can impinge on the cavity without significant loss of the retrieved quantum state.

To reconstruct the polarization state of the retrieved photon, a tomography is performed on an ensemble of identical memory realizations by measuring the three polarization components $S_{1,2,3}$ of the Stokes vector (see Section 3.2.1.6). The detection basis can be chosen by rotating the $\lambda/2$ waveplates and $\lambda/4$ waveplate in front of the SPCMs. This procedure is repeated for six different input states, the two circular components $|L\rangle$, $|R\rangle$, and the four linear polarizations $|H\rangle$, $|V\rangle$, $|D\rangle$ and $|A\rangle$.

3.3.3. Experimental Results

As discussed in Section 3.3.1, linear polarizations are mapped onto a balanced superposition of atomic eigenstates while a circular polarization is mapped onto a single state. Therefore, linear polarization states are susceptible to dephasing effects whereas circular polarizations are not. Consequently, to probe the coherence time of the quantum memory, a horizontally polarized photon is mapped onto the atom, retrieved after a variable time and detected in the corresponding H/V basis. Additionally, the memory is probed with right circular polarized photons which are detected in the corresponding R/L basis.

As shown in Figure 3.5, the circular polarization (blue) is read out with a constant fidelity independent of the storage duration. In contrast, the fidelity of the horizontally polarized input state evolves with a damped oscillation. The oscillation frequency stems from the magnetic guiding field applied in along the quantization axis to suppress fluc-

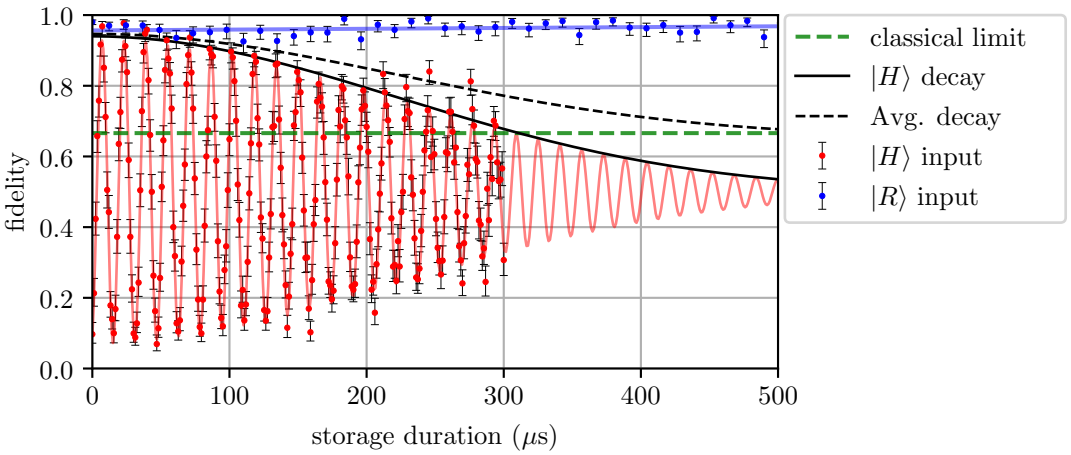

Figure 3.5.: Fidelity over storage time. For the storage of either a right-circular polarized input state (blue dots) or a horizontally-polarized input state (red dots), the fidelity of the retrieved state is probed as a function of the storage duration. The fidelity of the $|H\rangle$ input state is fitted to a Gaussian damped oscillation, and the fidelity for the $|R\rangle$ state is fitted to the constant function. The solid black line shows the Gaussian decay of the $|H\rangle$ input and the black dashed line is the weighted average decay of the linear and circular input polarization. The green dashed line indicates the performance limit of a classical device for single-photon inputs [96]. The error bars show the standard deviation estimated from the sample size.

tuations in orthogonal direction (see Section 3.2.3). The induced Zeeman shift splits the frequency of the qubit basis by $2\delta_L$, causing the precession of the qubit as described in Section 3.2.1.2 and renders the atomic qubit a highly sensitive magnetic field probe. From the fit of the data shown in Figure 3.5, a Zeeman shift $\delta_L \approx (31.454\pm0.002)\,\mathrm{kHz}$ can be extracted which corresponds to an applied magnetic guiding field parallel to the cavity axis of approximatively $B_y\approx45.06\,\mathrm{mG}$.

The coherence time of the memory is extracted from the damping of the fidelity oscillation. For the horizontal polarization, this is shown as the solid black line, and the black dashed line indicates the weighted average of the linear and circular polarization. Note that the average linear fidelity is defined as the average over a set of four orthogonal linear input polarizations ($|H\rangle$,$|V\rangle$,$|A\rangle$ and $|D\rangle$) and the two circular input polarization ($|R\rangle$, $|L\rangle$). However, the qubit's sensitivity to phase fluctuations is equal for all linear polarizations, and the two circular polarizations are equally insensitive to dephasing effects. Therefore, for estimating the coherence time it suffices to measure only one horizontal polarization and one circular polarization to calculate the average fidelity with weights of 2/3 and 1/3.

The fidelity $\mathcal{F}$ of the $|H\rangle$ input state fits well to a Gaussian damped oscillation with a characteristic decay time $\tau_{|H\rangle} = (222.9\pm6.6)\,\mu\mathrm{s}$. Averaged with the constant fidelity of the $|R\rangle$ input state, the qubit fidelity stays above the classical limit for $(615\pm6)\,\mu\mathrm{s}$. Compared to prior work by Specht at al. [96] this is an improvement by a factor two. Also noteworthy, in [147] a maximal fidelity for horizontal polarization of 0.81 for a storage time of $1.2\,\mu\mathrm{s}$ is reported. Here, the fidelity of $|H\rangle$ for short storage duration extracted from the fit is 0.929±0.007 which is an improvement by a factor of ≈2.7 in infidelity (defined as $1-\mathcal{F}$). The fidelity for circular polarizations was increased from approximatively 0.9 to 0.956±0.004. The efficiency of the storage and retrieval process was determined to be (22±2)% for single photon inputs independent of the storage duration. See Section 2.6 for an analysis of the interface efficiency.

3.3.4. Magnetic-Noise-Induced Decoherence

To improve the coherence time of the quantum memory, the primary source of decoherence must be identified first. Here, the impact of normal distributed magnetic field fluctuations is investigated. As discussed in Section 3.2.1.2, decoherence can be induced by a fluctuation of the energy splitting which affects the phase evolution speed.

Given the energy splitting corresponding to two Larmor quanta and the corresponding Larmor frequency

$$\Delta E = 2\mu g_F B_0 \ , \qquad \omega_L = \Delta E \ \hbar^{-1} \ , \tag{3.32}$$

such that the fidelity oscillates with (see Section 3.2.1.2)

$$\mathcal{F}(t) = \frac{1}{2}\left(1 + \cos\left(\omega_L t\right)\right) \ . \tag{3.33}$$

With normal-distributed fluctuations of the magnetic field around B_0 with the variance of σ_B^2,

$$P(B, \sigma_B^2) = \sqrt{2\pi\sigma_B^2}^{-1} \exp\left(-\frac{(B - B_0)^2}{2\sigma_B^2}\right), \tag{3.34}$$

and the assumption that the changes are slow compared to the duration of a single storage attempt, such that the phase evolution speed is constant during a single memory instance, the resulting fidelity dynamics can be determined by convolving the $\mathcal{F}$ and P

$$\mathcal{F}(t, \sigma_B) = \int \mathcal{F}(B, t) P(B, \sigma_B^2)\, dB \tag{3.35}$$

$$= \frac{1}{2}\left(1 + e^{-t^2/2\tau^2} \cos\left(f_L t\right)\right) \qquad \text{with } \tau = \frac{h}{2\sigma_B^2 \mu_B g_F} \tag{3.36}$$

resulting in a Gaussian decay term which damps the fidelity oscillation. The time constant τ of the damping is directly related to the variance σ_B^2 of the magnetic field. For the characteristic decay time $\tau{\approx}223\,\mu$s measured in Section 3.3.3, the variance of the magnetic field is approximatively $\sigma_B{\approx}3.2\,$mG. Compared to the strength of the guiding field $B_y = 0.44\,$mG, the variance in the magnetic field is roughly 7.2% of the overall guiding field and approximatively 2% of the total magnetic field applied to compensate the earth's magnetic field in the direction of the quantization axis.

3.3.4.1. Ramsey Spectroscopy

In the atomic-clock community, the *clock-state* transition

$$|F{=}1,\ m_F{=}0\rangle \leftrightarrow |F{=}2,\ m_F{=}0\rangle \tag{3.37}$$

is well known for its long coherence time [151] due to its insensitivity to magnetic field fluctuations. Here, it serves as a reference to confirm magnetic field fluctuations as the dominant source of decoherence by performing a Ramsey spectroscopy (see 3.2.1.7) on the *clock-state* transition.

After preparing the atom into the $|F{=}1,\, m_F{=}0\rangle$ by means of Zeeman pumping, a coherent superposition with the $|F{=}2,\, m_F{=}0\rangle$ state is prepared by driving a $\pi/2$-transition with a microwave field with $T_{\pi/2}{\approx}600\,\mu$s. During the free-evolution period, the microwave

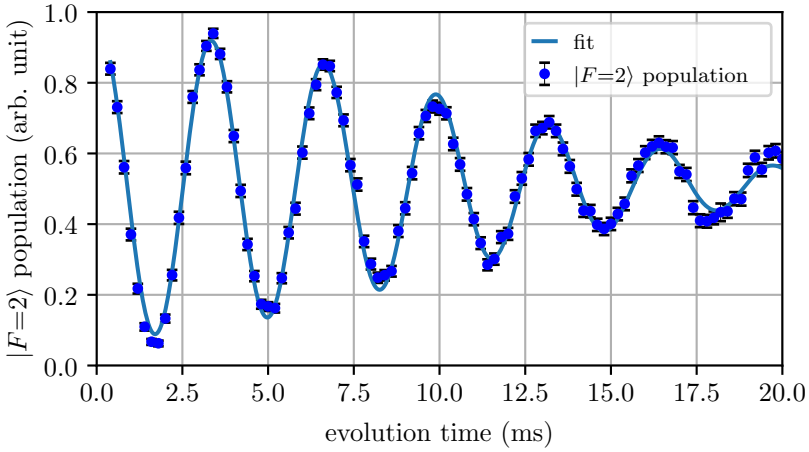

Figure 3.6.: Ramsey spectroscopy. To confirm fluctuations of the magnetic field as the dominant source of decoherence, the coherence time of a magnetically insensitive transition is probed employing a Ramsey spectroscopy. By deliberately adding a small detuning during the free evolution time, Ramsey fringes are induced to help to differentiate between accidentally chosen detunings and actual decoherence. The coherence time corresponds to the time constant of the damping of the population oscillation. The error bars show the standard deviation estimated from the sample size.

is slightly detuned from the transition frequency to create Ramsey fringes. This is done on purpose to distinguish a population decay due to a small accidental detuning from actual decoherence. The final population measurement is done using a cavity-assisted hyperfine state detection [152]. In Figure 3.6 the resulting population of $|F{=}2, m_F{=}0\rangle$ is shown as a function of the free evolution duration. A Gaussian envelope damps the oscillation of the population with a characteristic decay time $\tau{\approx}(9.6 \pm 0.2)\,\mathrm{ms}$ which is significantly longer compared to the coherence between the memory basis states $|F{=}2, m_F{=}{-}1\rangle$ and $|F{=}2, m_F{=}1\rangle$. This is a strong indication that magnetic field fluctuations are the dominant source of decoherence. The decay of the coherence on the timescale of several milliseconds hints towards additional decoherence mechanisms. This will be subject to further investigations in chapter (see Section 3.4.4).

3.3.4.2. Extending Coherence Time by Cleaning up the Magnetic Environment

The first step towards longer coherence times was the elimination of magnetic-noise sources in the vicinity of the atom-cavity system. This included the removal of commercial power supplies for photodiodes, the decommissioning of a flow box above the optical table, and moving of many electronic devices further away from the atom-cavity system. Although this approach is limited, the significant increase in coherence time observable for a horizontally polarized input state (see Figure 3.7) further supports the assumption that magnetic field fluctuations are the primary source of decoherence. Note that for the data shown in Figure 3.7, the readout times have been synchronized with the rephasing times of the Larmor precession to allow for faster data acquisition. The determined decay time of the $|H\rangle$ input state is $\tau_{|H\rangle} = (604 \pm 20)\,\mu\mathrm{s}$ compared to $223\,\mu\mathrm{s}$ observed above.

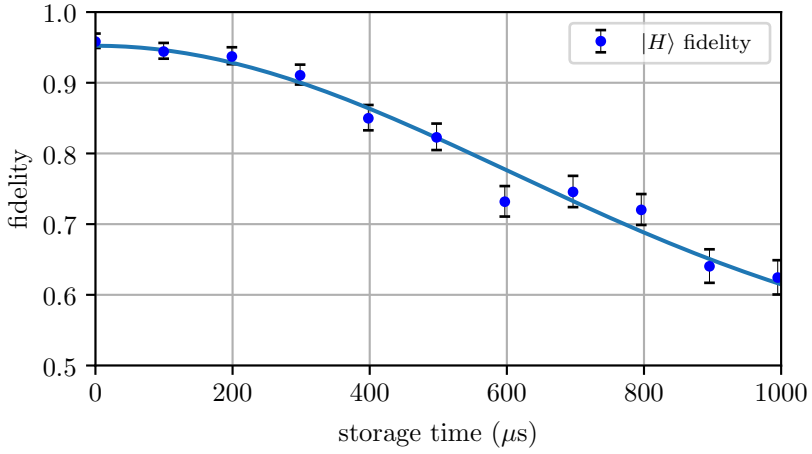

Figure 3.7.: Fidelity decay for $|H\rangle$ input state in the magnetically cleaned environment. The memory is probed with horizontally polarized input states, and the resulting fidelity is shown as a function of the storage time. The readout times are synchronized with the qubit precession to allow for fast data acquisition.

3.3.5. Conclusion

In this section, the storage of a single photon polarization qubit on a single atom has been revisited. Compared to prior work [96], a significant increase in memory efficiency was observed due to the implementation of a second intra-cavity dipole trap which increases the effective atom-cavity coupling. The fidelity for short storage durations was increased by a more precise magnetic field compensation and due to a better choice of the single-photon detuning. By reducing stray magnetic fields in the vicinity of the atom, a coherence time of almost 1 ms has been demonstrated. Further improvements in coherence time may be possible by passively shielding the atom from magnetic fields or by adding active compensation techniques, but this becomes increasingly difficult. Instead, the utilization of magnetically less sensitive atomic states to store the qubit is a promising option and is explored in the next section.

3.4. Decoherence Protected Storage

In the previous section, the storage and retrieval of a polarization qubit carried by a single photon were demonstrated with a coherence time limited by magnetic field fluctuations. To increase the coherence time of the qubit, one could employ technologies to reduce the magnetic field fluctuations, like a μ-metal shielding or a feed-forward technique to compensate the known dynamics of the field fluctuations [153]. Alternatively, the magnetic field induced decoherence can be actively prevented by mapping the qubit to a set of states with a reduced sensitivity to field fluctuations. Here, a scheme is presented in which the qubit is transferred to a decoherence-protected basis after it is successfully mapped to the atom. First, the choice of basis is motivated. Subsequently, the optical transfer to achieve the mapping is investigated and followed by the experimental realization and the results. Finally, residual decoherence effects are analyzed.

3.4.1. Decoherence Protected Atomic Qubit Basis

To reduce the dephasing of the atomic qubit, a basis with an energy splitting ΔE which is less sensitive to the magnetic field is beneficial. The sensitivity of the qubit basis is given by the magnetic field dependence of the differential Zeeman shift of the two basis states used to store the qubit. After mapping the photonic qubit onto the atom, the qubit is stored in a superposition of $\{|F{=}2,\ m_F{=}\pm1\rangle\}$. In this *interface basis*, the sensitivity of the of the energy splitting to the external magnetic field in the linear weak-field approximation is given by

$$\partial_B(\Delta E_{\text{interface basis}}) \approx \frac{3}{2} g_I \mu_B + \frac{1}{2} g_J \mu_B = 2 g_F \mu_B \tag{3.38}$$

with [144]

$$g_F = g_J \frac{F(F+1) - I(I+1) + J(J+1)}{2F(F+1)} + g_I \frac{F(F+1) + I(I+1) - J(J+1)}{2F(F+1)} \tag{3.39}$$

$$= \frac{1}{4} g_J + \frac{3}{4} g_I \qquad \text{for } {}^{87}\text{Rb in } |5^2S_{1/2}, F{=}2\rangle \tag{3.40}$$

In contrast, for a qubit mapped to a superposition of $|F{=}1,\ m_F{=}{-}1\rangle$ and $|F{=}2,\ m_F{=}1\rangle$ the sensitivity of the differential Zeeman splitting in linear approximation is given by (see Section 3.2.2)

$$\partial_B \left(\Delta E_{\text{memory basis}}\right) \approx 2 g_I \mu_B \tag{3.41}$$

For the so-called *clock state*, which is a coherent superposition of $\{|F{=}\{1,2\},\ m_F{=}0\rangle\}$, there is no linear dependence on the magnetic field and only the quadratic term contributes to the differential energy shifting

$$\partial_B^2(\Delta E_{\text{clock state}}) = (g_J - g_I)\mu_B. \tag{3.42}$$

In the weak-field regime, the magnetic field sensitivity is suppressed by the factor

$$\frac{g_F}{g_I} \approx 503.1 \tag{3.43}$$

for a qubit stored in the memory basis compared to the interface basis. Previous experiments with atom-chip traps have already confirmed, that coherence can be maintained for longer than 1 ms on this state pair [97]. With the coherence times achieved by solely storing the qubit in the interface basis, a reduction of a factor 500 should theoretically allow for a coherence time up to a few hundred milliseconds. The clock-state is even less sensitive to magnetic field fluctuations, but a mapping of the atomic qubit to this state pair poses significantly higher experimental overhead compared to the interface basis. Since the photonic qubit cannot be directly mapped onto the memory basis, the atomic qubit must be transferred between the memory basis and interface basis to allow for both light-matter interfacing and long coherence times.

Table 3.1.: Magnetic field sensitivity of different qubit basis configuration for a bias field $B_z = 44\,\mathrm{mG}$.

name	basis states $\lvert F, m_F\rangle$	sensitivity $h\Delta E/\mathrm{G}$
interface basis	$\lvert 2,-1\rangle$,$\lvert 2,+1\rangle$	1.4 MHz
memory basis	$\lvert 1,-1\rangle$,$\lvert 2,+1\rangle$	2.8 kHz
clock state	$\lvert 1,\ \ 0\rangle$,$\lvert 2,\ \ 0\rangle$	3.4Hz

3.4.2. Zeeman State Selective Population Transfer

The *memory basis*, $\{|F{=}2,\ m_F{=}1\rangle\,, |F{=}1,\ m_F{=}{-}1\rangle\,,\}$ was identified to be a suitable qubit basis to protect the qubit against magnetic field fluctuations. Although the mapping between the interface basis and the memory basis could be achieved using a microwave field to drive a quadrupole transition, an optical transfer scheme has to be utilized due to the lack of microwave power inside the cavity, caused by the shielding effect of the surrounding piezo used to stabilize the distance of the cavity mirrors.

Stimulated Raman transitions [154] are a well-known technique for coherently transferring population between two hyperfine-levels. For Raman transitions involving multiple excited states, the interaction strength of the individual transitions must be combined in the regime of large single-photon detunings and therefore effectively reduce the system to the well-known three-level model. As it has been described in [155], this results in a suppression of the transfer for the specific set of states used here, since the excitation paths mediated by the individual excited levels of both the D_1 and D_2 transition interfere destructively for large single-photon detunings. To overcome this, a single-photon detuning between the hyperfine levels must be chosen, such that the different signs of the single-photon detuning lift the destructive interference condition. However, this requires the development of a four-level model for the Raman transition in which the excited states are treated individually.

In this section, a general model to drive stimulated Raman transitions in a four-level system with small single-photon detunings is developed. Subsequently, the model is applied to the transfer used to map the qubit basis between two different configurations. Further, the requirements to transfer population only between specific Zeeman states is discussed. Finally, the scattering rates associated with the transfer are calculated and their impact on the qubit memory is estimated.

3.4.2.1. General Formalism

In this paragraph, a general formalism for a four-level Raman transition between two ground states $\{|1\rangle, |2\rangle\}$ with energy difference Δ when coupled by two light fields ω_{L1} and ω_{L2} to the excited states $\{|3\rangle, |4\rangle\}$ with energy separation Δ' (see Figure 3.8) is derived. The detunings of the driving lasers are defined with respect to the average energy of the two excited states:

$$\begin{aligned} \Delta_1 &= \omega_{L1} - \omega_{13} - \Delta'/2\ , \\ \Delta_2 &= \omega_{L2} - \omega_{23} - \Delta'/2\ . \end{aligned} \tag{3.44}$$

The single-photon detuning is defined as the average detuning of the lasers $\Delta_{12} = (\Delta_1 + \Delta_2)/2$, and the two-photon detuning as their difference $\delta = \Delta_2 - \Delta_1$. The Hamiltonian of

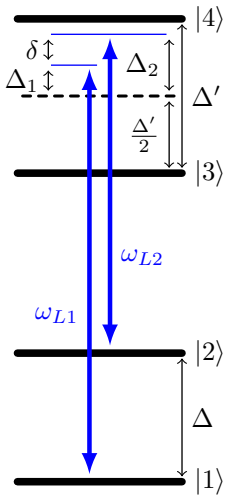

Figure 3.8.: Level scheme for the four-level raman driving. Given a four-level system with two ground states $|1\rangle$ and $|2\rangle$ with energy splitting Δ and two excited states $|3\rangle$ and $|4\rangle$ with energy splitting Δ'. The first excited state $|1\rangle$ is coupled by a field ω_{L1} to the excited states with a detuning Δ_1 which is defined with respect to the center of the excited states. Analogously, a second field ω_{L2} couples the second ground state $|2\rangle$ to the excited state with a detuning Δ_2 and the differential detuning $\delta = \Delta_2 - \Delta_1$.

the driven four-level system is given by

$$\hat{H} = \frac{\hbar}{2}\begin{bmatrix} 0 & 0 & \Omega_{13}e^{i\omega_{L1}t} & \Omega_{14}e^{i\omega_{L1}t} \\ 0 & 2\Delta & \Omega_{23}e^{i\omega_{L2}t} & \Omega_{24}e^{i\omega_{L2}t} \\ \Omega_{13}^* e^{-i\omega_{L1}t} & \Omega_{23}^* e^{-i\omega_{L2}t} & 2(\omega_{L1}-\Delta_1)-\Delta' & 0 \\ \Omega_{14}^* e^{-i\omega_{L1}t} & \Omega_{24}^* e^{-i\omega_{L2}t} & 0 & 2(\omega_{L1}-\Delta_1)+\Delta' \end{bmatrix}, \tag{3.45}$$

where $\Omega_{ij} = c_{ij}\frac{E_i d_0}{\hbar}$ are the usual atom-light interaction terms and c_{ij} is the Clebsch-Gordan coefficient for the coupling between the levels $|i\rangle$ and $|j\rangle$.

By writing the Hamiltonian in the interaction picture and by adiabatically eliminating the excited states ($|3\rangle$ and $|4\rangle$) which mediate the driving of the transition between the two ground states, the interaction Hamiltonian for the two ground states is obtained:

$$\hat{H}_\mathrm{I} = \frac{\hbar}{2}\begin{bmatrix} \frac{|\Omega_{13}|^2}{2\Delta_{12}+\Delta'} + \frac{|\Omega_{14}|^2}{2\Delta_{12}-\Delta'} - \delta & \frac{\Omega_{13}\Omega_{23}^*}{2\Delta_{12}+\Delta'} + \frac{\Omega_{14}\Omega_{24}^*}{2\Delta_{12}-\Delta'} \\ \frac{\Omega_{13}^*\Omega_{23}}{2\Delta_{12}+\Delta'} + \frac{\Omega_{14}^*\Omega_{24}}{2\Delta_{12}-\Delta'} & \frac{|\Omega_{23}|^2}{2\Delta_{12}+\Delta'} + \frac{|\Omega_{24}|^2}{2\Delta_{12}-\Delta'} + \delta \end{bmatrix}. \tag{3.46}$$

Since the diagonal elements of the Hamiltonian in the interaction picture contain the detunings of the transition with respect to the driving, one can identify the following two terms as light shifts induced by the impinged light fields:

$$\frac{|\Omega_{13}|^2}{2\Delta_{12}+\Delta'} + \frac{|\Omega_{14}|^2}{2\Delta_{12}-\Delta'} =: 2\delta_1 \ , \tag{3.47}$$

$$\frac{|\Omega_{23}|^2}{2\Delta_{12}+\Delta'} + \frac{|\Omega_{24}|^2}{2\Delta_{12}-\Delta'} =: 2\delta_2 \ . \tag{3.48}$$

With the differential light shift

$$\delta_\mathrm{ls} := \delta_2 - \delta_1 \ , \tag{3.49}$$

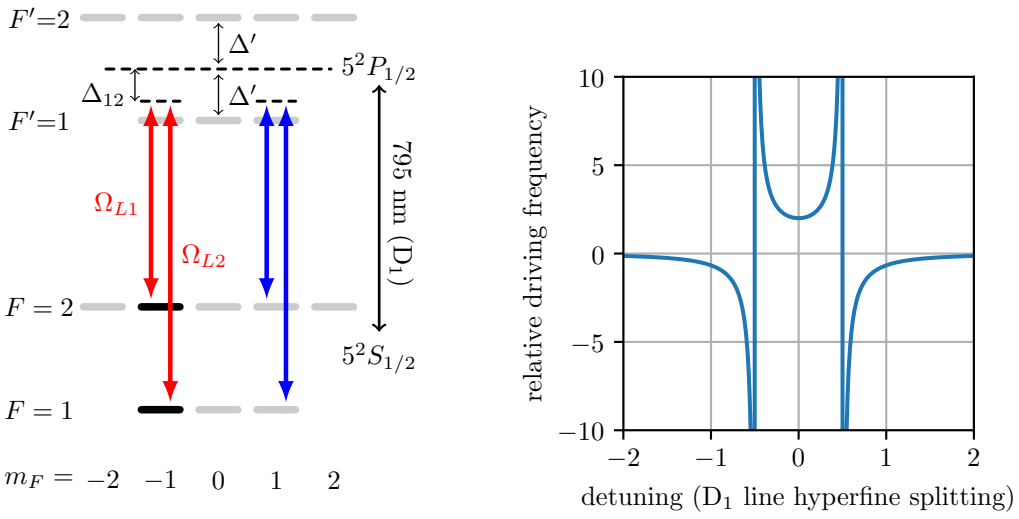

(a) **(b)**

Figure 3.9.: Four-level Raman driving applied to the transfer between the interface basis and memory basis. a) The ground states $|F{=}1, m_F{=}{-}1\rangle$ and $|F{=}2, m_F{=}{-}1\rangle$ are coupled by the π-polarized fields with Rabi frequencies Ω_{L1} and Ω_{L2} to the excited states $|F'{=}1, m_F{=}{-}1\rangle$ and $|F'{=}2, m_F{=}{-}1\rangle$ in two-photon resonance with a single-photon detuning Δ_{12} defined with respect to the center of the two excited states (red arrows). The π-polarized beams equally couple the states $|F{=}1, m_F{=}1\rangle$ and $|F{=}2, m_F{=}1\rangle$ to the excited states (blue arrows). **b)** The driving strength as a function of the single-photon detuning Δ_{12} normalized to the splitting of the two excited states.

the Hamiltonian can be identified as the usual Hamiltonian of the Rabi driving of a two-level system. For convenience, the Hamiltonian is shifted to zero energy:

$$\hat{H}_{\mathrm{I}} = \frac{\hbar}{2}\begin{bmatrix} 0 & \Omega \\ \Omega^* & 2(\delta - \delta_{\mathrm{ls}}) \end{bmatrix} . \tag{3.50}$$

Hence, the generalized Rabi frequency is given by

$$\Omega_R = \sqrt{\Omega^2 + (\delta - \delta_{\mathrm{ls}})^2} , \tag{3.51}$$

with the transfer amplitude

$$T = \Omega^2/\Omega_R^2.$$

As for a two-level system, the transfer amplitude is unity for a vanishing effective detuning. Hence, to achieve full transfer, the two-photon detuning must compensate for the induced light shift.

3.4.2.2. Mapping Between the Interface and Memory Basis

To map the qubit to the memory basis, the atomic population of the $|F{=}2, m_F{=}{-}1\rangle$ state must be transferred to the $|F{=}1, m_F{=}{-}1\rangle$ state. To address this $\Delta m_F = 0$ transition, two π-polarised beams (i.e. linearly polarized along the quantization axis) with $\vec{E}_i = E_i \cos(\omega_{Li} + \phi_i))\vec{\epsilon}_y$ are used. To apply the formula derived for the four-level transfer, the states are identified as follows

$$|1\rangle = |F = 1, m_F = -1\rangle , \qquad |2\rangle = |F = 2, m_F = -1\rangle , \tag{3.52}$$

$$|3\rangle = |F' = 1, m_F = -1\rangle , \qquad |4\rangle = |F' = 2, m_F = -1\rangle . \tag{3.53}$$

With the corresponding Clebsch-Gordan coefficients, the driving terms are given by:

$$\Omega_{13} = \frac{1}{\sqrt{12}} \frac{E_1 d_0}{\hbar} e^{i\phi_1}, \qquad \Omega_{14} = \frac{1}{\sqrt{4}} \frac{E_1 d_0}{\hbar} e^{i\phi_1} \ , \tag{3.54}$$

$$\Omega_{23} = \frac{1}{\sqrt{4}} \frac{E_2 d_0}{\hbar} e^{i\phi_2}, \qquad \Omega_{24} = \frac{-1}{\sqrt{12}} \frac{E_2 d_0}{\hbar} e^{i\phi_2} \ , \tag{3.55}$$

where E_i is the real amplitude of the electric field of the impinging light field i and d_0 the dipole moment of the transition.The total driving term (see Section 3.50) identified in the previous section becomes

$$\begin{aligned} \Omega_{\parallel} &= \frac{\Omega_{13}\Omega_{23}^*}{2\Delta_{12} + \Delta'} + \frac{\Omega_{14}\Omega_{24}^*}{2\Delta_{12} - \Delta'} \\ &= \frac{e^{i(\phi_1 - \phi_2)}}{\sqrt{4 \cdot 12}} \frac{E_1 E_2 d_0^2}{\hbar^2} \left(\frac{1}{2\Delta_{12} + \Delta'} - \frac{1}{2\Delta_{12} - \Delta'} \right) \ . \end{aligned} \tag{3.56}$$

Note that the Clebsch-Gordan coefficients lead to the same amplitude of Raman driving for both excited states but with a detuning-dependent factor. This can be seen as an interference of the two Raman processes. For $\Delta_{12} \gg \Delta'$ both processes interfere destructively. In contrast, for $\Delta_{12} < \frac{1}{2}\Delta'$ the two processes interfere constructively, with the maximum transfer frequency for $\Delta_{12} = 0$. As already discussed by Uphoff [155], this shows that this transfer cannot be efficiently realized using π-polarised light fields and a large single-photon detuning which necessarily has the same sign for both excited levels. When discussing scattering rates during this transfer (see Section 3.4.2.4) this restriction becomes important.

3.4.2.3. Zeeman State Selectivity

To map the qubit between the memory basis and the interface basis only the population in $|F{=}2,\, m_F{=}{-1}\rangle$ has to be transferred to $|F{=}1,\, m_F{=}{-1}\rangle$ (see red arrow in Figure 3.10), while the population in $|F{=}2,\, m_F{=}1\rangle$ should remain in its initial state and should not be transferred down to $|F{=}1,\, m_F{=}1\rangle$ (blue arrow in Figure 3.10). To allow the transfer to be Zeeman state selective, a bias magnetic field along the quantization axis has to be applied. The bias field introduces a component to the two-photon detuning of two Larmor quanta which acts in the opposite direction for both transitions:

$$\Delta\omega_{\text{trans.}} = \pm 2\delta_L = \pm \frac{2\mu_B g_F B_{\text{bias}}}{\hbar} \ . \tag{3.57}$$

The Hamiltonian for the four-level Raman transfers for the two individual transitions is given by

$$\hat{H} = \frac{\hbar}{2} \begin{bmatrix} \begin{bmatrix} -2\delta_L & \Omega \\ \Omega^* & 2(\delta_{ls} + \delta + \delta_L) \end{bmatrix} & 0 \\ 0 & \begin{bmatrix} 2\delta_L & \Omega \\ \Omega^* & 2(\delta_{ls} + \delta - \delta_L) \end{bmatrix} \end{bmatrix} , \tag{3.58}$$

in the basis $\{|F{=}1,\, m_F{=}{-1}\rangle, |F{=}2,\, m_F{=}{-1}\rangle, |F{=}1,\, m_F{=}{+1}\rangle, |F{=}2,\, m_F{=}{+1}\rangle\}$ with the two-photon detuning of $\pm 2\delta_L$ introduced to the subsystems. To achieve full population transfer between $|F{=}2,\, m_F{=}{-1}\rangle$ and $|F{=}1,\, m_F{=}{-1}\rangle$ the detuning has to compensate for the light shift and the two Larmor quanta:

$$\delta = -(\delta_{ls} + 2\delta_L) \tag{3.59}$$

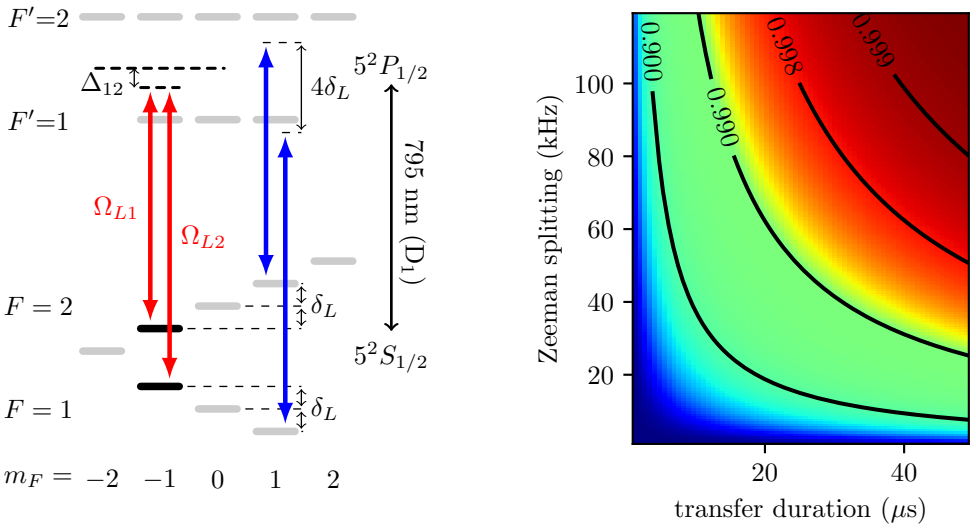

(a) **(b)**

Figure 3.10.: Four-level Raman driving applied to the transfer between the interface basis and memory basis with bias magnetic field. a) The ground states $|F{=}1, m_F{=}{-}1\rangle$ and $|F{=}2, m_F{=}{-}1\rangle$ are coupled by the π-polarized fields with Rabi frequencies Ω_{L1} and Ω_{L2} to the excited states $|F'{=}1, m_F{=}{-}1\rangle$ and $|F'{=}2, m_F{=}{-}1\rangle$ in two-photon resonance with the single-photon detuning Δ_{12} defined with respect to the center of the two excited states (red arrows). A bias magnetic field induces a Zeeman splitting δ_L which shifts the $|F{=}1, m_F{=}1\rangle$ and $|F{=}2, m_F{=}1\rangle$ which are also coupled by the π-polarized beams $4\delta_L$ out of the two-photon resonance condition (blue arrows). **b)** Suppression of the driving of the wrong transitions (blue arrows) as a function of the Zeeman splitting and the transfer duration.

This will lead to an effective two-photon detuning of $4\delta_L$ for the transition between $|F{=}2, m_F{=}1\rangle$ and $|F{=}1, m_F{=}1\rangle$ as it is illustrated in Figure 3.10a. The transfer amplitude T_- of the wrong transition is given by

$$T_- = \frac{|\Omega|^2}{|\Omega|^2 + 16\delta_L^2}. \tag{3.60}$$

Driving Amplitude Suppression Approach

To achieve a suppression of at least S for the unwanted transfer, the Zeeman splitting δ_L must be chosen sufficiently large such that the driving amplitude T_- gets below the threshold given by S. This yields the following inequality condition:

$$\delta_L \geq \frac{\Omega\sqrt{S}}{4\sqrt{(1-S)}} = \frac{\pi\sqrt{S}}{4t_\pi\sqrt{(1-S)}}\,, \tag{3.61}$$

with the time t_π for a π-transfer. The transfer duration t_π is critical since the qubit has to be transferred to the decoherence-protected basis as fast as possible to avoid dephasing. For a transfer duration of 40 μs and a suppression of $S{=}0.99$, a Zeeman splitting of at least $\delta_L{\approx}2\pi{\cdot}31$ kHz is needed (see Figure 3.10b).

Double Transfer Approach

An alternative approach is to drive a 2π transfer on the unwanted transition while a π-transfer is driven on the target transition. For a vanishing two-photon detuning on the tar-

get transfer and a constant driving frequency, the following condition must be fulfilled:

$$2n{\cdot}\Omega = \sqrt{\Omega^2 + 16\delta_L^2} \quad \forall\, n \in \mathbb{N}^+ \tag{3.62}$$

Here, the Rabi frequency and the Zeeman splitting have to be in tune with each other. Obviously, this is experimentally more challenging than full-filling the inequality condition (see Equation 3.61), but in principle, perfect suppression can be achieved with a finite Zeeman splitting δ_L. Additionally, for a given Zeeman splitting δ_L the transfer can be performed faster compared to the approach discussed above. However, for the experimental realization, the suppression of the transfer amplitude is the preferred method since the detuning is more robust and the Zeeman splitting can be chosen sufficiently large for the demands on the transfer duration.

3.4.2.4. Scattering Rates

Although the Raman transfer discussed so far is a coherent process it is associated with a probability to incoherently scatter a photon. Such a scattering event can affect both the T_1 and the T_2 time of the stored, qubit since it can destroy the coherence between the storage states and can also lead to a change of the population amplitudes resulting in a classical bit flip (see Section 3.2.1.4). In most experimental scenarios, the scattering rates associated with Raman transfers can be suppressed straight-forwardly by using a large single-photon detuning. However, as discussed in Section 3.4.2.4 this specific transfer is suppressed for large single-photon detunings due to the destructive interference of two competing transfer mediated by the individual hyperfine levels of the D_1 line. Therefore, a single-photon detuning must be chosen which allows for a sufficiently fast transfer with a reasonable intensity of the Raman pair while simultaneously resulting in a low scattering rate to avoid decoherence induced by the transfer. To this end, the scattering probability as a function of the single-photon detuning is characterized to define the optimal working point.

In a first step, it is determined, that the scattering probability for a π-pulse in a two-photon transition is constant and independent of the Rabi frequency if both Raman beams have the same intensity up to a constant factor. Subsequently, the scattering probability for the transfer discussed in this section is evaluated as a function of the single-photon detuning, and the optimal working point is identified. Finally, the impact of a scattering event on the qubit coherence is approximated.

Independence on Rabi frequency and pulse shape

The scattering rate for an off-resonant light-field is given by [144]

$$\Gamma_{sc} = \frac{3\pi c^2}{2\hbar\omega_0^3}\frac{\Gamma^2}{\Delta^2} I \ , \qquad I = \frac{1}{2}\epsilon_0 c E^2. \tag{3.63}$$

The Rabi frequency for a two-photon Raman transition is proportional to the product of the electric fields associated with the Raman beams:

$$\Omega(t) \propto \frac{E_1 E_2}{\Delta} \approx \frac{E^2}{\Delta} \quad \text{for} \quad E = E_1 = c\ E_2 \tag{3.64}$$

Here, it is assumed that both beams have equal light intensities and therefore the same electric field amplitudes. For any given detuning Δ, the probability to scatter $p(\Delta)_{\text{scat}}$ during a π transition is proportional to the pulse area,

$$p(\Delta)_{\text{scat}} = \int \Gamma(\Delta)_{\text{scat}}\, dt \propto \int E(\Delta)^2\, dt \propto \int \Omega(\Delta)\, dt = \pi, \tag{3.65}$$

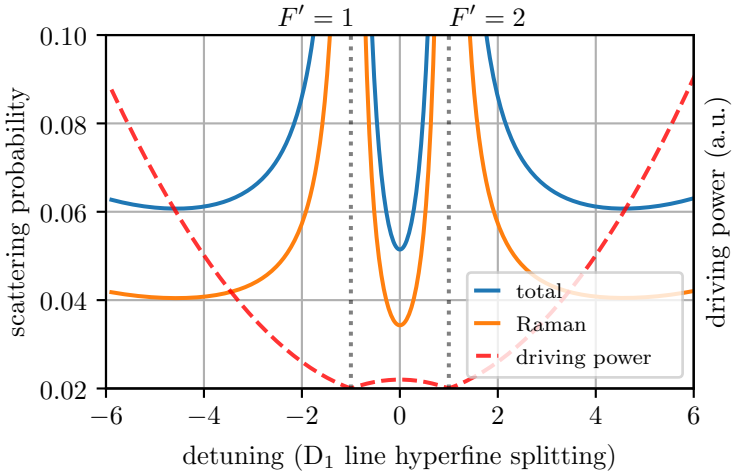

Figure 3.11.: Scattering probability over detuning. Here, the overall scattering probability associated with a π-pulse is shown as a function of the single-photon detuning. The single-photon detuning is normalized to the hyperfine-splitting of the D_1 line. The 0 corresponds to the center of the two hyperfine levels. The dashed grey lines mark the spectral position of the $|F'{=}1\rangle$ and $|F'{=}2\rangle$ energy levels. The solid orange lines show the expected Raman scattering probability, and the blue line shows the total expected scattering probability incorporating both Raman and the Rayleigh scattering. The dashed red lines show the scaling of the needed beam intensity to drive the π-transition in constant time.

but independent on the details of the shape. Note that this independence relies on the proportionality of the electric field strengths, $E_1 \propto E_2$. Consequently, the scattering probability p_{scat} is only a function of the single-photon detuning Δ.

Scattering Probability vs Detuning

Applied to the four-level transfer, the total scattering probability is evaluated according to [156]. The dynamics of the driving process can be eliminated by utilizing the fact that the integrated atomic population is equally distributed between the initial state $|F{=}2, m_F{=}{-}1\rangle$ and the target state $|F{=}1, m_F{=}{-}1\rangle$. The scattering probabilities associated with the individual states are determined by summing over all possible excitations paths. By evaluating the possible decay channels, one must distinguish Raman and Rayleigh scattering. In principle, only the Raman scattering events are affecting the coherence of the driving because Rayleigh scattering does not destroy the coherence between the basis states [156]. Moreover, the scattering process is fast compared to the driving duration. The scattering probabilities are shown in Figure 3.11 as a function of the detuning. The scattering probability is minimized precisely in between the two hyperfine levels of the $5^2P_{1/2}$ state. Although the driving power is maximized in between the two $|F'{=}1\rangle$ and $|F'{=}2\rangle$ states, the constructive interference of the two competing driving processes (see Section 3.4.2.1) allows for the simultaneous minimization of the scattering probability and sets the optimal working point with a scattering probability of $p_{\text{scat}}{=}3.4\%$ (5.1% if Rayleigh scattering is not excluded).

Impact on the Qubit Fidelity

Here, a simple approximative model is derived to estimate the impact of the scattering on the qubits fidelity. There are two general cases to be taken into account: first, for successful storage events which happen with a probability p_{store}, the population can be

scattered to a random state during the transfer. It is approximatively assumed that after an incoherent decay, the system has a 2/3 probability to produce a random photon once read-out, or alternatively no photon, because the final state after the decay lies within the $|F{=}1\rangle$ manifold and is not addressed by the read-out process. Second, for unsuccessful storage attempts the atomic population is scattered to a state which produces an incoherent photon during the readout with a probability of 2/3. The approximated degradation of the fidelity $\Delta\mathcal{F}$ is given by

$$\Delta\mathcal{F} = \mathcal{F}_0 - \frac{\mathcal{F}_0 \cdot p_{\text{store}}(1-p_{\text{scat}}) + \frac{1}{3}p_{\text{scat}}}{p_{\text{store}}(1-p_{\text{scat}}) + \frac{2}{3}p_{\text{scat}}} \tag{3.66}$$

where $\mathcal{F}_0$ is the qubit fidelity for short storage times. For a write efficiency $p_{\text{store}}{\approx}0.22$ (see Section 2.6) the degradation is $\Delta\mathcal{F}{\approx}0.027$ (0.040 if Rayleigh scattering is not excluded). Note that this transfer has to be performed twice to make the qubit available for readout, resulting in a total fidelity degradation of $\Delta\mathcal{F}_{\text{total}}{\approx}0.052$ (0.076 including Rayleigh scattering). This yields the approximated higher bound for the qubit fidelity achievable with this transfer used in this specific configuration.

3.4.2.5. Conclusion

In this section, a general formalism for a four-level Raman transfer was derived and applied for the transfer between $|F{=}2,\, m_F{=}{-}1\rangle$ and $|F{=}1,\, m_F{=}{-}1\rangle$ mediated by the $5^2P_{1/2}$ state. The transfer was shown to be most efficient for a single-photon detuning between the two hyperfine levels of the $5^2P_{1/2}$ state due to an interference effect which becomes destructive for large single-photon detunings. The Zeeman state selectivity is provided by applying a bias magnetic field in the direction of the cavity axis which shifts the undesired transfer affecting the population of the other qubit basis state out of resonance. By the choice of a single-photon detuning at the center of the two hyperfine transitions of the D_1 line, the scattering probability associated with the transfer is minimized.

3.4.2.6. Experimental Realization

In the previous sections, a decoherence-protected storage basis was identified and a four-level Raman transfer scheme to coherently map the qubit between the interface and the storage basis was derived. In this section, the experimental realization of a storage protocol utilizing the decoherence protected qubit basis is described. Note that the protocol is a superset of the single-atom quantum memory (see Section 3.3). Here, only the details concerning the mapping to the decoherence protected basis are discussed.

To perform the optical four-level Raman transfer a pair of co-propagating phase-stable laser beams has to be generated which has a spectral distance corresponding to the energy splitting $\Delta E \approx h\,6.8\,\text{GHz}$. Further, additional spectral components have to be suppressed to avoid the generation of light-shifts which disturb the two-photon resonance and imprint additional phase offsets. To drive reliable π-transitions, the intensity of the Raman pair has to be actively stabilized to compensate thermal and mechanical drifts.

3.4.2.7. Sideband Generation with a Mach-Zehnder Interferometer

The creation of sidebands in a periodically driven Mach-Zehnder interferometer is a well-known and widely used technique. Here, the working principle is briefly explained and the

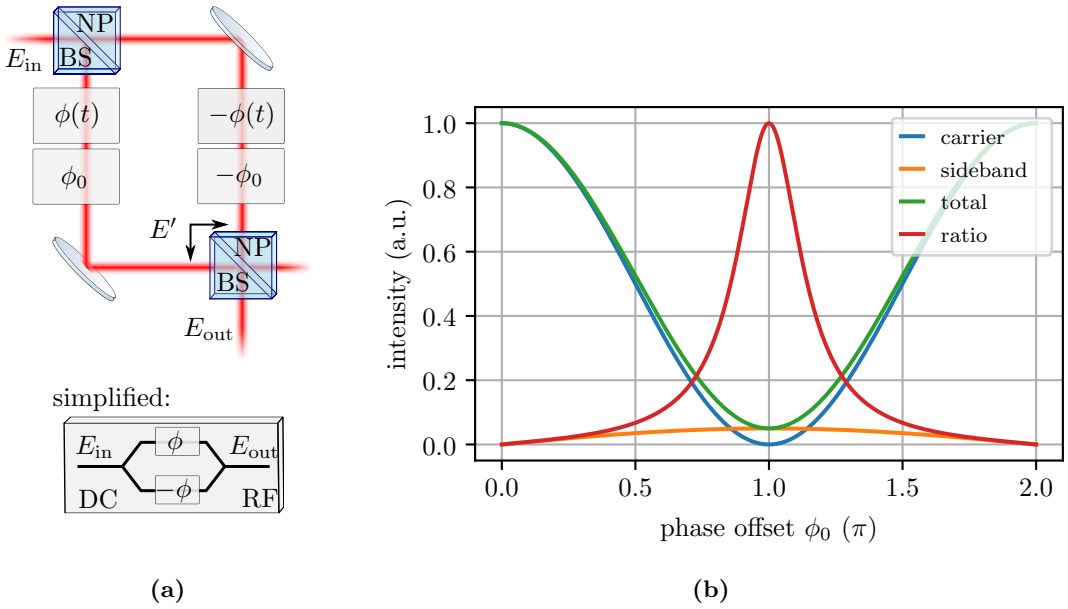

(a) **(b)**

Figure 3.12.: a) Schematics of a Mach-Zehnder interferometer. The light is split into the two arms of the interferometer, and an antisymmetric phase shift is applied. The phase shift consists of a time-dependent part $\phi(t)$ and a constant offset ϕ_0 which can be controlled individually. Afterward, the two arms are recombined and one port serves as the output of the interferometer. **b) Light-intensity of the carrier and the sidebands as a function of the phase offset.** The blue line shows the normalized intensity of the carrier transmitted through the interferometer, while the orange line represents the total intensity of the created sidebands. The ratio of the former is shown by the red line and the green line corresponds to the total light intensity transmitted. It can be seen that a phase offset $\phi_0 = \pi/2$ completely suppresses the transmission of the carrier frequency while simultaneously minimizing the total transmission and maximizing the intensity of the sidebands.

expression for a periodically driven Mach-Zehnder interferometer is later used to demonstrate the suppression of the carrier by minimizing the total intensity of the resulting light-field.

In a Mach-Zehnder interferometer, a beamsplitter divides the impinging light field

$$E_{\text{in}} = e^{-i\omega t} E_0 \tag{3.67}$$

into the two arms of the interferometer. In the so-called *push-pull* configuration, an antisymmetric phase boost $\pm\phi = \pm(\phi(t)+\phi_0)$ with a time-dependent and a constant component is applied to the light fields in each arm. The field inside the interferometer is given by

$$E' = \frac{E_0}{\sqrt{2}} \left(e^{-i\omega t+\phi_0+\phi(t)} - e^{-i\omega t-\phi_0-\phi(t)} \right). \tag{3.68}$$

Subsequently, the light is recombined at a second beamsplitter (see Figure 3.12a) where both beams interfere at the individual ports of the beamsplitter. The energy distribution between both ports is a function of the phase boost applied inside the interferometer:

$$E_{\text{out}} = \frac{E_0}{2} \left(e^{-i\omega t+\phi_0+\phi(t)} + e^{-i\omega t-\phi_0-\phi(t)} \right) \tag{3.69}$$

$$= E_0 e^{-i\omega t} \left(\cos\left(\phi_0 + \phi(t)\right) \right) \tag{3.70}$$

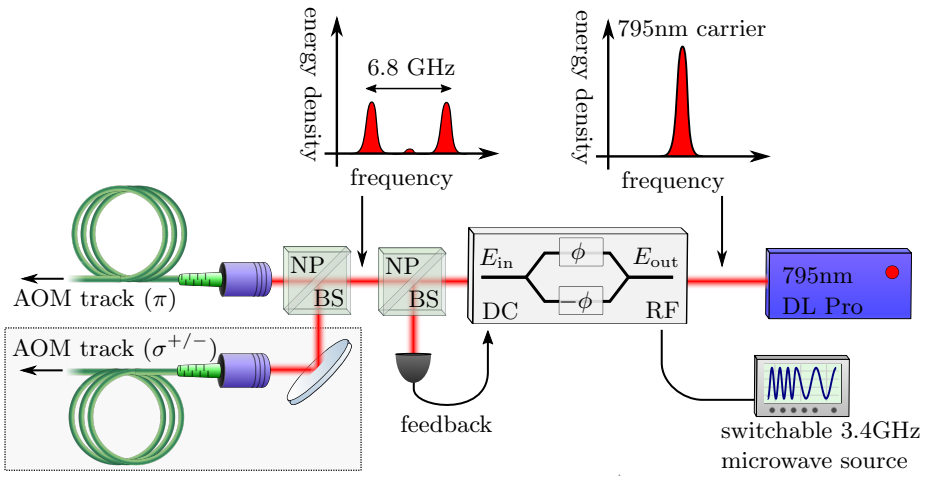

Figure 3.13.: Raman sideband generation. Laser light with a wavelength of 795 nm emitted from a diode laser is fed into a fiber-coupled phase modulator. A microwave generator with a frequency of roughly 3.4 GHz drives the modulator, resulting in a sideband separation of twice the driving frequency. The microwave source can be phase-coherently switched between two frequencies. This allows for rapidly switching between two sideband separations without introducing random phase offsets. The optical power at the output port of the modulator is measured and the DC input of the modulator is adjusted to minimize the total output power in order to suppress the transmission of the carrier frequency. The resulting co-propagating Raman pair is first split and then coupled into two polarization-maintaining optical fibers for subsequent usage. The second fiber in the grey box becomes important in a later chapter.

With the given phase shift controlled by an external source voltage $U = U(t) + U_{\text{DC}}$

$$\phi(t) = \alpha \cos(\delta t) \qquad \text{with} \quad \alpha = \frac{U(t)\pi}{U_0} \ll 1 \quad \text{and} \quad \phi_0 = \frac{\pi U_{\text{DC}}}{U_\pi} \tag{3.71}$$

the recombined field at one port of the beamsplitter becomes (A.4 for derivation)

$$E_{\text{out}} \approx \underbrace{E_0 \cos(\phi_0) e^{-i\omega t}}_{\text{carrier}} - \underbrace{E_0 \frac{\sin(\phi_0)}{2} e^{-i(\omega \pm \delta)t}}_{\text{symmetric sidebands}} . \tag{3.72}$$

As it can be seen from Equation 3.72, the weak sinusoidal modulation applied to the phase boost inside the interferometer results in the creation of two symmetric sidebands spectrally spaced from the carrier by the modulation frequency $\pm\delta$. This yields the recipe to create the Raman pair: by driving the Mach-Zehnder interferometer with half the frequency corresponding to the target transition two phase coherent sidebands emerge with the correct frequency splitting.

Note that the driving frequency must be switched coherently between the two-photon resonance frequency during the actual transfer, and the slightly different energy splitting of the qubit basis to compensate for qubit rotation in the rotating frame of the Raman pair. This is achieved by the *Frequency Shift Keying* feature of the Rohde und Schwarz SMF 100A microwave generator.

3.4.2.8. Carrier Suppression

The presence of the carrier poses two problems: first, it induces a light shift of the atomic transitions which must be compensated to maintain the two-photon resonance condition.

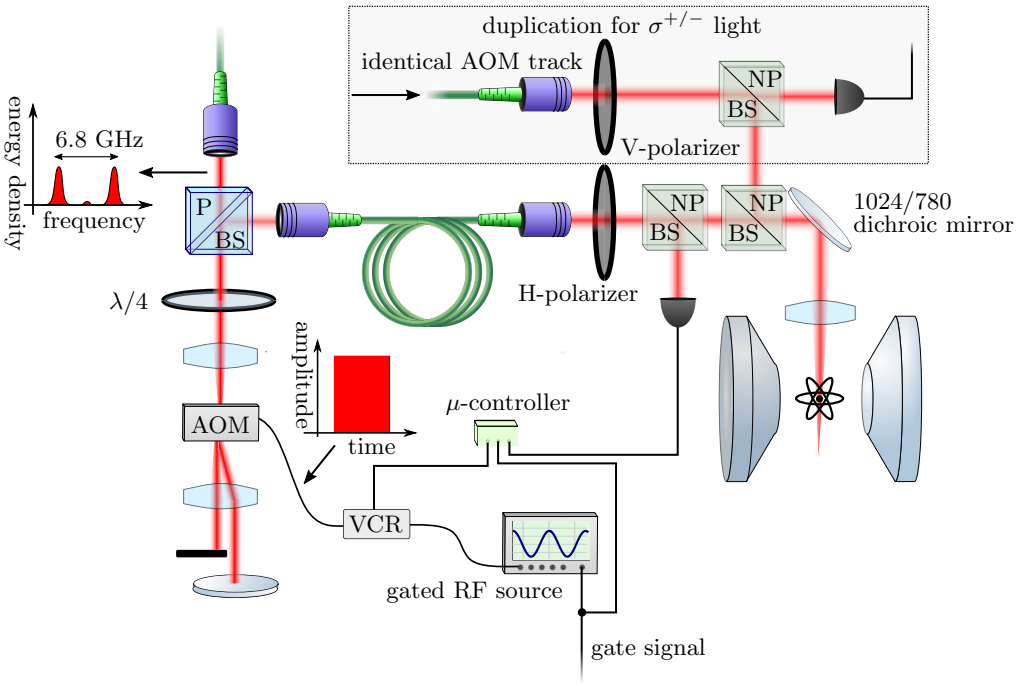

Figure 3.14.: Raman pair power stabilization. The carrier-free Raman pair is switched using an acousto-optical modular (AOM) to generate an approximatively 40 μs long rectangular shaped pulse. The AOM is driven by a gated radio-frequency source with a voltage controlled attenuator (VCA) in between to adjust the amplitude of the driving signal. The switched light is coupled into an optical fiber and guided towards the cavity system where it is first filtered by a horizontal polarizer. Afterward, the light is split by a non-polarizing beamsplitter and the output of one port of the beamsplitter is first combined with the 1064 nm dipole trap beam and focussed onto the atom. A microcontroller is triggered by the same gate signal which activates the radio-frequency source and measures the voltage signal from a photodiode corresponding to the light intensity behind the second port of the beamsplitter. The microcontroller then applies a feedback signal to VCA to compensate upstream drifts affecting the intensity of the Raman pair. A second identical setup used for $\sigma^{+/-}$- instead of π-polarized light with an independent power stabilization is indicated by the grey box and becomes important in a later section.

Second, the basis transfer relies on π-transfers, and therefore, on stable beam intensities. Although the total power can be stabilized downstream, it is crucial to have a constant ratio of the amount of intensity in the sidebands to the total energy. As it can be seen in 3.72, this is a function of the constant phase term ϕ_0 which can drift over time e.g. due to temperature fluctuations. The total intensity of the output light as a function of ϕ_0 is given by

$$I(\phi_0) = E_0 \left(\cos(\phi_0)^2 + \frac{1}{2} \sin(\phi_0)^2 \alpha^2 \right) . \tag{3.73}$$

For $\phi_0 = n\pi \ \forall n \in \mathbb{N}$ the carrier is completely suppressed and the overall intensity is minimized as it is illustrated in Figure 3.12b. Consequently, the intensity of the output field is used to create a feedback loop with the DC-input of the interferometer, which controls the constant phase offset, to minimize the output intensity (see Figure 3.13).

3.4.2.9. π-Pulse Generation and Power Stabilization

For the basis transfer used to map the qubit to the magnetic-field insensitive atomic-state pair, it is crucial to drive reproducible π-transitions within a short period of time. To this

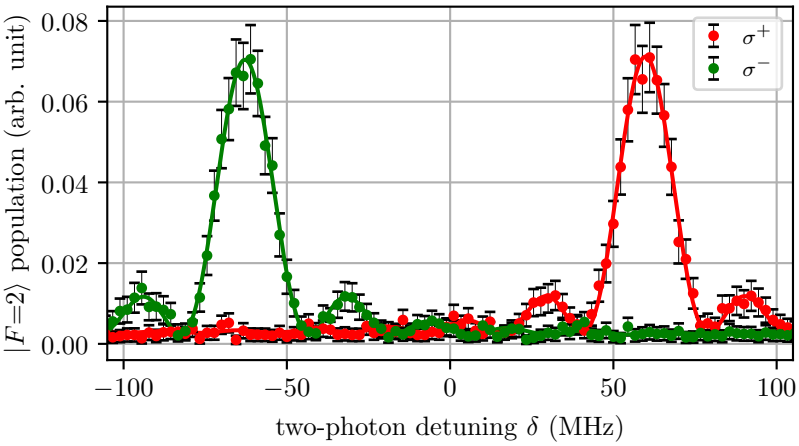

Figure 3.15.: Zeeman state selectivity. The atomic population is prepared in the $|5^2S_{1/2}, F{=}1\rangle$ state and randomly distributed over the Zeeman substates. The Raman transfer is applied with a variable two-photon detuning for a duration corresponding roughly to a 3/2 π-pulse. Subsequently, the photon production protocol is applied and the photon is detected polarization resolved in the $|H\rangle, |V\rangle$ basis. Besides the spectral information, the polarization yields additional information about the atomic state from which the photon was produced. The two peaks correspond to the transfer $|F{=}1, m_F{=}{-}1\rangle \rightarrow |F{=}2, m_F{=}{-}1\rangle$ and $|F{=}1, m_F{=}1\rangle \rightarrow |F{=}2, m_F{=}1\rangle$.

end, a rectangular pulse with an extent of 40 μs is created by means of an acousto-optical modulator (AOM) and coupled to a polarization maintaining optical fiber. The 10 m long fiber guides the light towards the cavity system where the out-coupled light is first filtered by a polarizer and afterward split by a non-polarizing beamsplitter. The output of one port of the beamsplitter is projected onto the atom while the second output measures the intensity of the pulse. By using this latest possible point for the intensity measurement, all upstream drifts including the AOM coupling efficiency, the coupling to the optical fiber as well as rotations of the polarization are detected and only drifts of the apparently very stable beam-pointing are untreated. To stabilize the pulse power projected onto the atom, the measured intensity is used as a feedback signal to adjust the driving amplitude of the AOM by means of a voltage controlled attenuator.

The challenging aspect is that the Raman beam is a short pulse controlled by a gate signal which activates the RF source which drives the AOM. Therefore, the power stabilization must measure the intensity of a short pulse at a given moment. To this end, a circuit board with an ADUC-7020 microcontroller is triggered by the gate pulse which activates the RF source. After a delay of 5 μs the microcontroller reads the output signal of the Thorlabs PDA-36 photodiode used to measure the Raman beams intensity and feeds back a voltage signal to a voltage controlled attenuator to adjust the driving amplitude of the AOM (see Figure 3.14).

3.4.3. Experimental Results

3.4.3.1. Basis Transfer Zeeman State Selectivity

The Zeeman state selectivity is a crucial requirement for the decoherence-protected storage (see Section 3.4.2.3) because the transfer to the decoherence-protected memory basis relies on solely coupling the $|F{=}2, m_F{=}{-}1\rangle \leftrightarrow |F{=}1, m_F{=}{-}1\rangle$ transition while maintaining the population in the $|F{=}2, m_F{=}1\rangle$ state. To experimentally investigate the selectivity,

the atom is initialized in the $|5^2S_{1/2}, F{=}1\rangle$ manifold employing optical hyperfine pumping [118] with an almost randomly distributed Zeeman state. Subsequently, the Raman pair is impinged with a variable two-photon detuning δ to probe the driving of the different m_F states up to the $|5^2S_{1/2}, F{=}2\rangle$ manifold (see Figure 3.10a). The area of the rectangular shaped Raman pulse is set to approximatively 0.6π by driving the optical transition for $25\,\mu$s. Finally, the population of the $|F{=}2\rangle$ manifold is probed by applying the photon emission protocol, with the subsequent detection of the potentially created photon with the polarization resolving single-photon detection setup in the R/L (σ^+/σ^-) basis configuration. Note that the two possible transitions which can be driven in this configuration can either result in a σ^+ polarized photon or a σ^- polarized photon, respectively.

The photon emission efficiency as a function of the two-photon detuning δ is shown in Figure 3.15. The two driven Raman transitions $|F{=}1, m_F{=}{-}1\rangle \leftrightarrow |F{=}2, m_F{=}{-}1\rangle$ and $|F{=}1, m_F{=}1\rangle \leftrightarrow |F{=}2, m_F{=}1\rangle$ are spectrally well resolved, and the produced photons corresponding to the individual transitions exhibit the expected polarizations. The maxima of the two polarization channels are spaced by (122.68 ± 0.15) kHz which corresponds to a Zeeman splitting of $\delta_L = (30.67 \pm 0.04)\,$kHz.

By fitting each polarization channel to a Lorentzian and by subsequently comparing the values of both curves at the peak position corresponding to the $|F{=}2, m_F{=}{-}1\rangle \leftrightarrow |F{=}1, m_F{=}{-}1\rangle$ transition, after the subtraction of the base level, one can determine the suppression ratio $S{\approx}99.0{\pm}0.2$ between the driving of the targeted transition and the unwanted transition which is in good agreement with the theoretical expectation (see Section 3.4.2.3). The comparability of the extracted value with the theoretical expectation is limited since the pulse area is not π, and a fair distribution between the m_F states in the initialization process is not ensured.

In conclusion, the data is in good agreement with the theoretical expectation and demonstrates a good Zeeman state selectivity of the transfer.

3.4.3.2. Coherence of the Basis Transfer

Besides the Zeeman state selectivity, the coherence of the transfer and the exact duration to perform a π-transfer is critical. To map the qubit back and forth between the two bases, a complete Rabi cycle must be coherently driven in two steps. The coherence of the driving is probed for the $|F{=}1, m_F{=}{-}1\rangle \leftrightarrow |F{=}2, m_F{=}{-}1\rangle$ transition by initializing the qubit in $|F{=}1\rangle$ with a randomly distributed Zeeman state and subsequently driving the transition for a variable duration. Subsequently, the population of $|F{=}2\rangle$ is probed. In contrast to the previous experiment (see 3.4.3.1) the cavity is locked onto the $|F{=}2\rangle \leftrightarrow |F{=}3\rangle$ transition to allow the application of the cavity-assisted hyperfine state detection protocol [152] to trade the Zeeman substate resolved detection against higher data rates.

The population of the $|F{=}2\rangle$ manifold as a function of the driving duration is shown in Figure 3.16 and the data is fitted to an exponentially damped oscillation. From this curve a driving duration of $(46.1{\pm}0.2)\,\mu$s for a π-transition is determined. Further, the curve has an exponential time constant of $(571{\pm}206)\,$ms. This corresponds to 6.1 Rabi cycles with a length of $T_{BT} \approx 92.30$ and a 7.9% loss of oscillation contrast for one π-cycle. This result is compatible with the theoretically determined Raman scattering probability of 3.2% per π-cycle. Note that the population of not only the $|F{=}1, 2, m_F{=}{-}1\rangle$ states can be scattered. Also, the branching ratios must be taken into account to model the damping of the

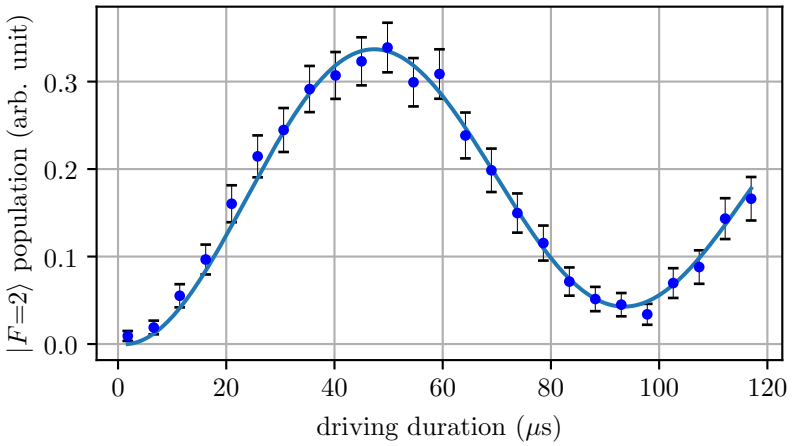

Figure 3.16.: Population transfer over storage time. The atomic state is initialized to $\left|5^2S_{1/2}, F{=}1\right\rangle$ and the Raman transfer is applied for a variable duration. Subsequently, the population of the $\left|5^2S_{1/2}, F{=}2\right\rangle$ is detected utilizing a cavity-assisted hyperfine state detection [152]. For a given Raman-pair beam-intensity the duration of a π-pulse can be extracted. Note, that only the population in the $|F{=}1, m_F{=}{-}1\rangle$ state is transferred and the exact distribution of the population between in substates is unknown. Consequently, the units of the population transfer is arbitrary.

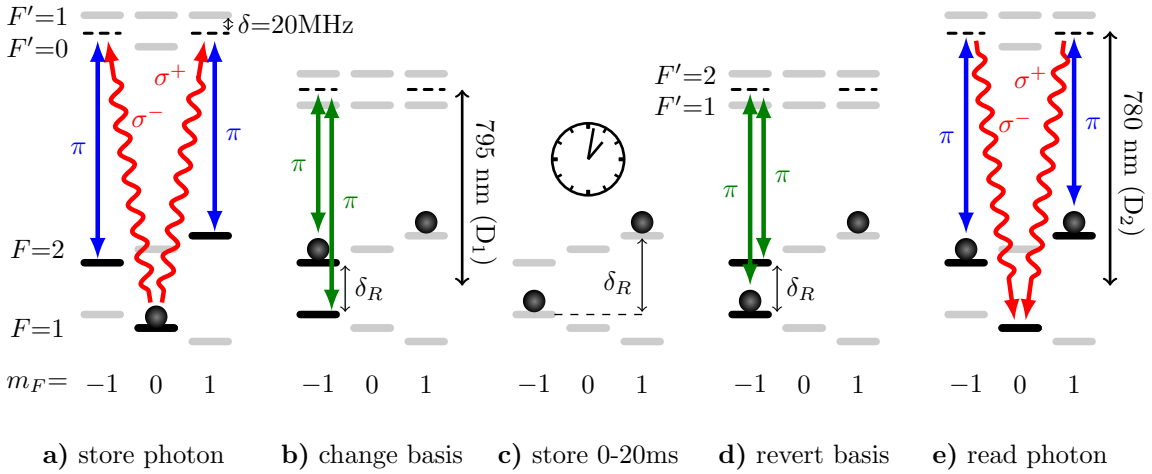

Figure 3.17.: Protocol for the photonic polarization qubit storage on a single ^{87}Rb atom. a) After the atom is initialized in the $|F{=}1, m_F{=}0\rangle$ ground state the photonic polarization qubit is mapped onto the basis states $|F{=}2, m_F{=}{-}1\rangle$ and $|F{=}2, m_F{=}1\rangle$. **b)** Immediately after the absorption process, the population in the $|F{=}2, m_F{=}{-}1\rangle$ state is transferred to the $|F{=}1, m_F{=}{-}1\rangle$ state utilizing the Raman pair with a frequency splitting δ_R corresponding to the transition frequency. **c)** During the storage time, the frequency splitting of the Raman pair δ_R is adjusted to the corresponding energy difference of the new qubit basis to eliminate the qubit precession. **d)** Before the read-out, the Raman pair is set again to the transition frequency such that the basis change can be reverted. **e)** Finally, the qubit is retrieved by photon emission protocol.

oscillation contrast accurately. However, with this measurement, the duration for a π-pulse is determined which is a prerequisite for the storage experiment in the next section.

3.4.3.3. Qubit Coherence

In this section, the basis transfer which was characterized in the previous sections is applied to the photonic qubit storage protocol to protect the coherence of the stored qubit

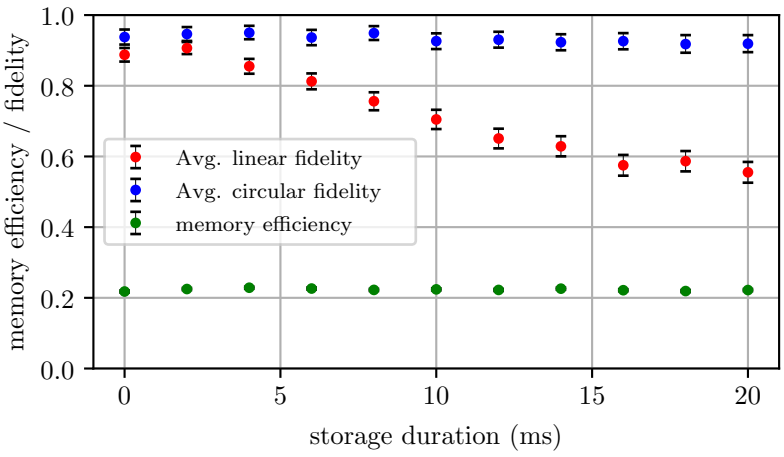

Figure 3.18.: Qubit fidelity and memory efficiency. The coherence of the memory is probed with four linearly polarized input states $|H\rangle$,$|V\rangle$,$|A\rangle$ and $|D\rangle$ and the average fidelity over the storage duration is shown as red dots. Analogously, the average coherence of the two circularly input states $|R\rangle$ and $|L\rangle$ is shown as blue dots. The total memory efficiency for writing and reading the polarization qubit is shown as green dots. The error bar indicates the standard deviation estimated from the sample size.

from magnetic field fluctuations. The storage protocol introduced in Section 3.3.1 is extended as follows: After the photonic qubit is mapped to the atomic states $|F{=}2,\ m_F{=}{-}1\rangle$ and $|F{=}2,\ m_F{=}1\rangle$ (Figure 3.17a) by the photon absorption process with a single-photon detuning of -20 MHz, the basis transfer is immediately applied to minimize the time the qubit is susceptible to magnetic-field-induced decoherence effects. To this end, the Raman pair with a frequency splitting δ_{R} which corresponds to the transition frequency $|F{=}2,\ m_F{=}{-}1\rangle \leftrightarrow |F{=}1,\ m_F{=}{-}1\rangle$, is interrogated for 46.1 μs to drive a π-transition (Figure 3.17b). With the completion of the basis transfer, the microwave source which controls the frequency splitting of the Raman pair (see Section 3.4.2.6) is set to match the frequency difference of the new qubit basis states $|F{=}1,\ m_F{=}{-}1\rangle$ and $|F{=}2,\ m_F{=}1\rangle$ to eliminate the qubit precession in the rotating frame of the Raman pair (3.17c). After a variable-length storage duration, the Raman pair is set again to match the two-photon resonance condition for the basis transfer, and the population in $|F{=}1,\ m_F{=}{-}1\rangle$ is transferred back to the $|F{=}2,\ m_F{=}{-}1\rangle$ state (Figure 3.17d). Finally, the photonic qubit is retrieved by utilizing the photon emission protocol (Figure 3.17e), and its polarization state is measured in a given basis by the polarization resolving single-photon detection setup presented in Section 3.3.2.4.

The performance of the qubit memory is evaluated regarding the overall efficiency and the fidelity of the retrieved state. The memory is probed with a weak-coherent pulse containing one photon on average with the four linearly polarized input states $|H\rangle$,$|V\rangle$,$|A\rangle$ & $|D\rangle$ and the two circularly polarized input states $|R\rangle$ and $|L\rangle$. To determine the fidelity, the retrieved photon is detected in the basis corresponding to the input state. For a full state-tomography needed to reconstruct the density matrix (see Section 3.2.1.6), each input state must be measured with three mutually orthogonal basis sets.

To evaluate the coherence, the fidelity of the 4 linearly polarized input states is averaged, and the result is shown in Figure 3.18 (green dots) as a function of the storage duration together with the average over the two circular input states (blue dots) and the memory efficiency (red dots). As discussed in Section 2.6, the efficiency is multiplied by a factor 1.3

to resemble the storage efficiency of single-photon Fock states.

As shown in Figure 3.18, the memory has a constant efficiency of (22.3±0.2)%. Also, the fidelity of circular-polarized input states does not significantly decrease over the storage duration while the coherence of the linearly polarized input states degrades on a time scale of 20 ms, which is more than one order of magnitude longer compared to the storage in the magnetically sensitive basis. Both, the conservation of the basis state amplitudes and the decay of the coherence can be well-observed in the reconstructed time-resolved density matrix shown in Figure 3.19. Besides the decay of coherence, the measured fidelity for short storage durations is significantly lower compared to the experiments without the basis transfer. This is attributed to the total Raman scattering probability of approximatively 6.4% for both basis transfers (see Section 3.4.2.4). Note that although scattering can also affect the storage of circularly polarized input states, only an incoherent decay to $|F{=}2, m_F{=}0\rangle$ can lead to the production of a photon with an orthogonal polarization compared to the input state. In contrast, for linearly polarization states, every photon retrieved after a Raman scattering event results in a random outcome. Therefore, linearly polarized input states are more affected by the scattering probability as it can be observed in the data.

Although the storage in the magnetically insensitive basis significantly increases the coherence time, the expectation due to the reduction of the sensitivity to magnetic field fluctuation of factor 500 is not met. The investigation of further decoherence mechanisms is subject to the next chapter.

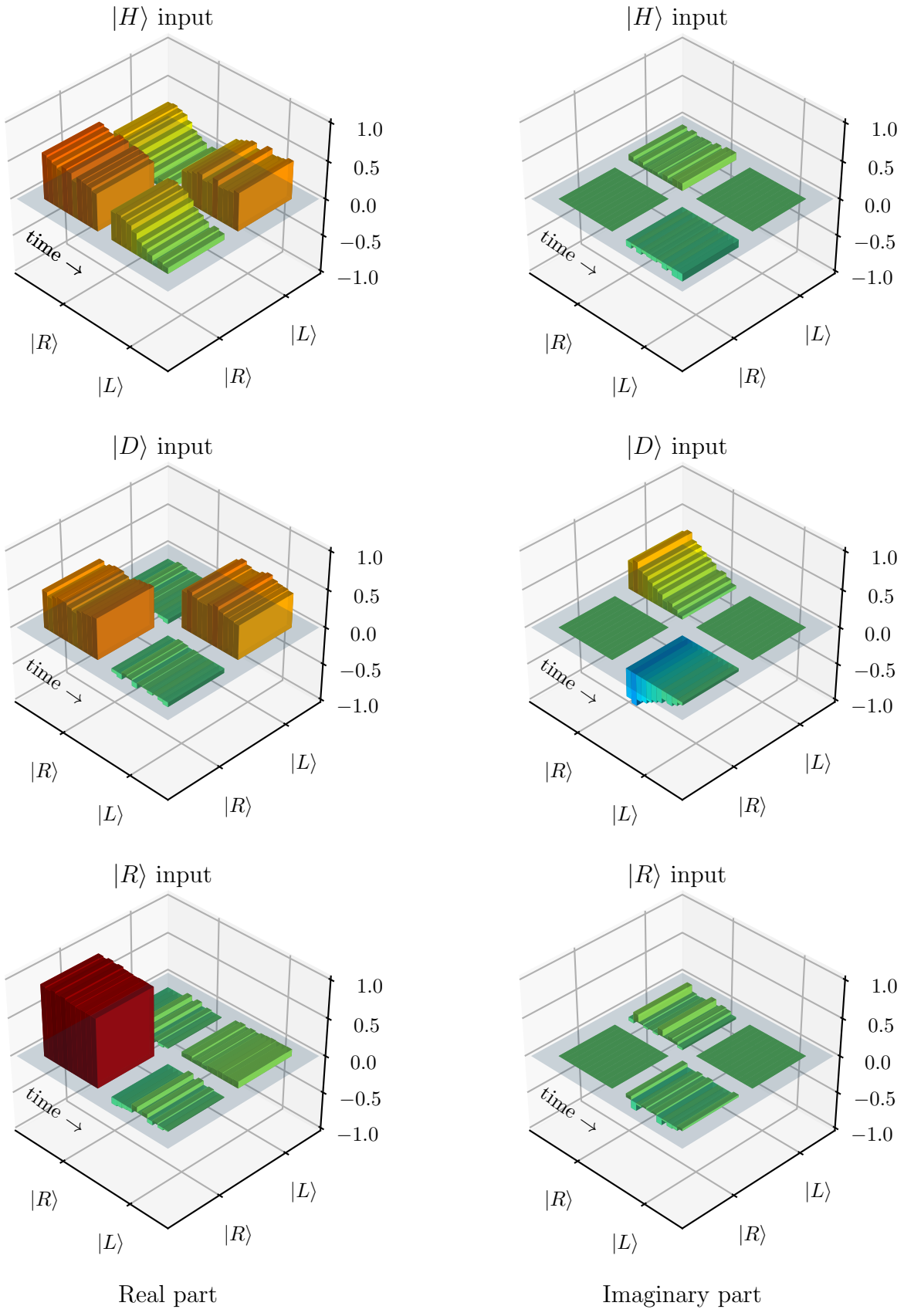

Figure 3.19.: Time-resolved density matrix. Reconstructed density matrices for $|H\rangle$, $|D\rangle$ and $|R\rangle$ input states with the real part on the left and the imaginary part on the right side. Each bar is divided into slices representing the different storage times between 0 and 20 ms. The time evolution goes from the back-left to the front-right.

3.4.4. Analysis of Decoherence Mechanisms

The mapping of the qubit to the decoherence protected basis increases the coherence time by one order of magnitude. The analysis of the sensitivity of the different qubit bases suggests an increase in coherence time by a factor of 500 if magnetic field fluctuations were the only source of decoherence. Further, the decoherence rate observed in the memory experiment resembles the decoherence rate seen with the Ramsey spectroscopy performed on the clock-state transition, that is highly insensitive to magnetic field fluctuations. Consequently, the observed decoherence must stem from additional mechanisms which cause a differential energy shift of the used qubit basis. Besides the magnetic fields, the energy of the atomic states is also influenced by the intense light-fields used to confine the atom at the center of the cavity.

In this section, the impact of the dipole beams on the coherence of the qubit stored on two different hyperfine states is explored. Employing a Ramsey spectroscopy for different trap beam intensities, the influence of the dipole traps to the coherence time is probed followed by an investigation of the mechanisms leading to decoherence.

3.4.4.1. Light as the Dominant Source of Decoherence

To demonstrate that the dominant source of decoherence is linked to the trapping beams confining the atom at the center of the cavity, the Ramsey experiment shown in Section 3.3.4.1 is repeated with two different sets of trapping beam intensities: the settings used for the measurement as shown in Section 3.3.4.1 and settings with approximately twice the beam intensities. With a beam intensity of 500 mW corresponding to a trap frequency of ≈311 kHz for the red-detuned 1064 nm dipole trap along the beam axis and an intra-cavity trap frequency of 473 kHz, the coherence of the clock-state decays with a characteristic time $\tau \approx (5.1 \pm 0.1)$ ms according to the fit by a Gaussian damped oscillation (see Figure 3.20). In contrast, for half the beam intensities with trap frequencies of 220 kHz and 335 kHz, the characteristic time of the decay is fitted to $\tau \approx (9.6 \pm 0.2)$ ms which is almost a doubling of the coherence time. Note that the usage of a Gaussian model to fit the dynamics of the decay does not result in perfect accordance and is not further justified. As it will be shown in the subsequent sections, the dynamics depends on a multitude of parameters. However, this suggests that the coherence of the memory is limited by effects introduced by the dipole traps.

3.4.4.2. Dipole Traps

To see how dipole traps can affect the coherence of the qubit, the dipole trapping mechanisms and its implementation in the setup are briefly discussed.

Optical dipole traps are a well-established technique to confine neutral atoms in small volumes. For a two-level atom with the resonance frequency ω_0, the dipole potential $V(\mathbf{r})$ of a linearly polarized light field with frequency ω, the associated potential depth V_0 and the effective detuning $\bar{\Delta}$ are given by [157]

$$V(\mathbf{r}) = \frac{d_0^2 \mathcal{E}^2(\mathbf{r})}{4\hbar\bar{\Delta}}, \qquad V_0 = \frac{d_0^2 \mathcal{E}_0^2}{4\hbar\bar{\Delta}} = \frac{\hbar\Omega_0^2}{4\bar{\Delta}}, \qquad \frac{1}{\bar{\Delta}} = \frac{1}{\omega - \omega_0} - \frac{1}{\omega + \omega_0}\ , \tag{3.74}$$

where d_0 is the atom's dipole moment and $\mathcal{E}(\mathbf{r})$ the electric field amplitude of the light field.

For a better resemblance of the experimental scenario, both the $5^2P_{1/2}$ and the $5^2P_{3/2}$

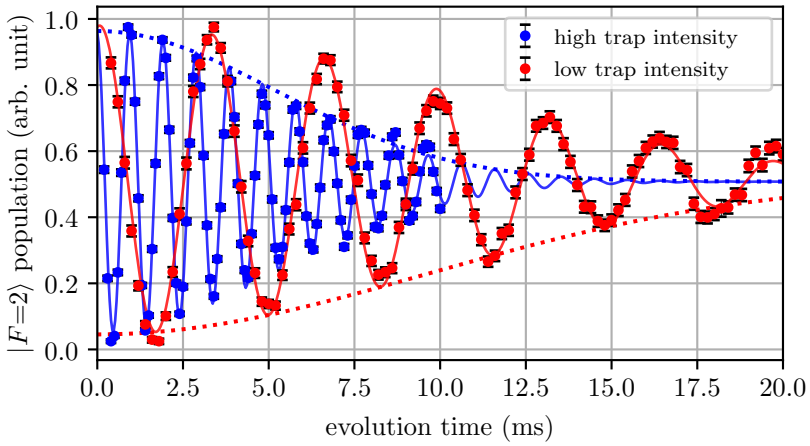

Figure 3.20.: Ramsey spectroscopy for different trap intensities. The coherence of the clock-state transition $|F{=}1, m_F{=}0\rangle \leftrightarrow |F{=}2, m_F{=}0\rangle$ is probed by employing a Ramsey spectroscopy for two different intensities of both dipole traps with a factor of approximately 2. The atom is first initialized in the $|F{=}1, m_F{=}0\rangle$. Then, using a microwave field, a $\pi/2$-pulse prepares the atomic population in a coherent superposition of $|F{=}1, m_F{=}0\rangle$ and $|F{=}2, m_F{=}0\rangle$. After a variable time of free-evolution, a second $\pi/2$-pulse is applied. Eventually, the state of the atom is detected with a cavity-assisted hyperfine state detection [152]. A small detuning is added to the microwave field during the free-evolution time to enforce the appearance of Ramsey fringes. This avoids a possible confusion between decoherence and an accidentally chosen small detuning. Besides this, the different oscillation frequencies of both measurements are arbitrary. The curves are fitted to a Gaussian damped oscillation, and the error bars correspond to the standard deviation estimated from the sample size.

levels must be taken into account, but due to the large detuning of the optical traps compared to the hyperfine splittings, each transition can be treated as a single line with an effective detuning $\bar{\Delta}_{\mathrm{D}_i}$ and the Rabi frequency $\Omega_{\mathrm{D}_i} = d_{\mathrm{D}_i}\mathcal{E}_0/\hbar$. In the case of ^{87}Rb the effective dipole moments in the far detuned regime for the D_1 and D_2 lines are directly related by $d_{D2} = \sqrt{2}d_{D1}$ and the interference between the transitions leads to a strength factor of $1/3$ for each transition. This yields the dipole potential

$$V_0 = \frac{1}{3}\cdot\frac{\hbar\Omega_{D1}^2}{4\bar{\Delta}_{D1}} + \frac{1}{3}\cdot\frac{\hbar\Omega_{D2}^2}{4\bar{\Delta}_{D2}} = \frac{\hbar\Omega_{D1}^2}{4}\frac{1}{3}\underbrace{\left(\frac{1}{\bar{\Delta}_{D1}} + \frac{2}{\bar{\Delta}_{D2}}\right)}_{\bar{\Delta}'^{-1}} = \frac{\hbar\Omega_{D1}^2}{4}\frac{1}{\bar{\Delta}'}. \tag{3.75}$$

with the effective detuning $\bar{\Delta}'$.

In the setup, two standing-wave traps are used to confine the atom inside the cavity: first, a blue-detuned intra-cavity trap (along the y-axis) with $\lambda_{\mathrm{blue}}{=}772\,\mathrm{nm}$ with the waist $w_{\mathrm{blue}} \approx 30\,\mu\mathrm{m}$. Second, a red-detuned trap with $\lambda_{\mathrm{red}}{=}1064\,\mathrm{nm}$ and a waist $w_{\mathrm{red}} \approx 16\,\mu\mathrm{m}$ which is aligned transversely to the cavity along the x-axis. For red detunings, atoms in their electronic ground state are attracted by high intensities. In contrast, for blue detunings, the atoms will be repelled by the light fields, and seek areas of low intensity. In 3D harmonic approximation and by ignoring the deconfining potential of the blue beam along the x- and z-axes, as well as the weakly confining potential of the red-detuned trap along the y-direction, the resulting potential is given by

$$V(\hat{\mathbf{r}}) = V_{\mathrm{const}} - \tfrac{1}{2}m\omega_x^2\hat{x}^2 + \tfrac{1}{2}m\omega_y^2\hat{y}^2 - \tfrac{1}{2}m\omega_z^2\hat{z}^2, \tag{3.76}$$

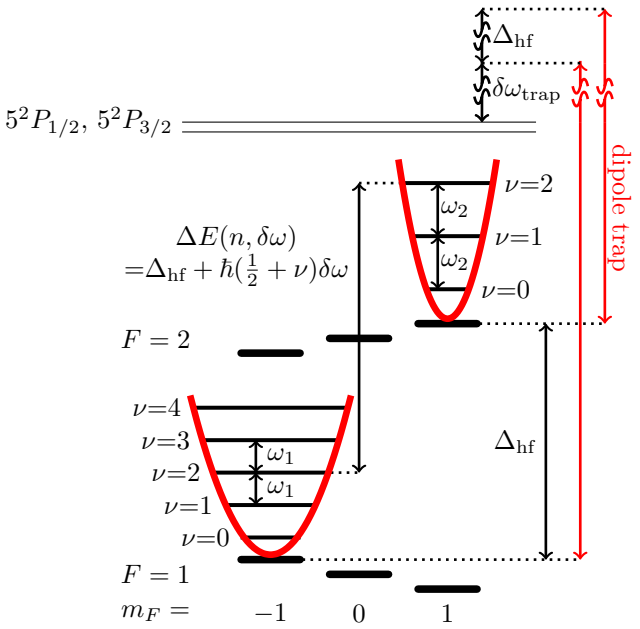

Figure 3.21.: Origin and impact of differential trap frequencies. The dipole beams (red arrows) induce a trapping potential by creating an intensity-depended light shift due to the off-resonant coupling to an optical transition. The created optical potential has a depth which is a function of the detuning of the dipole beams ($\delta\omega_{\mathrm{trap}}$). For a qubit stored on two different hyperfine states $|F{=}1/2\rangle$ the hyperfine splitting Δ_{hf} will result in different detunings of the dipole trap to the (most relevant) optical transition. This results in differential trap frequency $\delta\omega = \omega_2 - \omega_1$ for the two basis states and therefore to a motional state n dependent energy splitting $\Delta E(n, \delta\omega)$.

with the trap frequencies

$$\omega_x \approx \sqrt{\frac{-2V_0^{\mathrm{red}}}{m\lambda_{\mathrm{red}}^2}}\ , \quad \omega_y \approx \sqrt{\frac{2V_0^{\mathrm{blue}}}{m\lambda_{\mathrm{blue}}^2}}\ , \quad \omega_z \approx \sqrt{\frac{-4V_0^{\mathrm{red}}}{mw_{\mathrm{red}}^2}}\ . \tag{3.77}$$

3.4.4.3. Mechanical-State-Dependent Energy Splitting

To protect the qubit against magnetic field fluctuations, it is transferred to a magnetically insensitive basis in which the qubit is stored on a superposition of two energy eigenstates which are separated by the hyperfine splitting $\Delta_{\mathrm{hf}}{\approx}6.8\,\mathrm{GHz}$. As seen above, the depth of the dipole potential and the corresponding trap frequencies induced by the off-resonant trap beams are a function of the effective detuning $\bar{\Delta}'$. Consequently, due to the hyperfine splitting, the trap frequencies $\omega_{F=1,i}$ and $\omega_{F=2,i}$ for the qubit basis states and the motional axis i are discriminative.

For a given axis i with the relevant effective detunings $\bar{\Delta}'_{i,F=1}$, $\bar{\Delta}'_{i,F=2}$, the differential trap frequency can be expressed as

$$\delta\omega_i = \omega_{F=1,i}\left(\sqrt{\frac{\bar{\Delta}'_{i,F=1}}{\bar{\Delta}'_{i,F=2}}} - 1\right) = \omega_{F=1,i}\cdot(\alpha - 1)\ . \tag{3.78}$$

The factor α is given by the square root of the ratio of the detunings. Therefore, $\delta\omega_i$ is larger for trapping potentials formed by optical beams with a smaller detuning from the most relevant optical transitions.

Table 3.2.: Trap frequencies ω_{trap} and differential trap frequencies $\delta\omega_{\text{trap}}$ for the red-detuned 1064 nm and the blue-detuned 772 nm standing wave optical dipole traps along the x- and y-axis respectively.

axis	λ_{trap} (nm)	$\omega_{\text{trap},F=1}/2\pi$ (kHz)	$\delta\omega/2\pi$ (Hz)
x	1064	220	6.6
y	772	335	-259
z	1064	3.3	0.1

As depicted in Figure 3.21 for one dimension, the differential trap frequencies have an impact on the energy splitting ΔE of the qubit in the memory basis. The total energy difference is given by:

$$\Delta E_{\text{mem}} = \Delta_{\text{hf}} + \sum_{i\in(x,y,z)} \left(\nu_i + \frac{1}{2}\right) \delta\omega_i \hbar \ , \tag{3.79}$$

for the motional states ν_i for the three motional axis x, y, z.

Impact on the Coherence Time

As discussed in Section 3.2.1.2, the phase relation of the qubit basis states degrades with a fluctuating energy splitting ΔE. Here, $\delta\omega_i$ can lead to a fluctuating energy splitting by multiple mechanisms: The atom may be initialized in a statistical mixture of motional states such that ΔE fluctuates in the ensemble of memory realizations. Also, the motional state may change during the storage duration through a heating effect. Further, fluctuations of the trap intensity may result in an unstable energy splitting even when the atom is cooled to the motional ground state.

By employing Raman sideband cooling, the atom is cooled in the motional ground state along the cavity axis [118] which has the most significant differential trap frequency due to the relatively small detuning from the optical transitions. It was further verified that there is no significant heating effect in this direction on the timescale of the experiment. However, the motional states in the red-detuned 1064 nm dipole trap along the x- and z-axis are not known and will most likely be statistical mixtures which contribute to decoherence.

3.4.4.4. Fidelity Dynamics of a Thermal Ensemble

The dynamics of the fidelity of a qubit with the initial fidelity $\mathcal{F}_0$ in a thermal state with an average phonon number $\bar{\nu}$ and a differential trap frequency $\delta\omega_{\text{trap}}$ can be evaluated by superimposing the fidelity dynamics $\mathcal{F}(\nu)$ of a given motional state ν according to the thermal distribution (see A.5 for the derivation):

$$\begin{aligned}\mathcal{F}_{\text{thermal}}(t, \bar{\nu}, \delta\omega_{\text{trap}}) &= \sum_{\nu} p^{\bar{\nu}}_{\text{thermal}}(\nu) \cdot \mathcal{F}(t, \nu, \delta\omega_{\text{trap}}) \\ &= \frac{1}{2} + \frac{(2\mathcal{F}_0 - 1)}{2\,(\bar{\nu}+1)} \frac{1 - \frac{\bar{\nu}}{\bar{\nu}+1}\cos(\Delta\omega t)}{1 + \left(\frac{\bar{\nu}}{\bar{\nu}+1}\right)^2 - 2\alpha\cos(\Delta\omega t)}\end{aligned} \tag{3.80}$$

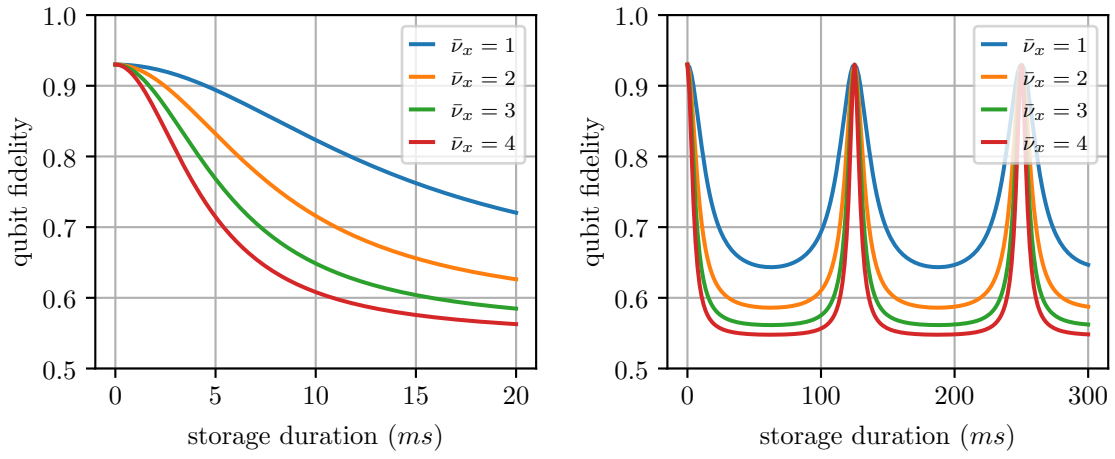

Figure 3.22.: Fidelity dynamics of a thermal ensemble. For a differential trap frequency of $\delta\omega_{\text{trap}}$=6.6 Hz corresponding to the dipole potential along the x-axis, the fidelity dynamics for a thermal ensemble with ν motional quanta are shown for short **(a)** and long storage durations **(b)**.

As it can be seen in Figure 3.22, a statistical mixture of motional states can lead to significant decoherence on a time scale which is much shorter than the corresponding differential trap frequency. Since the contribution to the qubit precession speed is an integer multiple of the differential trap frequency for all motional states in the statistical mixture, the fidelity of the qubit revives after T_{revive}=$1/\delta\omega_{\text{trap}}$. Note that the revival time relies on the harmonic approximation of the dipole trap and can be much longer for anharmonic traps. The existence of the revival has a significant consequence: Under the assumption that the relevant motional states in the 772 nm trap are indeed harmonic, the observed decoherence cannot be explained by the residual motional quanta along this axis due to the abstinence of revivals which should happen roughly all 5 ms. Further, the abstinence of oscillatory behavior in the data is a witness for the good quality of the ground state cooling.

If the decoherence model $\mathcal{F}_{\text{thermal}}(\nu)$ for $\delta\omega_{\text{trap}}$=6.6 Hz is fitted to the observed average decoherence of the linear input states, an agreement can be found for $\bar{\nu}_x = 2.7\pm0.3$ as it can be seen in Figure 3.23.

3.4.4.5. Position-Dependent Differential Light Shift

Besides the motional state, also the position of the atom within the trap affects the energy separation of the basis states and therefore the qubit coherence [158]. Although an imaging system capable of resolving the relative position of two atoms up to a single lattice site [159] is used to monitor the atom's position, drifts of the trap geometry or the imaging system stay undetected. Further, the position of the atom cannot be precisely controlled along the cavity axis. Also, to achieve a reasonable data rate despite the probabilistic atom distribution, the atom's position can only be restricted to a small range of lattice sites. Throughout the data acquisition, this can lead to a spread of the atom's position over a few lattice sites. Here, the associated decoherence mechanism is investigated.

The energy separation of the two hyperfine states not only results in differential trap frequencies but also in a differential light shift which is given by the difference in potential heights of the trapping potentials $\Delta V_0^{\text{red}}\approx$810 Hz. This value is a function of the beam

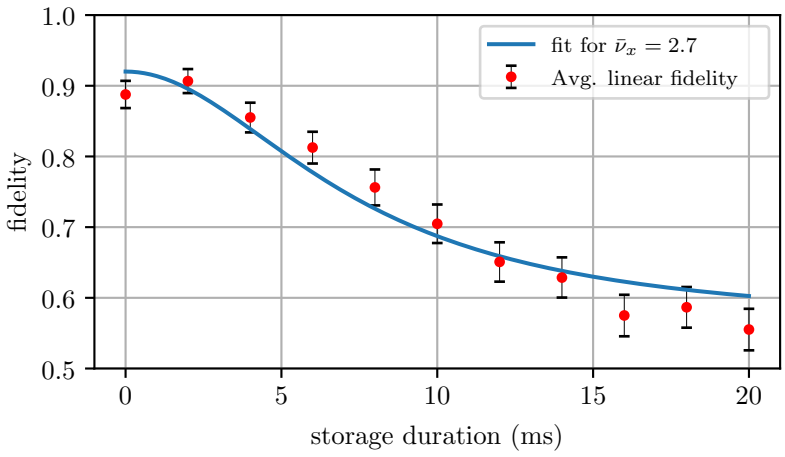

Figure 3.23.: Fit of the fidelity dynamics of thermal state to the observed coherence. The fidelity dynamics for a thermal state associated with a differential trap frequency $\delta\omega_{\text{trap}} = 6.6\,\text{Hz}$ fitted to the measured coherence with an agreement for $\bar{\nu}_x = 2.7 \pm 0.3$ motional quanta.

intensity of the red-detuned dipole trap, and its stability is crucial for the coherence of the qubit since it linearly affects the phase evolution speed. The beam intensity is actively stabilized to suppress dephasing due to intensity fluctuations, but the presence of the orthogonal blue-detuned intra-cavity trap leads to a sampling of beam intensities of the red-detuned trap by the atom: Due to the finite waist of the dipole trap's beam, the differential light shift is modulated over the lattice sites of the blue-detuned trap. For a Gaussian beam mode, the modulation can be analytically expressed as

$$\Delta V(z) = \Delta V_0 \cdot \exp\left(\frac{-\left(n_y \lambda_{\text{blue}}\right)^2}{w_y^2}\right) . \tag{3.81}$$

If the lattice sites occupied by the atom is a statistical mixture, the qubit decoheres in the ensemble of memory realizations. For a uniformly distributed atom position within a given range of n lattice sites centered around the lattice site with the maximum beam intensity, the expected decay of qubit coherence is shown in Figure 3.24a. It can be seen that that for a tolerance below 10 lattice sites, as it has been applied for the memory characterization, this mechanism is too weak to be the dominant cause of decoherence. If the effect for a spread over 10 lattice sites is superimposed with the decoherence for a thermal state, a good agreement with the measured results can be observed for $\bar{\nu} = 2.3 \pm 0.1$ motional quanta (see Figure 3.24b).

3.4.4.6. Conclusion

In this section two decoherence mechanisms induced by the dipole traps were identified: The storage on two different hyperfine states with a splitting which is not negligible with regard to the detuning of the dipole traps results in differential trap frequencies. If the atom is not initialized in a specific motional state but in a statistical mixture, the differential trap frequencies will result in a mixture of qubit precession speeds and therefore in decoherence. Further, a spread of the atom's position along the 772 nm beam results in a sampling of the intensity of the red-detuned dipole trap and therefore to a mixture of differential light shifts.

The observed decoherence can be well-explained for 2.3 ± 0.1 motional quanta along the strongly confining direction of the red-detuned 1064 nm dipole trap with a spread of the

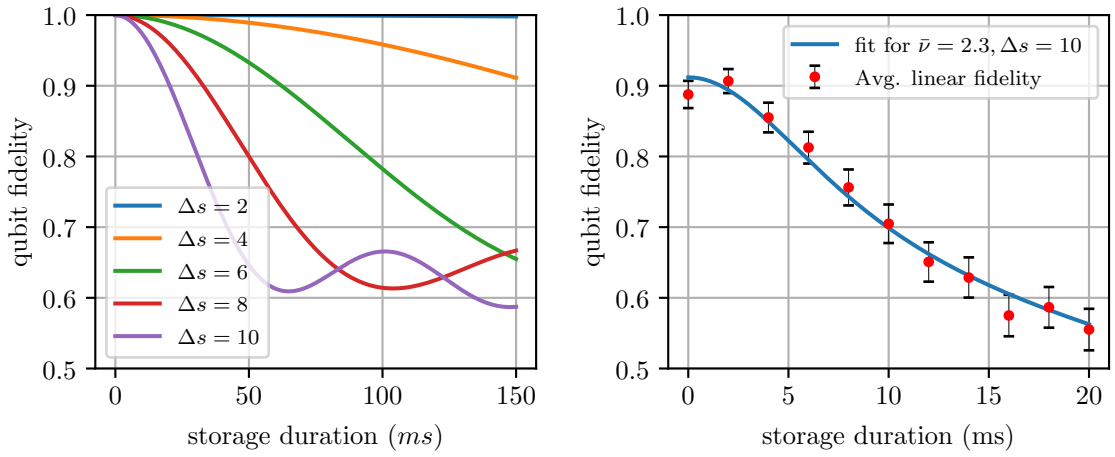

(a) Coherence over atom position spread

(b) Combined effects (spread=10,$\bar{\nu}_x = 2.26$)

Figure 3.24.: Decoherence due to a spread of atom positions. **a)** Shows the decay of the qubit fidelity for a uniformly distributed atom over Δs lattice sites around the center of the trap. **b)** Fitted coherence time with a model which incorporates both the fidelity decay due to a thermal state with $\bar{\nu}_x = 2.3$ and a spread over 10 lattice sites.

atom's position over 10 lattice sites in the direction of 772 nm blue-detuned dipole trap.

Both effects are linked to the imperfect initialization of the atom, and the resulting energy splitting of the qubit basis is constant during a single storage attempt. Such inhomogeneous dephasing effects are well-known to be reversible by the application of a spin-echo technique [132]. The implementation and the experimental test of a spin-echo will be subject of the next section.

3.5. Spin-Echo Memory

The coherence time of the qubit stored in the memory basis states, $|F{=}1, m_F{=}{-1}\rangle$ and $|F{=}2, m_F{=}1\rangle$, is not limited anymore by magnetic field fluctuations, but the dominant decoherence mechanisms are linked to the initialization of the atom: The motional degree of freedom of the atom in the direction of the red-detuned trap is not controlled and is distributed over multiple motional states. In addition, the localization of the atom is only restricted to a given range around the center. Both mechanisms result in an energy splitting which varies in the ensemble of the memory instances but is constant during a single storage attempt. Therefore, the phase evolution speed does not fluctuate on the timescale of a single memory instance. Those inhomogeneous dephasings are fully reversible by the spin-echo technique [132, 158, 160]: By swapping the population of the qubit basis states precisely in the middle of the storage duration, the effect of the inhomogeneous phase evolution speeds completely cancels after the full storage duration.

In this chapter, the spin-echo technique is utilized to cancel all reversible decoherence mechanisms to further extend to the coherence time of the memory compared to the one achievable by storing on the decoherence-protected basis (see Section 3.4.4). The chapter is structured like the following: First, the four-level Raman transfer derived in Section 3.4.2 is adapted to swap the population of the qubit basis states is discussed. Second, the details of the experimental realization are discussed, followed by a demonstration of a significantly prolonged coherence time when this technique is applied to the memory protocol. Finally,

the new limitations for the coherence time are investigated.

3.5.1. Population Swap Transfer

To apply the spin-echo technique, the population of the qubit basis states must be swapped in the middle of the storage duration. The corresponding two-photon transition (see Figure 3.25),

$$|F{=}1,\ m_F{=}{-1}\rangle \leftrightarrow |F{=}2,\ m_F{=}1\rangle \tag{3.82}$$

, can in principle be driven by a combination of two microwave fields in two-photon resonance condition or by a combination of a microwave and a radio frequency field. Unfortunately, as for the basis transfer (see Section 3.4.2.2), the shielding effect of the metalized piezo-ceramic tube holding the cavity mirrors inhibits the application of sufficiently strong fields. Therefore, this transfer must be driven optically by a two-photon stimulated Raman transition.

3.5.1.1. Four-Level Raman Driving

The desired four-level Raman transfer is covered by the theory derived in Section 3.4.2 when applied to the following levels of the $5^2S_{1/2}$ ground state and the $5^2P_{1/2}$ state:

$$|1\rangle = |F{=}1,\ m_F{=}{-1}\rangle\,, \qquad |2\rangle = |F{=}2,\ m_F{=}1\rangle\ , \tag{3.83}$$

$$|3\rangle = \left|F'{=}1,\ m_F{=}0\right\rangle, \qquad |4\rangle = \left|F'{=}2,\ m_F{=}0\right\rangle. \tag{3.84}$$

The schematics of this driving scheme are shown in Figure 3.25. Note that one beam of the Raman pair must be right-circularly polarized (σ^+) while the other beam has to be left-circularly polarized (σ^-). Due to experimental constraints, both beams consist of a balanced combination of σ^+- and σ^--polarized light since the beam is aligned on an axis perpendicular to the cavity axis. The resulting electrical field is given by

$$\vec{E} = E_i \frac{1}{\sqrt{2}} \left(\vec{\epsilon}_+ + e^{i\theta}\vec{\epsilon}_-\right) \cos(\omega_{Li} + \phi_i), \tag{3.85}$$

with the angle $\theta = 0$ between the beam axis and the normal of the quantization axis. In contrast to the transfer for the mapping between the memory and the interface basis where only π-polarized beams are utilized (see Section 3.4.2), only half of the electrical field contributes to the driving of the desired transition. By using the formula 3.56 the driving terms are determined,

$$\Omega_{13} = \frac{-1}{\sqrt{12}} \frac{E_{1+} d_0}{\hbar} e^{i\phi_1}, \qquad \Omega_{14} = \frac{-1}{\sqrt{12}} \frac{E_{1+} d_0}{\hbar} e^{i\phi_1}, \tag{3.86}$$

$$\Omega_{23} = \frac{1}{\sqrt{4}} \frac{E_{2-} d_0}{\hbar} e^{i\phi_2} e^{i\theta}, \qquad \Omega_{24} = \frac{-1}{\sqrt{4}} \frac{E_{2-} d_0}{\hbar} e^{i\phi_2} e^{i\theta}, \tag{3.87}$$

with the amplitudes $E_{1,2+}$, $E_{1,2-}$ of the electric fields corresponding to the right and left circular polarization components σ^+ and σ^-, respectively. The overall Rabi frequency is given by

$$\Omega_\perp = \frac{\Omega_{13}\Omega_{23}^*}{2\Delta_{12} + \Delta'} + \frac{\Omega_{14}\Omega_{24}^*}{2\Delta_{12} - \Delta'} \tag{3.88}$$

$$= \frac{e^{i(\phi_1 - \phi_2)}}{\sqrt{4 \cdot 12}} \frac{E_{1,+} E_{2,-} d_0^2}{\hbar^2} \left(\frac{1}{2\Delta_{12} + \Delta'} - \frac{1}{2\Delta_{12} - \Delta'}\right). \tag{3.89}$$

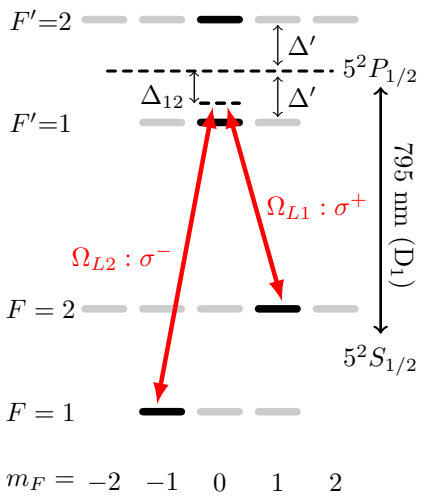

Figure 3.25.: Schematic of the population swap transfer. To apply the spin echo technique, the population of $|F{=}1,\, m_F{=}{-1}\rangle$ and the $|F{=}2,\, m_F{=}1\rangle$ state is swapped in the middle of the storage protocol by means of a Raman transfer with σ^-/σ^+ polarized beams.

As for the $\Delta m_F = 0$ transition (see Section 3.4.2), the driving frequency vanishes for large single-photon detunings. The optimal single-photon detuning $\Delta_{12} = 0$ is chosen with regard to the scattering probability as it was discussed in Section 3.4.2.4. Note that for this transfer, the scattering rate is twice the scattering rate of the basis transfer due to the combination of σ^- and σ^+ light in both driving fields.

3.5.1.2. State Selectivity

Once again, the Raman pair can potentially address multiple transitions unless a sufficiently strong bias magnetic field lifts the energy degeneracy. Since both Raman beams are a combination of σ^-- and σ^+-polarizations, there are two classes of transitions, $\Delta m_F{=}0$ and $\Delta m_F{=}\pm2$. The former are driven by two beams with the same circular polarization, and the latter is driven by two beams with orthogonal circular polarizations. The possible transitions group into three classes: transitions which have a magnetic field induced component in the two-photon detuning of $-2\delta_L$ shown in Figure 3.26a, transitions without magnetic field induced energy splittings shown in Figure 3.26b, and transitions with an additional splitting of $2\delta_L$ as shown in Figure 3.26c.

To avoid these undesired transfers, the ratio between the Zeeman splitting and the driving duration has to be chosen sufficiently large to not address transitions with a two-photon detuning of $\pm2\delta_L$ (see Section 3.4.2.3). Note that in contrast to the basis transfer, the difference in two-photon detuning with regard to unwanted transfers is only $2\delta_L$ compared to $4\delta_L$. This results in a diminished selectivity which can be compensated by either increasing the transfer duration or by increasing the Zeeman splitting. However, since the qubit is already in a decoherence-protected basis, a long transfer duration is not problematic.

As it can be seen in Figure 3.26b, the targeted transfer to perform the population swap, $|F{=}1,\, m_F{=}{-1}\rangle \leftrightarrow |F{=}2,\, m_F{=}1\rangle$, cannot be addressed without simultaneously driving the symmetric transition $|F{=}1,\, m_F{=}1\rangle \leftrightarrow |F{=}2,\, m_F{=}{-1}\rangle$. For an initial population restricted to the states $|F{=}1,\, m_F{=}\pm1\rangle$ the corresponding Hamiltonian in the basis

$$|F{=}1,\ m_F{=}{-1}\rangle, |F{=}2,\ m_F{=}{-1}\rangle, |F{=}1,\ m_F{=}{+1}\rangle, |F{=}2,\ m_F{=}{+1}\rangle \tag{3.90}$$

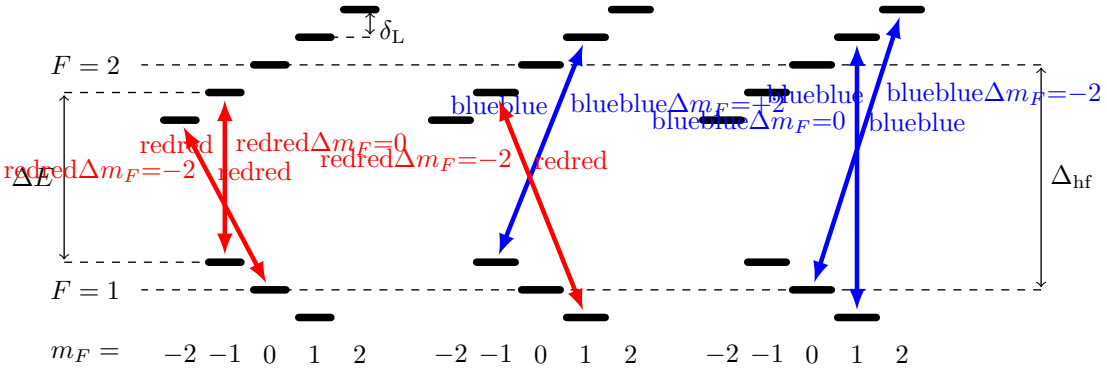

(a) $\Delta E = \Delta_{hf} - 2\delta_L$ **(b)** $\Delta E = \Delta_{hf}$ **(c)** $\Delta E = \Delta_{hf} + 2\delta_L$

Figure 3.26.: Possible transfers for σ^-/σ^+ polarized Raman beams. The stimulated Raman transition driven with $\sigma^{+/-}$-polarized beams can become two-photon resonant with Δm_F=0 and Δm_F=±2 transitions in three different classes of two-photon detunings: **a)** For a two-photon detuning δ of the hyperfine splitting Δ_{hf} minus two times the Zeeman splitting δ_L the states $|F$=1, m_F=0$\rangle$ and $|F$=1, m_F=−1$\rangle$ become resonant with $|F$=2, m_F=−1$\rangle$ and $|F$=2, m_F=−1$\rangle$, respectively. **b)** For $\delta = \Delta_{hf}$ the transition for the population swap transfer (blue) and the symmetric transition (red) are coupled. **c)** For $\delta = 2\delta_L + \Delta_{hf}$ the symmetric scenario of **a)** is realized. The color code of the arrows corresponds to the polarization of the photon created from the target state in the $|F$=2$\rangle$ manifold.

is given by (see Section 3.4.2.3)

$$\hat{H}_\perp = \frac{\hbar}{2}\begin{bmatrix} -2\delta_L & 0 & 0 & -\Omega_\perp \\ 0 & 2(\delta_{l.s.\perp} + \delta_\perp + \delta_L) & \Omega_\perp^* & 0 \\ 0 & \Omega_\perp & +2\delta_L & 0 \\ -\Omega_\perp^* & 0 & 0 & 2(\delta_{l.s.\perp} + \delta_\perp - \delta_L) \end{bmatrix}. \tag{3.91}$$

By choosing a detuning $\delta_\perp = -\delta_{l.s.}$ to compensate for the light shift, both transitions become resonant simultaneously. However, the concurrent transfer which populates $|F$=2, m_F=−1$\rangle$ is not problematic for the storage protocol since the population of $|F$=2, m_F=−1$\rangle$ will be swapped back to $|F$=1, m_F=−1$\rangle$ by the transfer between the interface and the storage basis and cannot contribute to the photon retrieval process.

Note that π-polarization components in the Raman beams will result in even more transfers with just one Larmor quanta detuning by combining a $\Delta m_F = \pm 1$ transition driven by a $\sigma^\pm$-polarized beam with a $\Delta m_F = 0$ transition induced by a π-polarized beam. Additionally, by combining two π-components, the clock-transition $|F$=1, m_F=0$\rangle \leftrightarrow |F$=2, m_F=0$\rangle$ without a detuning from the target transition can be driven. After a failed storage attempt with the atomic population remaining in the initial state $|F$=1, m_F=0$\rangle$, the clock-transition will populate $|F$=2, m_F=0$\rangle$, and this can result in the creation of a random photon. Therefore, it is crucial to carefully adjust the polarization of the Raman beams to avoid driving those unwanted transfers.

3.5.1.3. Conclusion

It was shown that the population-swap transfer to perform a spin-echo pulse is very similar to the basis transfer discussed earlier but has to be performed with two $\sigma^{+/-}$-polarized

beams to allow for a $\Delta m_F = 2$ transition. Again, a single-photon detuning between the two hyperfine levels of the D_1 line must be chosen to avoid destructive interference and to minimize the scattering probability. The latter is twice as high compared to the scattering of the basis transfer due to the second unused light components of the $\sigma^{+/-}$. Also, the detuning from unwanted transfers is only half the detuning for the basis transfers. To maintain an equally good suppression of those, the transfer must be driven slower compared to the basis transfer.

3.5.2. Experimental Realization

The population-swap transfer has the same requirements as the basis transfer discussed in Section 3.4.2.6: A carrier-free and power-stabilized Raman pair in a micro-second long pulse has to be impinged onto the atom from a direction perpendicular to the cavity axis in a well-defined linear polarization. The only difference to the basis transfer scenario is the polarization of the Raman pair and the frequency splitting of the sidebands. To drive π-transitions, the Raman pair has to be horizontally polarized in the propagation direction while for the $\sigma^{+/-}$-transitions, a vertical polarization is needed. For the basis transfer, a frequency splitting of $\Delta_{\mathrm{hf}} - 2\delta_L$ is needed to fulfill the two-photon resonance condition, and for the population swap transfer, the frequency splitting must be Δ_{hf}. However, as it was discussed in Section 3.4.2.6, to remove the qubit precession, in between the population transfers, the Raman pair is switched to match the energy difference of the qubit and therefore to the two-photon resonance of the population swap transfer. Consequently, the desired switching between the two necessary two-photon detunings is already implemented.

For the experimental realization, light from the previously described the Mach-Zehnder modulator is divided into two beam paths, one for the basis transfer and one for the population-swap transfer (see Figure 3.13). In each path an identical AOM setup as described in Section 3.4.2.6 is employed to create the desired pulse shape and to stabilize the pulse intensity by measuring the beam power downstream right before the cavity system and after filtering out undesired polarization components (see Figure 3.14).

3.5.3. Experimental Results

3.5.3.1. Driving Spectrum of the Population-Swap Transfer

A single atom is trapped at the center of the cavity mode and cooled into the motional ground state along the cavity axis by means of Raman sideband cooling. By employing a hyperfine state pumping technique [118], the atom is initialized in the $|F{=}1\rangle$ manifold in a randomly distributed Zeeman state. Subsequently, the Raman pair in the $\sigma^{+/-}$-configuration is impinged with a variable energy splitting to perform a two-photon detuning scan. The pulse duration is set to $40\,\mu$s which corresponds roughly to a $\pi/3$-transfer on the desired transition. After the Raman transfer, the photon emission protocol is utilized, and the potentially created photon is detected with the polarization-resolving detection setup in the $|R\rangle$ /$|L\rangle$ basis. The polarization yields information about the state the population was transferred to for a given two-photon detuning. See Section 3.4.3.1 for further details.

The spectrum shown in Figure 3.27 exhibits three peaks (please refer to Figure 3.26 for reference). The left green peak at a two-photon detuning of $(-67.46 \pm 0.05)\,$kHz corresponds to the transitions $|F{=}1,\, m_F{=}0\rangle \leftrightarrow |F{=}2,\, m_F{=}{-}2\rangle$ and $|F{=}1,\, m_F{=}{-}1\rangle \leftrightarrow |F{=}2,\, m_F{=}{-}1\rangle$. The right red peak at (57.82±0.05)kHz corresponds to the transfer $|F{=}1,\, m_F{=}0\rangle \leftrightarrow |F{=}2,\, m_F{=}2\rangle$ and $|F{=}1,\, m_F{=}1\rangle \leftrightarrow |F{=}2,\, m_F{=}1\rangle$. The green part of the

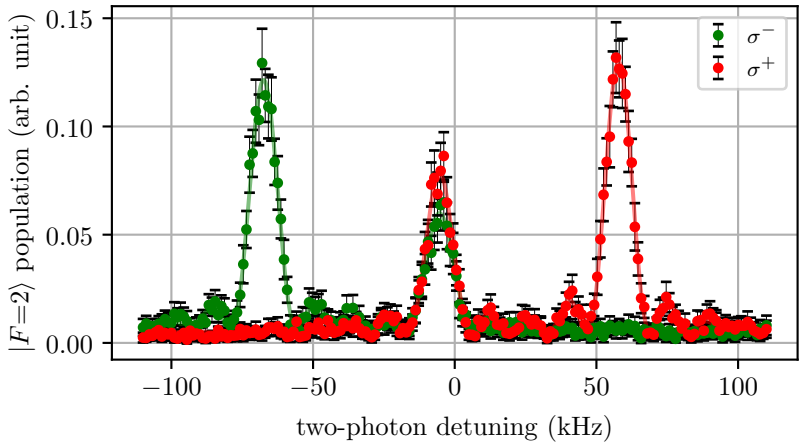

Figure 3.27.: Zeeman state selectivity of the population swap transfer The atom is initialized in $|5^2S_{1/2}, F{=}1\rangle$ with a randomly distributed Zeeman state. The population-swap Raman transfer is applied with a variable two-photon detuning for a duration corresponding roughly to a $\pi/2$-pulse. Subsequently, the photon production protocol is applied to probe the population of $|5^2S_{1/2}, F{=}2\rangle$. The polarization of the created photon is detected in the $|R\rangle, |L\rangle$ basis, yielding additional information about the atomic state after the Raman transfer.

central peak at $(-5.41{\pm}0.07)\,\mathrm{kHz}$ corresponds to the $|F{=}1,\, m_F{=}1\rangle \leftrightarrow |F{=}2,\, m_F{=}{-}1\rangle$ transition and the red part at $(-5.28{\pm}0.12)\,\mathrm{kHz}$ to the targeted population-swap transfer $|F{=}1,\, m_F{=}{-}1\rangle \leftrightarrow |F{=}2,\, m_F{=}1\rangle$. Note that although those two transfers cannot be spectrally resolved, the memory is not affected since the population transferred to $|F{=}2,\, m_F{=}{-}1\rangle$ is removed from the $|F{=}2\rangle$ manifold by the application of the second basis state transfer (see Section 3.5.1.2).

The spectrum is in a good agreement with the theoretical expectation and demonstrated a good separability of the transitions for the chosen magnetic field and transfer duration. With the value for the two-photon detuning for the population-swap transition, $\delta = -5.28\,\mathrm{kHz}$, the coherence of the transfer is probed in the subsequent section.

3.5.3.2. Coherence of the Population Swap Driving

To test the coherence and exact transfer duration on two-photon resonance the same procedure as for the basis transfer is used (see Section 3.4.3.2): A single atom is initialized in the motional ground state along the cavity axis and the $|F{=}1\rangle$ ground state in a randomly distributed Zeeman state by means of Raman sideband cooling and hyperfine pumping. The Raman pair on two-photon resonance with the two transitions

$$|F{=}1,\ m_F{=}{-}1\rangle \leftrightarrow |F{=}2,\ m_F{=}1\rangle\ , \tag{3.92}$$

$$|F{=}1,\ m_F{=}1\rangle \leftrightarrow |F{=}2,\ m_F{=}{-}1\rangle\ , \tag{3.93}$$

impinges onto the atom for a variable-length duration. Subsequently, the population of the $|F{=}2\rangle$ manifold is measured by employing the cavity-assisted hyperfine state detection method [152].

The population of the $|F{=}2\rangle$ manifold is shown in Figure 3.28 as the blue dots along with a fit to an exponentially damped oscillation. The time constant $\tau = 498.2{\pm}53.9\,\mu\mathrm{s}$ which corresponds to 2.33 Rabi cycles with a length of $T_{\mathrm{PS}} = 213.5\,\mu\mathrm{s}$ and a loss of 19.4%

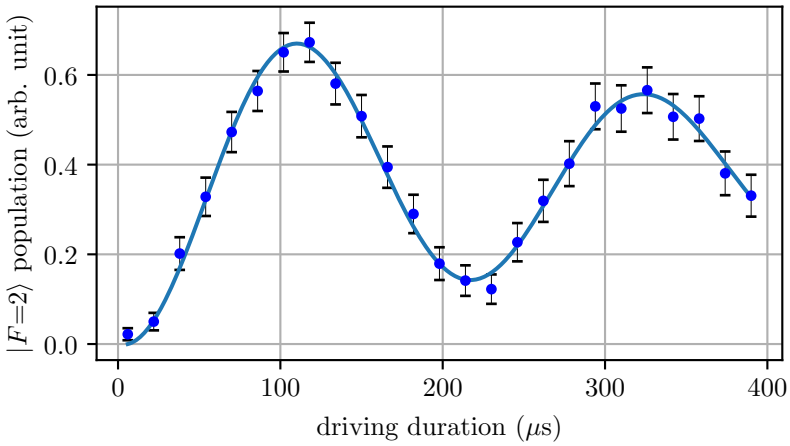

Figure 3.28.: population-swap transfer driving-duration sweep. A single atom is initialized in the $|F{=}1\rangle$ ground state manifold with a randomly distributed Zeeman state. The Raman pair in two-photon resonance to drive the $|F{=}1, m_F{=}{-}1\rangle \leftrightarrow |F{=}2, m_F{=}1\rangle$ and $|F{=}1, m_F{=}1\rangle \leftrightarrow |F{=}2, m_F{=}{-}1\rangle$ transitions is shown on the atom for a variable interrogation time. Finally, the population of the $|F{=}2\rangle$ manifold is probed by utilizing a cavity-assisted hyperfine detection method [152].

oscillation contrast per π-cycle. This value is 2.3 times the value for the basis state transfer (see Section 3.4.3.2) compared to a theoretically predicted estimate of 2.

With this measurement, the exact duration for a π-pulse was determined such that the spin-echo can now be applied for the qubit-storage protocol. From the observed decoherence of the driving, a significant impact on the qubit's fidelity is to be expected.

3.5.3.3. Qubit Coherence with Applied Spin-Echo

Here, the transfer which was characterized in the last two sections is employed to the photonic polarization qubit memory to revert inhomogeneous dephasing mechanisms by the application of a spin-echo pulse. To this end, the protocol for the storage of the qubit in the magnetic insensitive basis is extended by a population swap transfer $|F{=}1, m_F{=}{-}1\rangle \leftrightarrow |F{=}2, m_F{=}1\rangle$ at half the storage time.

After the atom is initialized in the $|F{=}1, m_F{=}0\rangle$ state within the motional ground state along the cavity axis, the photonic polarization qubit is mapped onto a coherent superposition of the atomic states $|F{=}2, m_F{=}1\rangle$ and $|F{=}2, m_F{=}{-}1\rangle$ (Figure 3.29a). By employing the basis-transfer protocol discussed in Section 3.4.2.2, the qubit is mapped to the magnetically insensitive basis by means of two π-polarized Raman beams (Figure 3.29b). During a free-evolution time, the two-photon detuning of the Raman pair is switched to the two-photon resonance condition of the qubit basis states. After half the predefined storage time T_{store}, the spin-echo pulse is applied by driving a π-transition by interrogating the Raman pair in $\sigma^{+/-}$-configuration for approximatively 107 μs (Figure 3.29c). Once the second half of the storage duration is over, the two-photon detuning δ_{Raman} is set again to the basis-transfer configuration and the initial basis configuration is restored (Figure 3.29d). Finally, the photonic polarization qubit is retrieved for subsequent state analysis (Figure 3.29e).

The memory is probed with four linearly polarized input states ($|H\rangle$,$|V\rangle$,$|D\rangle$,$|A\rangle$) and two circularly polarized input states ($|L\rangle$,$|R\rangle$). The resulting average coherence times for the

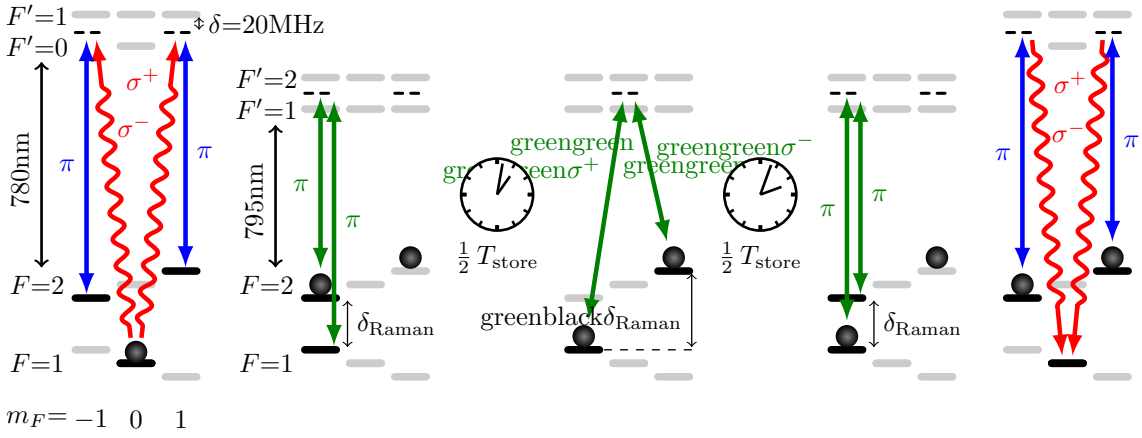

a) store qubit **b)** change basis **c)** apply spin echo **d)** revert basis **e)** read qubit

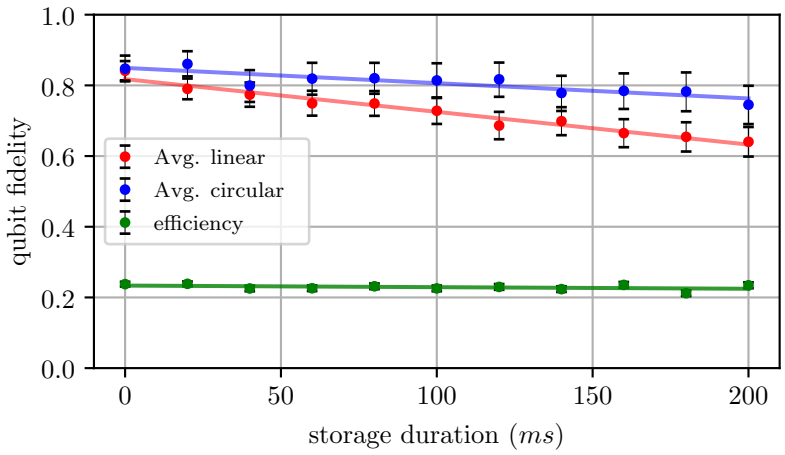

(f) memory coherence and efficiency

Figure 3.29.: Sequence and results for the memory with applied spin-echo. a-e) The photonic qubit is mapped onto the atom and the qubit base is subsequently changed to the magnetic field insensitive configuration. After half the predefined storage time, the spin-echo pulse is applied. Once the second half of the storage duration is over, the basis-transfer is reversed and the photonic qubit is retrieved. **f)** The resulting average fidelity of linearly polarized and circularly input states is shown by the red and blue dots, respectively. Despite the lag of a suitable model, the fidelities are fitted to a linear slope. The efficiency of the memory is indicated by the green dots.

linearly and circularly polarized input states are shown in Figure 3.29f (red and blue dots) along with the overall efficiency of the memory (green dots).

There are four important observations in the data set. First, the efficiency of the memory is constant over the full storage period. Second, the average fidelity of short storage times is reduced by almost 10% to 0.827±0.007 for linearly polarized input states and to 0.85±0.01 for circularly polarized input states. This reduction is in good agreement with the estimate from the characterization measurements. Third, the fidelity of linearly polarized inputs stays above the classical limit of $\mathcal{F} = 2/3$ for approximatively 200 ms and degrades with a seemingly constant rate of (9.3±0.6)%/100 ms. Fourth, the fidelity of circular polarizations also degrades with a rate $(4.3 \pm 0.8)\%/100\,\text{ms}$ which is almost half the rate of the linear polarization.

This result demonstrates that the application of the spin-echo technique indeed prolongs the coherence of the stored photon qubit by more than one order of magnitude. In contrast to the storage in the magnetically protected basis which allowed for arbitrary readout times, the timing of the spin-echo pulse determines the readout time. Although the application of multiple spin-echo pulses could cancel even higher-frequency noise-components and relaxes the timing constraint on the read-out, the scattering rates associated with the optical transfers and the resulting reduction of qubit fidelities renders this approach unfeasible. However, the decay of the fidelity of circularly polarized input states suggests that the coherence of the memory is no longer limited by dephasing mechanisms.

3.5.4. Light-Induced Dephasing Mechanisms

In previous storage experiments, the polarization qubit was stored up to 10 ms and the storage time was limited by the degradation of fidelity of linearly polarized input photons due to dephasing mechanisms. Here, the qubit is stored for more than 100 ms and both, the fidelity of the linear input polarizations as well as the circular input polarizations degrade over time. This is qualitatively different from the previous scenarios since the degradation of circularly polarized qubits cannot be explained by a fluctuating energy splitting. Since the circularly polarized qubits are stored on a single atomic eigenstate and not a coherent superposition, the limiting mechanism must affect the population amplitudes of the qubit basis states.

In this section, Raman scattering induced by the optical dipole traps is identified as the limiting mechanism to both the T_2 and the T_1 time of the memory. First, the reduction in memory fidelity for short storage times is discussed. Second, the impact of the red-detuned dipole trap is analyzed and the effective non-vanishing light intensity sampled by an atom trapped in a blue-detuned dipole trap is calculated to determine the associated scattering rate. Finally, the impact of scattering events on the qubit fidelity is approximated.

3.5.4.1. Scattering from the Red-Detuned Dipole Trap

In a red-detuned dipole trap, the atom is confined to regions of high light intensities resulting in a scattering rate Γ_{red}. The scattering must be divided into two mechanisms: Raman and Rayleigh scattering and according to [156] only the former results in a degradation of the qubit fidelity. With the formalism provided in [156] the Raman scattering rate is calculated by summing up all possible excitation-and-decay channels resulting in a change of the atomic population. In contrast, the Rayleigh scattering rate is determined by summing all the channels which maintain the atomic population. When the formalisms is applied to our experimental setup with the experimentally determined trap frequency of $\omega_x \approx 220\,\mathrm{kHz}$, a Rayleigh scattering rate of $\Gamma_{\mathrm{red,Rayleigh}} \approx 0.77\,\mathrm{Hz}$ and a Raman scattering rate of $\Gamma_{\mathrm{red,Raman}} \approx 1\,\mathrm{mHz}$ are calculated. Due to the large detuning of the dipole trap from the atomic transitions, Raman scattering is strongly suppressed and insignificant on the timescale of the memory. Therefore, scattering events linked to the far-red-detuned dipole trap are not the dominant source of fidelity decay.

3.5.4.2. Off-Resonant Scattering from the Blue-Detuned Trap

Blue-detuned dipole traps where atoms is confined at regions of low light intensity are often considered to neither cause light shifts or nor off-resonant scattering. However, the spatial extent of the atomic wave function results in a non-vanishing effective light intensity seen

by the atom and therefore in a scattering rate. The effective light intensity is calculated by convolving the spatial expectation value $p(y)$ of the ground state in a harmonic oscillator potential with the light intensity $I(y)$. In the second order Taylor approximation around the intensity minimum at $y = 0$ this yields

$$I_{\text{eff}} = \int p_0(y)I(y)dy = \int \sqrt{\frac{m\omega_y}{\pi\hbar}} e^{-\frac{m\omega_y}{\hbar}y^2} I_0 \left(2\pi\frac{y}{\lambda}\right)^2 dy = I_0 \frac{\pi\hbar}{\lambda m\omega_y} \tag{3.94}$$

with the maximum light intensity I_0 and the measured trap frequency $\omega_y \approx 335\,\text{kHz}$, the Rayleigh and Raman scattering rates can be calculated according to [156] as

$$\Gamma_{\text{blue,Rayleigh}} \approx 3\,\text{Hz}, \quad \Gamma_{\text{red,Raman}} \approx 0.7\,\text{Hz}\ . \tag{3.95}$$

In contrast to the scattering events associated with the red trap, Raman scattering has a significant contribution to the overall scattering rate due to the comparably low detuning from the optical transition of 8 nm.

3.5.4.3. Impact on the Qubit Fidelity

To understand the impact of the Raman scattering on the memory fidelity, four different rates must be taken into account.

$\Gamma_{2\to2}$: The storage was successful resulting in the atom to populate a state within the $\left|5^2S_{1/2}, F{=}2\right\rangle$ manifold. A scattering event leads to a redistribution of the atomic population in the $\left|5^2S_{1/2}, F{=}2\right\rangle$ manifold with a rate of $\Gamma_{2\to2}$.

$\frac{1}{\eta_w}\Gamma_{1\to2}$: The storage was not successful, and the atom is still populated in the $\left|5^2S_{1/2}, F{=}1\right\rangle$ manifold. A scattering event can populate the $\left|5^2S_{1/2}, F{=}2\right\rangle$ manifold resulting in the production of a random photon with a rate $\Gamma_{1\to2}$, which must be normalized with the write efficiency $\eta_{\text{write}} \approx 2/9$ for weak coherent pulses with $\bar{n} = 1$. This process increases the measured efficiency of the memory.

$\Gamma_{2\to1}$: The storage was successful but a scattering event depopulates the $\left|5^2S_{1/2}, F{=}1\right\rangle$ manifold with the rate $\Gamma_{2\to1}$ thus resulting in no photon being produced. This channel decreased the measured efficiency of the memory.

$\frac{1}{\eta_w}\Gamma_{1\to1}$: The storage was not successful and scattering events only populate the $\left|5^2S_{1/2}, F{=}1\right\rangle$ manifold with the rate $\Gamma_{1\to1}$ resulting in not producing a photon. Again the rate must be renormalized with the efficiency of the writing process.

The observed memory efficiency is not changing significantly over the storage duration. Therefore, the processes which populate and depopulate the states used for the qubit are compensating each other. Here, it is neglected that one state within the $|F{=}1\rangle$ and the $|F{=}2\rangle$ manifold are temporally interchanging their role due to the storage in the decoherence protected basis. For an exact calculation, it is necessary to determine the population of the $|F{=}1\rangle$ manifold after a failed storage attempt and the population of the $|F{=}2\rangle$ manifold, which also has a random component due to incoherent scattering events during the storage process (see Section 2.4.4). Additionally, multi-scatter events have to be taken into account. Therefore, this serves only as a rough estimation to confirm off-resonant scattering from the trap as the limiting mechanism. The estimated rate with which the memory is converted into a random photon generator is given by

$$\Gamma = \Gamma_{2\to2} + \frac{1}{\eta_w}\Gamma_{1\to2} \approx 3.2\,\text{Hz}\ . \tag{3.96}$$

This estimation suggests a reduction in the fidelity for linear input polarization from 0.85 to 0.74 within 100 ms which is in agreement with the experimental results. Note that atomic states corresponding to circularly polarized input photons are less affected because the atomic population has a higher chance to decay to its initial state rather than the orthogonal state. For instance, if the atom is in $|F{=}2, m_F{=}1\rangle$, a single scattering event can populate $|F{=}2, m_F{=}0\rangle$, $|F{=}2, m_F{=}1\rangle$ or $|F{=}2, m_F{=}2\rangle$ within the $|F{=}2\rangle$ manifold but only $|F{=}2, m_F{=}0\rangle$ can contribute to the retrieval of the wrong circular polarization. In contrast, for linear input polarization, a scattering event always results in a total loss of the phase relation.

3.5.4.4. Conclusion

The application of the population swap transfer is linked to a higher scattering probability which reduces the achievable fidelity. Further, it was shown that the storage time of the memory is not limited by dephasing mechanisms but by Raman scattering events. Although blue-detuned dipole traps are often considered to be not harmful since the atom is trapped at low electric fields, here the blue-dipole trap turned out to be the limiting factor due to its comparably low detuning from atomic resonance and the resulting Raman scattering rate. For a significant improvement, the employment of only far-detuned dipole traps suppresses the Raman scattering events and therefore the observed decoherence. Alternatively, the trap intensities can be either dynamically or constantly reduced.

4.Summary and Outlook

The research performed during this thesis project is focussed on improving cavity mediated absorption and emission of a single photon from a single atom, and the long-lived storage of qubits encoded in the polarization degree of freedom of a single photon, motivated by the significance for the formation of future photonic based quantum networks.

In the first part of this thesis, a formalism for the cavity-mediated emission (absorption) of a single photon from a single atom was derived and applied to the atom-cavity system used throughout this research project. The formalism is based on the work by Gorshkov *et al.* and describes the relation between the temporal mode of the emitted (absorbed) photon and the applied control Rabi frequency, as well as the efficiency of the emission (absorption) process. In contrast to the previous studies, the formalism does not assume a three-level atom but incorporates all excited states, which are coupled by either the cavity mode or the control pulse. It was shown that the influence of additional excited states becomes increasingly significant for larger atom-resonator detunings due to the interference between competing transfers mediated by different Λ-systems and the probability to incoherently scatter from one of the excited states. The interference renders the light-matter coupling a function of the single-photon detuning, which affects both the efficiency of the emission (absorption) process and the relation between the emitted (absorbed) temporal mode and the control pulse. Furthermore, the presence of multiple excited states results in additional light-shifts, which affect the two-photon condition and must be compensated by dynamically shifting the center frequency of the control pulse. In the three-level formalism, those effects are not covered resulting in an inaccurate relation between the temporal mode and the control pulse, which becomes significant for single-photon detunings in the order of a cavity bandwidth. The use of an incorrect control pulse results in the emission of a deformed temporal mode and in a deduction of the photon absorption efficiency due to the temporal mode mismatch.
With an additional numerical analysis of incoherent processes caused by atomic decay, a good correspondence between the predictions and the experimental results was achieved with one exception. The efficiency of the absorption process is approximately 0.5 of the theoretical expectation, independent of the single-photon detuning. Although the source of this constant effect was not identified within this research project, the experimentally observed degradation of the absorption efficiency with an increasing single-photon detuning was resolved. This is an essential step towards the formation of network-enabled quantum computation nodes because single-photon detunings in the order of multiple cavity bandwidths are crucial for the scaling of the light-matter interface to multiple atoms with controllable light-matter interactions. Furthermore, the precise and independent control over the absorbed and emitted photonic modes was utilized to demonstrate the interconversion between temporal modes. With a conversion range of at least three orders of magnitude in the temporal extent of the absorbed and emitted photons, this system may become useful for creating compatibility between different quantum platforms in an hybrid network.
The efficiency-limitation of the light-matter interface stems from the finite cooperativity of the employed cavity system. A new generation of fiber-based micro-cavities exhibit significantly smaller mode volumes and allow for larger cooperativities, which will boost the achievable efficiency of the light-matter interface in the future.

In the second part of this thesis, the coherence time for the storage of a photonic polariza-

tion qubit was extended by almost three orders of magnitude. The qubit was temporally mapped from the atomic basis used for the light-matter interface to a second basis that is insensitive to magnetic field fluctuations. Although this basis transfer can in principle be done by driving quadrupole transitions with a microwave field, the transition had to be driven optically due to the shielding effect of the piezo tube surrounding the employed cavity system. To this end, a general formalism to describe Raman driving in a four-level system was derived, and the optimal single-photon detuning was evaluated with regard to the expected incoherent scattering rate. The experimental application of this basis transfer prolonged the coherence time of the quantum memory to a few milliseconds and an analysis of the residual decoherence revealed that mechanisms linked to an imperfect initialization of the atom limited the coherence of the memory. The most dominant effect stemmed from a statistically mixed motional state in the dipole trap potential, and a secondary mechanism was caused by a spread of atom-positions in the optical lattices. Both mechanisms result in inhomogeneous dephasing, which can be reverted by the application of the spin-echo technique. To this end, the derived four-level Raman transfer was applied again to swap the population of both atomic basis states after half of the storage duration. This application leads to a coherence time of more than 100 ms, and the analysis of the residual decoherence showed that the memory is no longer limited by dephasing mechanisms but by Raman scattering from the near-resonant blue-detuned optical dipole trap.
The achieved coherence time of more than 100 ms is a significant breakthrough in the context of quantum networks. The classical signaling time between two farthest places on opposite sites of the earth establishes 66 ms as the lower bound needed for the direct teleportation of qubits in a global quantum internet. The results presented here are the first demonstration of photonic qubit storage beyond this threshold and establish cavity-based qubit memories as a promising candidate for future quantum-internet platforms.
The observed limitations of the coherence time are not fundamental and can be overcome technologically. By employing only far-detuned dipole traps the currently limiting Raman scattering rate can be suppressed. Next generation optical setups based on fiber-cavities may enable faster microwave transitions and potentially allow for the replacement of the optical transfers with one- or two-photon microwave transitions. Thereby, the loss in fidelity caused by incoherent scattering associated with the optical transfers could be eliminated, and a dynamic decoupling scheme could be employed, which also would lift the readout-timing constraints introduced by the spin-echo. Alternatively, three-dimensional ground state cooling and better atom positioning may allow for equally good coherence times without the spin-echo.

In the future, the presented results could be utilized for the formation of a multi-atom quantum memory. In such an experiment, the ability to use significant single-photon detunings demonstrated in the first chapter need to be combined with the qubit storage capabilities. To achieve independent storage and retrieval, the control pulse must be applied through an optical addressing system [118]. In a second step, the basis changing abilities presented here could be further extended to transfer the qubits to a basis that is compatible with the reflection mechanism used to mediate quantum gates [95]. The combination of a photonic multi-qubit memory with the ability to mediate gates between qubits would yield a fully functional quantum-network-enabled computation node.

5.List of publications

Accurate photonic temporal mode analysis with reduced resources
O. Morin, S. Langenfeld, M. Körber & G. Rempe
Phys. Rev. A, volume **101**, 013801 (2020)

Deterministic Shaping and Reshaping of Single-Photon Temporal Wave Functions
O. Morin, M. Körber, S. Langenfeld & G. Rempe
Phys. Rev. Lett, volume **123**, 133602 (2019)

Decoherence-protected memory for a single-photon qubit
M. Körber, O. Morin, S. Langenfeld, A. Neuzner, S. Ritter & G. Rempe
Nature Photonics, **12**, pages 18–21 (2018)

Langlebiger Qubitspeicher für Einzelphotonen
M. Körber & G. Rempe
Physik in unserer Zeit, **49**, 2 (2018)

Increased dimensionality of Raman cooling in a slightly nonorthogonal optical lattice
A. Neuzner, S Dürr, M. Körber, S. Ritter & G. Rempe
Phys. Rev. A, **98**, 013401 (2018)

Interference and dynamics of light from a distance-controlled atom pair in an optical cavity
A. Neuzner, M. Körber, O. Morin, S. Ritter & G. Rempe
Nature Photonics **10**, pages 303–306 (2016)

Breakdown of atomic hyperfine coupling in a deep optical-dipole trap
A. Neuzner, M. Körber, S. Dürr, G. Rempe & S. Ritter
Phys. Rev. A, **92**, 053842 (2015)

6. Acknowledgements

In the course of this PhD project, I had the privilege to work amongst a group of exceptionally talented and inspiring individuals. My time at the MPQ facilitates one of the most valuable experiences I had both on the professional as well as on the personal level.

Among all people who deserve my gratitude, I first want to thank Prof. Dr. Rempe for giving me the opportunity to do my PhD project in his research group and to contribute to this highly interesting research topic. Prof. Rempe always provided me with the right mixture of guidance and interest in the ongoing research, while simultaneously maintaining the spirit of self-determined research activities. I am highly thankful for this work experience and the trust he put in me.

I want to thank Dr. Adreas Neuzner for being an outstanding mentor during our shared time at the MPQ and Dr. Stephan Ritter for always keeping his door open to provide guidance and advise. I had the pleasure to work with Dr. Olivier Morin for almost half a decade and I am thankful for his willingness to share his expertise.

Further, I want to thank Dr. Manuel Uphoff, Dr. Bastian Hacker and Dr. Stephan Welte for the countless discussions we had to exchange knowledge between the teams.

A very special thanks goes to Dr. Stephan Dürr for the great amount of knowledge and wisdom he provided over the years.

Organizing a conference was an intense experience, and I want to thank Dr. Alexander Prehn, Dr. Thomas Gantner, Steffen Schmidt-Eberle and Martin Ibrügger for their outstanding teamwork making the YAO-Munich conference a success.

I am also grateful to Dr. Joseph Dale Christesen, Dominik Niemitz and Stefan Langenfeld to proofread this thesis and identify numerous mistakes.

Having real friends in your working group is a priceless privilege and I want to thank Dr. Isabel Rabey, Nicolas Tolazzi, Lukas Hartung and Christopher Ianzano for the great time we spent together.

Being involved in fascinating research is an absorbing experience and I want to thank Dr. Michael Gschwender, Dr. Matthias Rudolph and Miriam Hammerschmidt for maintaining our friendships.

Without my parents this thesis would not have happened, and I want to express my deepest gratitude for raising and supporting me throughout my whole life. Finally, I want to thank Antje for always being at my side over the course of the thesis.

A. Appendix

A.1. Population Dynamics of the Excited States

In a first step the differential equation 2.99 for the dynamics of the excited states is solved for the case of photon production where the incoming field mode is empty:

$$\epsilon_{\text{in}}(t) = 0 \ . \tag{A.1}$$

With the definition of the cooperativity

$$C_i = \frac{g_i^2}{\gamma\kappa} \tag{A.2}$$

the linear equation system for the expectation values P_i is given by

$$P_i = \frac{1}{(\gamma\,(1+C_i) + i\delta_i)} \left(-\sum_{j\neq i} \frac{g_j g_i}{\kappa} P_j + i\Omega_{c,i}(t) S \right) \qquad \forall i \in 1, 2, \ldots, N \tag{A.3}$$

With the abbreviations

$$\alpha_i = \gamma\,(1+C_i) + i\Delta_i \qquad \beta_{i,j} = \frac{g_j g_i}{\kappa} \tag{A.4}$$

the linear equation system can be written in the canonical form

$$\alpha_i P_i + \sum_{i\neq j} \beta_{i,j} P_j = i\Omega_{c,i}(t) S. \tag{A.5}$$

With the matrix elements

$$A_{i,j} = \begin{cases} \alpha_i & \text{for } i = j \\ \beta_{i,j} & \text{for } i \neq j \end{cases}$$

and the normalized Rabi frequency $\Omega_c(t)$ such that

$$\Omega_{c,i}(t) = c_{s,i}\Omega_c(t) \tag{A.6}$$

the general matrix representation for the N-level equation system is given by

$$\underbrace{\begin{pmatrix} \alpha_1 & \beta_{1,2} & \beta_{1,3} & \ldots & \beta_{1,N} \\ \beta_{2,1} & \alpha_2 & \beta_{2,3} & \ldots & \beta_{2,N} \\ \beta_{3,1} & \beta_{3,2} & \alpha_3 & \ldots & \beta_{3,N} \\ \vdots & \vdots & \vdots & \ddots & \vdots \\ \beta_{N,1} & \beta_{N,2} & \alpha_3 & \ldots & \alpha_N \end{pmatrix}}_{A} \underbrace{\begin{pmatrix} P_1 \\ P_2 \\ P_3 \\ \vdots \\ P_n \end{pmatrix}}_{P} = \underbrace{\begin{pmatrix} c_{s,1} \\ c_{s,2} \\ c_{s,3} \\ \vdots \\ c_{s,N} \end{pmatrix} \Omega_c(t) S}_{b} .$$

Note that the normalized Rabi frequency $\Omega_c(t)$ assumes that the system is either driven by only one classical field and the driving strength The solution for the population dynamics of all excited states can be found by multiplying the inverse matrix A^{-1} from the left side.

$$\underbrace{A^{-1}A}_{1} P = A^{-1} b$$

General solutions

For only one excited state, the solution for P is given by

$$P^{(N=1)} = \frac{c_{s,1}}{\alpha_1}\Omega_c(t)S$$

This result resembles the findings in Gorshkov et al. In a system with two excited states the solution vector is

$$P^{(N=2)} = \frac{1}{\alpha_1\alpha_2 - \beta_{1,2}^2}\begin{pmatrix} c_{s,1}\alpha_2 - c_{s_2}\beta_{1,2} \\ c_{s,2}\alpha_1 - c_{s_1}\beta_{1,2} \end{pmatrix}\Omega_c(t)S$$

The solution for a system with three excited states is given by

$$P^{(N=3)} = \frac{1}{\alpha_1\alpha_2\alpha_3 - \alpha_1\beta_{2,3}^2 - \alpha_2\beta_{1,3}^2 - \alpha_3\beta_{1,2}^2 + 2\beta_{1,2}\beta_{1,3}\beta_{2,3}}$$

$$\times \begin{pmatrix} c_{s1}(\alpha_2\alpha_3 - \beta_{2,3}\beta_{3,2}) - c_{s2}(\alpha_3\beta_{1,2} + \beta_{1,3}\beta_{2,3}) - c_{s3}(\alpha_2\beta_{1,3} + \beta_{1,2}\beta_{2,3}) \\ c_{s2}(\alpha_1\alpha_3 - \beta_{1,3}\beta_{3,2}) - c_{s1}(\alpha_3\beta_{1,2} + \beta_{1,3}\beta_{2,3}) - c_{s3}(\alpha_1\beta_{1,3} + \beta_{1,2}\beta_{1,3}) \\ c_{s3}(\alpha_1\alpha_2 - \beta_{1,2}\beta_{2,1}) - c_{s1}(\alpha_2\beta_{1,3} + \beta_{1,2}\beta_{2,3}) - c_{s2}(\alpha_1\beta_{2,3} + \beta_{1,2}\beta_{2,3}) \end{pmatrix}\Omega_c(t)S$$

Due to the form of the equation system where the Rabi frequency $\Omega_c(t)$ for the individual exited states can be factored out, all components P_i of P which describe the populations of the individual excited states behave equally up to a complex but constant factor which is governed by the Clebsch-Gordan coefficients and the single-photon detunings. All P_i are proportional to the Rabi driving frequency $\Omega_c(t)$ and the population S of the storage state $|s\rangle$ which will be solved in the next step.

A.2. Photon Shape Control

In this section, the time dependent Rabi frequency $\Omega_c(t)$ for the control laser to create an arbitrary photon shape $\epsilon_{\text{out}}(t)$ which results in the optimal efficiency η is derived. As shown in Section 2.3 the details of the atom-cavity system are exclusively contained in the factors $K(\Delta_i, c_{g,i}, c_{s,i})$ and $L(\Delta_i, C, \eta_{\text{esc}}\gamma, c_{g,i}, c_{s,i})$ and the resulting differential equations are of the same form as for the three-level system [90]. Therefore, the derivation of the control $\Omega_c(t)$ is kept briefly.

First, the retrieved mode $\epsilon_{\text{out}}(t)$ is renormalized

$$e(t) = \sqrt{\eta_R}^{-1}\epsilon_{\text{out}}(t)\ . \tag{A.7}$$

and the square of the absolute value is integrated using 2.54

$$\int |e(t)|^2 = 1 - \exp\left(-2\Re(K)h(t)\right)\ . \tag{A.8}$$

By using the time derivative and the relation $h(t) := \int_{t_0}^{t} |L|^2 dt'$ the absolute value of the control driving field can be extracted

$$|\Omega(t)| = \frac{|e(t)|}{\sqrt{2\Re(K)\exp\left(-2\Re(K)h(t)\right)}} = \frac{|e(t)|}{\sqrt{2\Re(K)\int_t^\infty |e(t')|^2 dt'}} \tag{A.9}$$

The phase can be extracted from 2.54 by using the arg function:

$$\arg(\epsilon_{\text{out}}(t)) = \underbrace{\arg(\eta_R)}_{0} + \arg(e(t)) = \underbrace{\arg(L)}_{const.} + \arg(\Omega_0) + \arg(\exp(-Kh(t))) \ , \tag{A.10}$$

$$\Rightarrow \arg(\Omega_0) = \arg(e(t)) + \arg(\Im(K)h(t)) \ . \tag{A.11}$$

With $h(t)$ extracted from A.8 the control Rabi frequency is given by

$$\Omega_c(t) = \frac{e(t)}{\sqrt{2\Re(K)\int_t^\infty |e(t')|^2 dt'}} \exp\left(-i\frac{Im(K)}{2\Re(K)} \ln\left(\int_t^\infty |e(t)|^2 dt'\right)\right) \tag{A.12}$$

The complex control Rabi shape Ω_0 allows the storage of any smooth incoming photon shape $e(t)$ with an efficiently $\eta(\delta) = \frac{|\Theta|^2}{2\Re(K)}$ which is only a function of the single-photon detuning δ.

A.3. Phase Consideration

In the following paragraph, the role of the phase for the different transfers and the free evolution during storage will be further investigated. In this section, the impact of the phase offset and a strategy to remove is discussed.

For the storage of the qubit on the basis pair $|F{=}2, m_F{=}1\rangle$ and $|F{=}2, m_F{=}{-}1\rangle$ the qubit relative phase evolves with twice the Larmor frequency (see Section 3.3.1). In the magnetically insensitive basis $|F{=}2, m_F{=}1\rangle$ and $|F{=}1, m_F{=}{-}1\rangle$, the qubit rotates approximatively at the frequency of the hyperfine splitting $\Delta_{\text{hf}} \approx 6.8\,\text{GHz}$. By maintaining the control of the phase of the Raman pair with respect to the qubit, the fast rotation can be compensated. What is crucial here is the phase of the driving term $\Omega = |\Omega|\, e^{i\phi}$ which depends on the Clebsch-Gordan coefficients and the phase of the driving field (see Section 3.4.2). In the following, the well-known driving equations are rederived in order maintain the global phase term. Here, this global phase for the two levels involved in the transfer is actually a relative phase of the four-level system.

The equation describing the population dynamics of a driven two-level system is

$$\dot{c}_1 = -\tfrac{i}{2}\Omega c_2 \ , \qquad \dot{c}_2 = -\tfrac{i}{2}\Omega^* c_1 \ , \tag{A.13}$$

which gives the equation $\ddot{c}_1 = -\frac{\Omega\Omega^*}{4}c_1$ with the general solution

$$\begin{aligned} c_1(t) &= a\cos\left(\tfrac{|\Omega|}{2}t\right) + b\sin\left(\tfrac{|\Omega|}{2}t\right) \ , \\ c_2(t) &= i\frac{2}{\Omega}\dot{c}_1(t) \\ &= i\frac{2}{\Omega}\frac{|\Omega|}{2}\left(-a\sin\left(\tfrac{|\Omega|}{2}t\right) + b\cos\left(\tfrac{|\Omega|}{2}t\right)\right) \\ &= ie^{-i\phi}\left(-a\sin\left(\tfrac{|\Omega|}{2}t\right) + b\cos\left(\tfrac{|\Omega|}{2}t\right)\right) \ . \end{aligned} \tag{A.14}$$

For both the basis transfer and the spin-echo transfer, one is interested in the full transfer, i.e. $\frac{|\Omega|}{2}t_\pi = \pi/2$. Hence,

$$c_1(0) = a, \qquad c_2(0) = ie^{-i\phi}b \tag{A.15}$$

and

$$c_1(t_\pi) = b = -ie^{i\phi}c_2(0), \qquad c_2(t_\pi) = -ie^{-i\phi}a = -ie^{-i\phi}c_1(0). \tag{A.16}$$

The basis state transfer with the π-polarized Raman light, $\exp(-it_{\pi/2}\hat{H}_\parallel/\hbar)$ as

$$\hat{R}_\parallel = \begin{bmatrix} \begin{bmatrix} 0 & -ie^{i\phi_0} \\ -ie^{-i\phi_0} & 0 \end{bmatrix} & 0 \\ 0 & \begin{bmatrix} e^{-i\delta_L t_{\pi/2}} & 0 \\ 0 & e^{+i3\delta_L t_{\pi/2}} \end{bmatrix} \end{bmatrix} . \tag{A.17}$$

Note that a complete suppression of the unwanted transfer $|F{=}1,\, m_F{=}1\rangle \leftrightarrow |F{=}2,\, m_F{=}1\rangle$ is assumed. Analogously, the transfer matrix for the spin-echo transfer with the σ_+/σ_--polarized light is given by.

$$\hat{R}_\perp = -i \begin{bmatrix} 0 & 0 & 0 & -e^{i\phi_\perp} \\ 0 & 0 & e^{-i\phi_\perp} & 0 \\ 0 & e^{i\phi_\perp} & 0 & 0 \\ -e^{-i\phi_\perp} & 0 & 0 & 0 \end{bmatrix} \tag{A.18}$$

with $\phi_\perp = \phi_0 - \theta$. When the Raman lights are switched *off* we have the free evolution Hamiltonian

$$\hat{H}_{\text{free}} = \frac{\hbar}{2} \begin{bmatrix} \begin{bmatrix} 2\delta_L & 0 \\ 0 & 2(\delta_{\text{free}} + \delta_L) \end{bmatrix} & 0 \\ 0 & \begin{bmatrix} +2\delta_L & 0 \\ 0 & 2(\delta_{\text{free}} - 2\delta_L) \end{bmatrix} \end{bmatrix} . \tag{A.19}$$

Although there are no light fields to drive the atom, δ_{free} is an important parameter: The Hamiltonian is still written in the rotating frame of the Raman pair and the phase difference of the two Raman beams rotates with the hyperfine splitting frequency of about 6.8 GHz. In the decoherence-protected memory basis, the phase of the qubit also rotates with the hyperfine splitting frequency which slightly differs from the frequencies used to generate the Raman pair. Without keeping this term, one would have a driving term Ω_π with a different phase. Practically, the microwave source (used to generate the sidebands) needs to be synchronised with the memory basis with a detuning of δ_{free}. The operator corresponding to a free evolution during a duration t is

$$\hat{U}_{\text{free}}(t) = e^{-i\hat{H}_{\text{free}}t} = \begin{bmatrix} \begin{bmatrix} e^{+i\delta_L t} & 0 \\ 0 & e^{-i(+\delta_{\text{free}}+\delta_L)t} \end{bmatrix} & 0 \\ 0 & \begin{bmatrix} e^{-i\delta_L t} & 0 \\ 0 & +e^{-i(\delta_{\text{free}}-\delta_L)t} \end{bmatrix} \end{bmatrix} . \tag{A.20}$$

In the rotating frame, the energy difference between the two levels where the qubit is stored (i.e. $|F = 1, m_F = -1\rangle$ and $|F = 2, m_F = +1\rangle$) is $\Delta E = \delta$. As expected, the free evolution of the qubit is approximately magnetic-field independent. The matrix which describes the storage in the memory basis is given by

$$\hat{R}_\parallel \hat{U}_{\text{free}}(\tau)\hat{R}_\parallel \ , \tag{A.21}$$

where τ is the duration of the storage. Hence, the qubit phase is modified as follows

$$\alpha|0\rangle + \beta|1\rangle \rightarrow \alpha|0\rangle + (-e^{i(6\delta_L t_{\pi/2} - \delta_{\text{free}}t))})\beta|1\rangle \ . \tag{A.22}$$

By choosing a detuning $\delta_{\text{free}} = 0$ by setting the splitting of the Raman pair to match the frequency splitting of the qubit basis during the free evolution time, only a time-independent phase term remains,

$$\pi + 6\delta_L t_\pi \ . \tag{A.23}$$

This phase offset can be compensated by adjusting a small delay before the final readout but after the qubit was transferred back to the interface basis where it rotates with twice the Larmor frequency. Importantly, the initial phase offset ϕ_0 imprinted by the Raman pair is compensated by the second transfer.

For the protocol which includes the spin echo pulse at half the storage time, the global phase-evolution operator is given by

$$\hat{R}_\parallel \ \hat{U}(\tau/2) \ \hat{R}_\perp \ \hat{U}(\tau/2) \ \hat{R}_\parallel \ . \tag{A.24}$$

The resulting state is

$$\alpha|0\rangle + \beta|1\rangle \rightarrow e^{i2(\phi_\perp - \phi_0)}\beta|0\rangle + \alpha|1\rangle. \tag{A.25}$$

Here, the phase of the qubit is $2(\phi_\perp - \phi_0) = 2\theta$. This time, by the principle of the spin echo technique, the detuning δ_{free} is always compensated whatever its value. As it can be seen, the rotation axis of the Bloch sphere is determined by θ. Without a fixed phase relation between $\hat{R}_\parallel$ and $\hat{R}_\perp$ the spin-echo rotation would have a random axis.

A.4. Carrier-Free Sideband Generation

The output field at one port of the interferometer is given by:

$$\begin{aligned} E_{\text{out}} =& \frac{E_0}{2}\left(e^{-i\omega t+\phi_0+\phi(t)} + e^{-i\omega t-\phi_0-\phi(t)}\right) && \text{(A.26)}\\ =& \frac{E_0}{2}e^{-i\omega t}\left(e^{+\phi_0+\phi(t)} + e^{-\phi_0-\phi(t)}\right) && \text{(A.27)}\\ =& E_0 e^{-i\omega t}\left(\cos\left(\phi_0+\phi(t)\right)\right) && \text{(A.28)} \end{aligned}$$

$$\begin{aligned} E_{\text{out}} &= E_0 e^{-i\omega t}\left(\cos\left(\phi_0+\phi(t)\right)\right) && \text{(A.29)}\\ &= E_0 e^{-i\omega t}\left(\cos\left(\phi_0\right)\cos(\alpha\cos(\delta t)) - \sin(\phi_0)\sin(\alpha\cos(\delta t))\right) && \text{(A.30)}\\ &\approx E_0 e^{-i\omega t}\left(\cos\left(\phi_0\right) - \sin(\phi_0)\alpha\cos(\delta t)\right) && \text{(A.31)}\\ &= \underbrace{E_0\cos(\phi_0)e^{-i\omega t}}_{\text{carrier}} - \underbrace{E_0\frac{\sin(\phi_0)}{2}e^{-i(\omega\pm\delta)t}}_{\text{symmetric sidebands}}. && \text{(A.32)} \end{aligned}$$

$$\begin{aligned} I(\phi_0) &= \langle|E|^2\rangle && \text{(A.33)}\\ &= E_0^2\left(\cos(\phi_0) + \sin(\phi_0)\alpha\cos(\delta t)\right)^2 && \text{(A.34)}\\ &= E_0\left(\cos(\phi_0)^2 + \sin(\phi_0)^2\alpha^2\cos(\delta t)^2 + 2\cos(\phi_0)\alpha\sin(\phi_0)\cos(\delta t)\right) && \text{(A.35)}\\ &= E_0\left(\cos(\phi_0)^2 + \frac{1}{2}\sin(\phi_0)^2\alpha^2\right). && \text{(A.36)} \end{aligned}$$

By evaluating the first and second order derivation with respect to ϕ_0 the points of minimum intensity as a function of ϕ_0 can be found:

$$\partial_{\phi_0} I = I' = E_0 \cos(\phi) \sin(\phi) \left(1 + \frac{\alpha^2}{2}\right) = 0 \tag{A.37}$$

$$\partial^2_{\phi_0} I = I'' = E_0 \left(\cos(\phi_0)\cos(\phi_0) - \sin(\phi)\sin(\phi)\right) \left(1 + \frac{\alpha^2}{2}\right) \tag{A.38}$$

$$I'\left(\frac{n}{2}\pi\right) = 0, \quad I''\left(n\pi\right) > 0, \quad I''\left((n+1/2)\pi\right) < 0 \quad \forall n \in \mathbb{N}. \tag{A.39}$$

A.5. Thermal State Qubit Fidelity Decay

$$\begin{aligned}
\mathcal{F}_{\text{thermal}} &= \sum_{\nu} p^{\bar{\nu}}_{\text{thermal}}(\nu) \cdot \mathcal{F}(\nu) \\
&= \sum_{\nu} \underbrace{\frac{1}{\bar{\nu}+1}}_{p_0} \underbrace{\left(\frac{\bar{\nu}}{\bar{\nu}+1}\right)^{\nu}}_{\alpha^\nu} \cdot \left(\frac{1}{2}\left(1 + V_0 \cos\left(\nu \Delta\omega t\right)\right)\right) \\
&= \frac{1}{2} + \frac{V_0 p_0}{4} \sum_{\nu} \alpha^\nu \left(e^{i\nu\Delta\omega t} + e^{-i\nu\Delta\omega t}\right) \\
&= \frac{1}{2} + \frac{V_0 p_0}{4} \left(\sum_{\nu} \left(\alpha e^{i\Delta\omega t}\right)^\nu + \sum \left(\alpha e^{-i\Delta\omega t}\right)^\nu\right) \\
&= \frac{1}{2} + \frac{V_0 p_0}{4} \left(\frac{1}{1 - \alpha e^{i\Delta\omega t}} + \frac{1}{1 - \alpha e^{-i\Delta\omega t}}\right) \\
&= \frac{1}{2} + \frac{V_0 p_0}{2} \frac{1 - \alpha\cos\left(\Delta\omega t\right)}{1 + \alpha^2 - 2\alpha\cos\left(\Delta\omega t\right)} \\
&= \frac{1}{2} + \frac{V_0}{2\left(\bar{\nu}+1\right)} \frac{1 - \frac{\bar{\nu}}{\bar{\nu}+1}\cos\left(\Delta\omega t\right)}{1 + \left(\frac{\bar{\nu}}{\bar{\nu}+1}\right)^2 - 2\alpha\cos\left(\Delta\omega t\right)}
\end{aligned} \tag{A.40}$$

A.6. Photon Detection Efficiency Calibration

To calibrate the detection efficiency of the single-photon counting modules (SPCM) the intensity of a macroscopic laser beam is measured with a conventional power meter (Thorlabs PM-160) and compared with the SPCM click rate after attenuating the beam by a known factor (Figure A.1 d). The attenuation to the single photon level is done by stacking neutral density filters (Thorlabs ND) which are individually calibrated using the conventional power meter. Since a neutral density filter can also effect the geometrical properties of the optical mode, the subsequent coupling efficiency to an optical fiber is affected. Therefore, the stacking of multiple filters in free space can result in an unpredictable change in coupling efficiency. This is solved by adding a fiber coupling after each individual ND filter (Figure A.1 c). The attenuation factor A_i and the relative error is given by

$$\mathrm{A}_i = \frac{\mathrm{I}_{\mathrm{ND}}}{\mathrm{I}_{\text{w/o ND}}}, \qquad \Delta\mathrm{A}_i^{\text{rel.sys}} = 2 \cdot \Delta\mathrm{I}_{\text{rel.sys}},$$

with the systematic error of the power meter $\Delta\mathrm{I}_{\text{sys}}$ which is dominated by a non-linear response and a non-uniformity of the active detector area. Since three different ND filters

are used, the total relative systematic calibration error sums up while the total attenuation is the product of the individual attenuations:

$$\mathrm{A}_{\mathrm{total}} = \Pi_i \mathrm{A}_i, \qquad \Delta\mathrm{A}^{\mathrm{rel.sys}}_{\mathrm{total}} = 6 \cdot \Delta\mathrm{I}_{\mathrm{rel.sys}}.$$

By measuring the attenuated power $\mathrm{I}_{\mathrm{w/o\ ND}}$ with a fiber coupled power meter, the non-uniformity of the power meter detection area can be ignored. A relative error in accuracy cancels and the zero-offset has to be well calibrated. With the combined attenuation factor the quantum efficiency of the SPCM can be derived from it's click rate Γ^{SPCM} using Einstein's famous photon-energy relation $E = {}^{h \cdot c}/_{\lambda}$:

$$\eta_{\mathrm{det}} = \frac{\text{click count}}{I_{\mathrm{w/o\ ND}} \Pi_i \mathrm{ND}_i} = \frac{(\Gamma^{\mathrm{SPCM}} - \Gamma^{\mathrm{SPCM}}_{\text{dark counts}}) \cdot h \cdot c}{\mathrm{I}_{\mathrm{w/o\ ND}} \cdot A^{\mathrm{total}} \cdot \lambda}.$$

Our typical SPCMs have a dark count rate of 20 Hz and a dead time in the order of 20 ns. For a stream of 100 k detected photons per second, the chance of having two photons within the dead time interval can be estimated using the Poissonian distribution: The average number of photons in a 20 ns interval is 0.002. This results in a probability of $P(X \geq 2) \approx 2 \cdot 10^{-6}$ of having a second photon during the dead time interval. This is even two orders of magnitude smaller than the probability $P(\text{dark count}) \approx 2 \cdot 10^{-4}$ that a detected click was a dark count. It is clear, that the error in the quantum efficiency is dominated by the error of the attenuation factor and the additional intensity measurement. In contrast to the calibration measurement of the ND filters, the absolute value of the measured power is important: A relative but constant error in accuracy of the power meter is not canceling, but contributing to the total error:

$$\Delta\eta_{\mathrm{det}} = \frac{\text{click count}}{I_{\mathrm{w/o\ ND}} \Pi_i \mathrm{ND}_i} \approx 7 \cdot \Delta\mathrm{I}_{\mathrm{rel.sys}} + \Delta\mathrm{I}_{\mathrm{rel.acc}}$$

The used power meter has a relative error in the power linearity $\Delta\mathrm{I}_{\mathrm{rel.sys}} = 1\%$, and a relative error in accuracy $\Delta\mathrm{I}_{\mathrm{rel.acc}} = 3\%$ resulting in a total error $\Delta\eta_{\mathrm{det}} = \frac{\text{click count}}{I_{\mathrm{w/o\ ND}} \Pi_i \mathrm{ND}_i} \approx 10\%$.

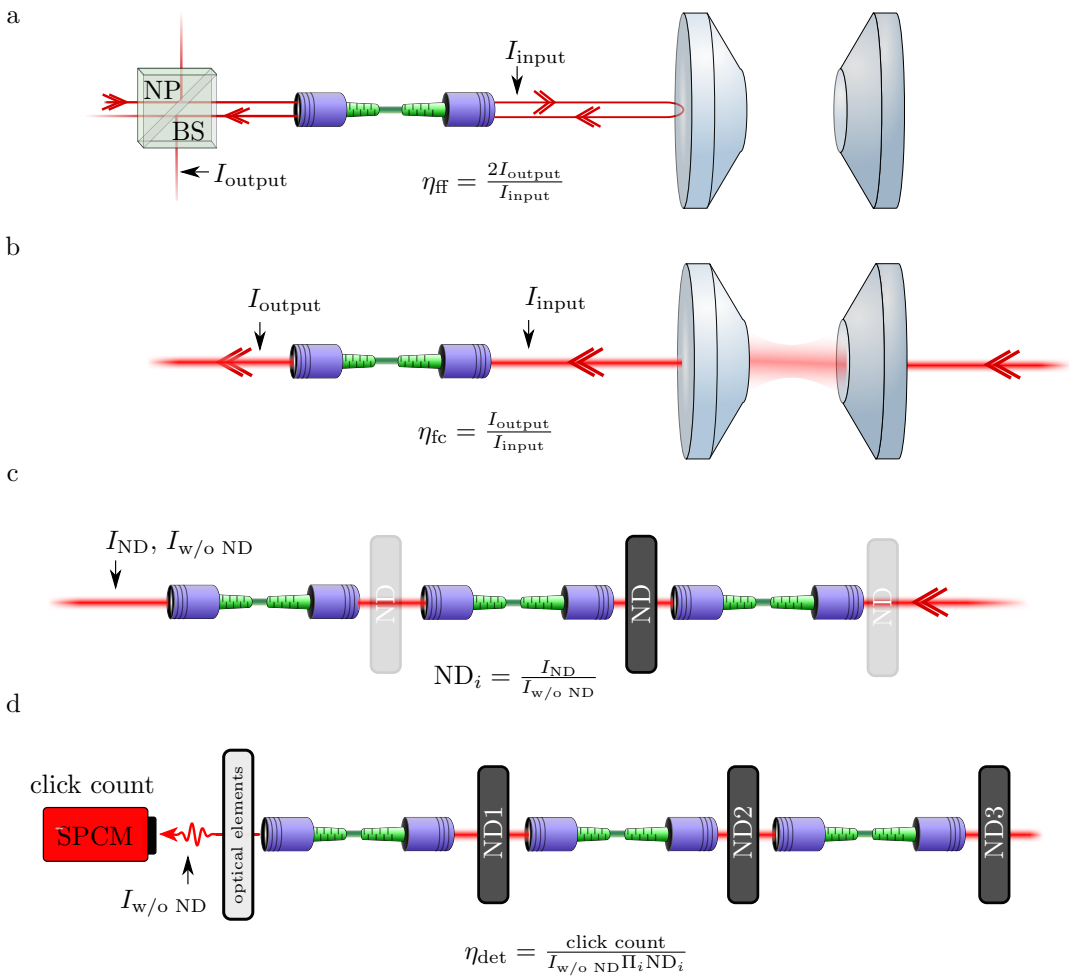

Figure A.1.: Coupling efficiency calibration: a) Fiber-fiber coupling efficiency. To measure the overlap of the light send to the cavity through the guiding-fiber, and the light which is reflected or coupled-out from the cavity, the ratio of the light which is coupled back to the guiding-fiber and the light which is send though the guiding-fiber to the cavity is measured. To this end, the light is send through a non-polarizing beam splitter before it is send through the guiding-fibre. By this, the intensity of the reflected light can be measured on one port of the beam splitter. **b)** The coupling efficiency of the free-field mode, which is coupled to the cavity, and the guiding-fiber is measured by coupling-in light through the high-reflector and measuring the light intensity in the free-space mode before and after the guiding-fiber. **c)** To reach the single-photon level for the input photon, an intense laser pulse must be attenuated by a well-known factor. To this end, a stack of three neutral density filters are calibrated individually to achieve a known total attenuation factor. Since a neutral density filter can affect the pointing of the beam, the three free-space filters are individually placed before an optical fiber. This prevents a change in the attenuation due to an affected beam pointing by a stack of filters which cannot be calibrated individually. **d)** The detection efficiency of the single-photon counting modules (SPCMs) is calibrated by impinging a macroscopic beam through the stack of calibrated neutral density filters. The observed photon count rate for a given frequency times the attenuation factor is compared with the macroscopic light intensity and yields the quantum efficiency of the SPCMs.

A.7. Calibration Coupling Efficiencies

To calibrate the overlap $\eta_{\text{fc}} = \frac{I_{\text{output}}}{I_{\text{input}}}$ between the free space mode coupled to the cavity and the free space mode coupled to the guiding fiber, the cavity is locked on resonance and light is impinged through the input coupler mirror. The intensity of the light leaving the output coupler is measured and compared with the amount of light leaving the guiding fiber

(Figure A.1 b). By neglecting losses in the fiber, this results in the mode overlap:

$$\eta_{\mathrm{fc}} = \frac{I_{\mathrm{output}}}{I_{\mathrm{input}}} = \frac{I_{\mathrm{output}}}{I_{\mathrm{input}}}, \qquad \Delta\eta_{\mathrm{fc}} = \frac{I_{\mathrm{output}}}{I_{\mathrm{input}}} \approx 2 \cdot \Delta \mathrm{I}_{\mathrm{rel.sys}}$$

The relative error derives again from the systematic error of the power meter due the non-linear response curve.

The fiber-fiber coupling efficiency $\eta_{\mathrm{ff}} = \frac{2I_{\mathrm{output}}}{I_{\mathrm{input}}}$ for a pulse reflected on the off-resonant cavity is calibrated using a beamsplitter as illustrated in Figure A.1 a). The power is measured after leaving the guiding fiber in the direction of the cavity an after being coupled again to the guiding fiber. Again, the error of the power meter translates to an error relative systematic error:

List of Figures

List of Tables

Bibliography

[1] K. Hentschel. *Lichtquanten: Die Geschichte des komplexen Konzepts und mentalen Modells von Photonen*. Springer-Verlag, 2017.

[2] M. Planck. Über das Gesetz der Energieverteilung im Normalspectrum. *Annalen der Physik* **309** (1901), 553.

[3] A. Einstein. Über einen die Erzeugung und Verwandlung des Lichtes betreffenden heuristischen Gesichtspunkt. *Annalen der physik* **322** (1905), 132.

[4] A. Einstein, B. Podolsky, and N. Rosen. Can Quantum-Mechanical Description of Physical Reality Be Considered Complete? *Phys. Rev.* **47** (1935), 777.

[5] A. Aspect, J. Dalibard, and G. Roger. Experimental Test of Bell's Inequalities Using Time-Varying Analyzers. *Phys. Rev. Lett.* **49** (1982), 1804.

[6] M. A. Rowe, D. Kielpinski, V. Meyer, C. A. Sackett, W. M. Itano, C. Monroe, and D. J. Wineland. Experimental violation of a Bell's inequality with efficient detection. *Nature* **409** (2001), 791.

[7] B. Hensen, H. Bernien, A. E. Dréau, A. Reiserer, N. Kalb, M. S. Blok, J. Ruitenberg, R. F. Vermeulen, R. N. Schouten, C. Abellán, et al. Loophole-free Bell inequality violation using electron spins separated by 1.3 kilometres. *Nature* **526** (2015), 682.

[8] M. Giustina et al. Significant-Loophole-Free Test of Bell's Theorem with Entangled Photons. *Phys. Rev. Lett.* **115** (2015), 250401.

[9] L. K. Shalm et al. Strong Loophole-Free Test of Local Realism. *Phys. Rev. Lett.* **115** (2015), 250402.

[10] B. B. T. Collaboration et al. Challenging local realism with human choices. *Nature* **557** (2018), 212.

[11] D. Rauch et al. Cosmic Bell Test Using Random Measurement Settings from High-Redshift Quasars. *Phys. Rev. Lett.* **121** (2018), 080403.

[12] J. S. Bell. On the Einstein Podolsky Rosen paradox. *Physics Physique Fizika* **1** (1964), 195.

[13] J. P. Dowling and G. J. Milburn. Quantum technology: the second quantum revolution. *Philosophical Transactions of the Royal Society of London A: Mathematical, Physical and Engineering Sciences* **361** (2003), 1655.

[14] R. P. Feynman. Simulating physics with computers. *International journal of theoretical physics* **21** (1982), 467.

[15] A. Trabesinger. Quantum simulation. *Nature Physics* **8** (2012), 263.

[16] P. W. Shor. Algorithms for quantum computation: discrete logarithms and factoring. *Proceedings of 35th Annual Symposium on Foundations of Computer Science* (1994), 124.

[17] G. Brassard and P. Hoyer. An exact quantum polynomial-time algorithm for Simon's problem. *Proceedings of the Fifth Israeli Symposium on Theory of Computing and Systems* (1997), 12.

[18] C. H. Bennett, E. Bernstein, G. Brassard, and U. Vazirani. Strengths and weaknesses of quantum computing. *SIAM journal on Computing* **26** (1997), 1510.

[19] L. K. Grover. From Schrödinger's equation to the quantum search algorithm. *Pramana* **56** (2001), 333.

[20] L. M. Vandersypen, M. Steffen, G. Breyta, C. S. Yannoni, R. Cleve, and I. L. Chuang. Experimental realization of an order-finding algorithm with an NMR quantum computer. *Physical Review Letters* **85** (2000), 5452.

[21] W. S. Warren. The usefulness of NMR quantum computing. *Science* **277** (1997), 1688.

[22] H. Häffner, C. F. Roos, and R. Blatt. Quantum computing with trapped ions. *Physics reports* **469** (2008), 155.

[23] J. I. Cirac and P. Zoller. Quantum Computations with Cold Trapped Ions. *Phys. Rev. Lett.* **74** (1995), 4091.

[24] J. Benhelm, G. Kirchmair, C. F. Roos, and R. Blatt. Towards fault-tolerant quantum computing with trapped ions. *Nature Physics* **4** (2008), 463.

[25] J. Clarke and F. K. Wilhelm. Superconducting quantum bits. *Nature* **453** (2008), 1031.

[26] M. Mariantoni et al. Implementing the Quantum von Neumann Architecture with Superconducting Circuits. *Science* **334** (2011), 61.

[27] L. DiCarlo, J. Chow, J. Gambetta, L. S. Bishop, B. Johnson, D. Schuster, J. Majer, A. Blais, L. Frunzio, S. Girvin, et al. Demonstration of two-qubit algorithms with a superconducting quantum processor. *Nature* **460** (2009), 240.

[28] D. Kielpinski, C. Monroe, and D. J. Wineland. Architecture for a large-scale ion-trap quantum computer. *Nature* **417** (2002), 709.

[29] D. P. DiVincenzo. Fault-tolerant architectures for superconducting qubits. *Physica Scripta* **2009** (2009), 014020.

[30] S. Wehner, D. Elkouss, and R. Hanson. Quantum internet: A vision for the road ahead. *Science* **362** (2018), eaam9288.

[31] L. Jiang, J. M. Taylor, A. S. Sørensen, and M. D. Lukin. Distributed quantum computation based on small quantum registers. *Physical Review A* **76** (2007), 062323.

[32] A. Serafini, S. Mancini, and S. Bose. Distributed Quantum Computation via Optical Fibers. *Phys. Rev. Lett.* **96** (2006), 010503.

[33] A. Yimsiriwattana and S. J. Lomonaco Jr. Distributed quantum computing: A distributed Shor algorithm. *Proceedings Volume 5436, Quantum Information and Computation II* **5436** (2004), 360.

[34] P. Komar, E. M. Kessler, M. Bishof, L. Jiang, A. S. Sørensen, J. Ye, and M. D. Lukin. A quantum network of clocks. *Nature Physics* **10** (2014), 582.

[35] L. Lamport, R. Shostak, and M. Pease. The Byzantine generals problem. *ACM Transactions on Programming Languages and Systems (TOPLAS)* **4** (1982), 382.

[36] M. J. Fischer, N. A. Lynch, and M. S. Paterson. *Impossibility of distributed consensus with one faulty process.* Tech. rep. Massachusetts Institute of Technology, 1982.

[37] L. Lamport et al. Paxos made simple. *ACM Sigact News* **32** (2001), 18.

[38] M. Ben-Or and A. Hassidim. *Fast quantum Byzantine agreement*. ACM, 2005.

[39] B. S. Chlebus, D. R. Kowalski, and M. Strojnowski. Scalable quantum consensus for crash failures. *International Symposium on Distributed Computing* (2010), 236.

[40] H. Bennett Ch and G. Brassard. Quantum cryptography: public key distribution and coin tossing Int. *Conf. on Computers, Systems and Signal Processing (Bangalore, India, Dec. 1984)* (1984), 175.

[41] T. Jennewein, C. Simon, G. Weihs, H. Weinfurter, and A. Zeilinger. Quantum cryptography with entangled photons. *Physical Review Letters* **84** (2000), 4729.

[42] A. Acin, N. Gisin, and L. Masanes. From Bell's Theorem to Secure Quantum Key Distribution. *Phys. Rev. Lett.* **97** (2006), 120405.

[43] M. Tomamichel and A. Leverrier. A largely self-contained and complete security proof for quantum key distribution. *Quantum* **1** (2017), 14.

[44] P. W. Shor and J. Preskill. Simple Proof of Security of the BB84 Quantum Key Distribution Protocol. *Phys. Rev. Lett.* **85** (2000), 441.

[45] W. K. Wootters and W. H. Zurek. A single quantum cannot be cloned. *Nature* **299** (1982), 802.

[46] G. Lindblad. A general no-cloning theorem. *Letters in Mathematical Physics* **47** (1999), 189.

[47] H. J. Kimble. The quantum internet. *Nature* **453** (2008), 1023.

[48] T. Northup and R. Blatt. Quantum information transfer using photons. *Nature photonics* **8** (2014), 356.

[49] D. P. DiVincenzo. The physical implementation of quantum computation. *Fortschritte der Physik: Progress of Physics* **48** (2000), 771.

[50] J. I. Cirac, P. Zoller, H. J. Kimble, and H. Mabuchi. Quantum State Transfer and Entanglement Distribution among Distant Nodes in a Quantum Network. *Phys. Rev. Lett.* **78** (1997), 3221.

[51] W. Munro, A. Stephens, S. Devitt, K. Harrison, and K. Nemoto. Quantum communication without the necessity of quantum memories. *Nature Photonics* **6** (2012), 777.

[52] H.-J. Briegel, W. Dür, J. I. Cirac, and P. Zoller. Quantum repeaters: the role of imperfect local operations in quantum communication. *Physical Review Letters* **81** (1998), 5932.

[53] M. Razavi, M. Piani, and N. Lütkenhaus. Quantum repeaters with imperfect memories: Cost and scalability. *Phys. Rev. A* **80** (2009), 032301.

[54] C. H. Bennett, G. Brassard, C. Crépeau, R. Jozsa, A. Peres, and W. K. Wootters. Teleporting an unknown quantum state via dual classical and Einstein-Podolsky-Rosen channels. *Phys. Rev. Lett.* **70** (1993), 1895.

[55] M. Barrett, J. Chiaverini, T. Schaetz, J. Britton, W. Itano, J. Jost, E. Knill, C. Langer, D. Leibfried, R. Ozeri, et al. Deterministic quantum teleportation of atomic qubits. *Nature* **429** (2004), 737.

[56] C. Nölleke, A. Neuzner, A. Reiserer, C. Hahn, G. Rempe, and S. Ritter. Efficient teleportation between remote single-atom quantum memories. *Physical review letters* **110** (2013), 140403.

[57] D. Boschi, S. Branca, F. De Martini, L. Hardy, and S. Popescu. Experimental Realization of Teleporting an Unknown Pure Quantum State via Dual Classical and Einstein-Podolsky-Rosen Channels. *Phys. Rev. Lett.* **80** (1998), 1121.

[58] P. P. Rohde, T. C. Ralph, and M. A. Nielsen. Optimal photons for quantum-information processing. *Phys. Rev. A* **72** (2005), 052332.

[59] C. Langer et al. Long-Lived Qubit Memory Using Atomic Ions. *Phys. Rev. Lett.* **95** (2005), 060502.

[60] P. C. Maurer et al. Room-Temperature Quantum Bit Memory Exceeding One Second. *Science* **336** (2012), 1283.

[61] M. Steger, K. Saeedi, M. L. W. Thewalt, J. J. L. Morton, H. Riemann, N. V. Abrosimov, P. Becker, and H.-J. Pohl. Quantum Information Storage for over 180 s Using Donor Spins in a 28Si "Semiconductor Vacuum". *Science* **336** (2012), 1280.

[62] N. Bar-Gill, L. M. Pham, A. Jarmola, D. Budker, and R. L. Walsworth. Solid-state electronic spin coherence time approaching one second. *Nature Commun.* **4** (2013). Article, 1743 EP.

[63] J. Yang, X. He, R. Guo, P. Xu, K. Wang, C. Sheng, M. Liu, J. Wang, A. Derevianko, and M. Zhan. Coherence Preservation of a Single Neutral Atom Qubit Transferred between Magic-Intensity Optical Traps. *Phys. Rev. Lett.* **117** (2016), 123201.

[64] M. Zhong, M. P. Hedges, R. L. Ahlefeldt, J. G. Bartholomew, S. E. Beavan, S. M. Wittig, J. J. Longdell, and M. J. Sellars. Optically addressable nuclear spins in a solid with a six-hour coherence time. *Nature* **517** (2015), 177.

[65] B. Casabone, K. Friebe, B. Brandstätter, K. Schüppert, R. Blatt, and T. E. Northup. Enhanced Quantum Interface with Collective Ion-Cavity Coupling. *Phys. Rev. Lett.* **114** (2015), 023602.

[66] A. B. Mundt, A. Kreuter, C. Becher, D. Leibfried, J. Eschner, F. Schmidt-Kaler, and R. Blatt. Coupling a Single Atomic Quantum Bit to a High Finesse Optical Cavity. *Phys. Rev. Lett.* **89** (2002), 103001.

[67] B. Brandstätter, A. McClung, K. Schüppert, B. Casabone, K. Friebe, A. Stute, P. O. Schmidt, C. Deutsch, J. Reichel, R. Blatt, and T. E. Northup. Integrated fiber-mirror ion trap for strong ion-cavity coupling. *Review of Scientific Instruments* **84** (2013), 123104.

[68] S. Riedl, M. Lettner, C. Vo, S. Baur, G. Rempe, and S. Dürr. Bose-Einstein condensate as a quantum memory for a photonic polarization qubit. *Phys. Rev. A* **85** (2012), 022318.

[69] M. G. Raymer and K. Srinivasan. Manipulating the color and shape of single photons. *Physics Today* **65** (2012), 32.

[70] M. Keller, B. Lange, K. Hayasaka, W. Lange, and H. Walther. Continuous generation of single photons with controlled waveform in an ion-trap cavity system. *Nature* **431** (2004), 1075.

[71] M. Eisaman, L. Childress, A. André, F. Massou, A. Zibrov, and M. Lukin. Shaping quantum pulses of light via coherent atomic memory. *Physical review letters* **93** (2004), 233602.

[72] M. D. Eisaman, L. Childress, A. André, F. Massou, A. S. Zibrov, and M. D. Lukin. Shaping Quantum Pulses of Light Via Coherent Atomic Memory. *Phys. Rev. Lett.* **93** (2004), 233602.

[73] M. Eisaman, A. André, F. Massou, M. Fleischhauer, A. Zibrov, and M. Lukin. Electromagnetically induced transparency with tunable single-photon pulses. *Nature* **438** (2005), 837.

[74] S. Zhou, S. Zhang, C. Liu, J. Chen, J. Wen, M. Loy, G. K. L. Wong, and S. Du. Optimal storage and retrieval of single-photon waveforms. *Optics express* **20** (2012), 24124.

[75] P. B. Nisbet-Jones, J. Dilley, D. Ljunggren, and A. Kuhn. Highly efficient source for indistinguishable single photons of controlled shape. *New Journal of Physics* **13** (2011), 103036.

[76] P. Farrera, G. Heinze, B. Albrecht, M. Ho, M. Chávez, C. Teo, N. Sangouard, and H. De Riedmatten. Generation of single photons with highly tunable wave shape from a cold atomic ensemble. *Nature communications* **7** (2016), 13556.

[77] H. P. Specht, J. Bochmann, M. Mücke, B. Weber, E. Figueroa, D. L. Moehring, and G. Rempe. Phase shaping of single-photon wave packets. *Nature Photonics* **3** (2009), 469.

[78] P. Kolchin, C. Belthangady, S. Du, G. Yin, and S. E. Harris. Electro-optic modulation of single photons. *Physical review letters* **101** (2008), 103601.

[79] S. Chu. Nobel Lecture: The manipulation of neutral particles. *Reviews of Modern Physics* **70** (1998), 685.

[80] W. D. Phillips. Nobel Lecture: Laser cooling and trapping of neutral atoms. *Reviews of Modern Physics* **70** (1998), 721.

[81] G. Rempe, R. Thompson, H. J. Kimble, and R. Lalezari. Measurement of ultralow losses in an optical interferometer. *Optics letters* **17** (1992), 363.

[82] H. J. Kimble. Strong interactions of single atoms and photons in cavity QED. *Physica Scripta* **1998** (1998), 127.

[83] B. W. Shore and P. L. Knight. The jaynes-cummings model. *Journal of Modern Optics* **40** (1993), 1195.

[84] A. D. Boozer, A. Boca, R. Miller, T. E. Northup, and H. J. Kimble. Reversible State Transfer between Light and a Single Trapped Atom. *Phys. Rev. Lett.* **98** (2007), 193601.

[85] T. Wilk, S. C. Webster, A. Kuhn, and G. Rempe. Single-atom single-photon quantum interface. *Science* **317** (2007), 488.

[86] M. Mücke, J. Bochmann, C. Hahn, A. Neuzner, C. Nölleke, A. Reiserer, G. Rempe, and S. Ritter. Generation of single photons from an atom-cavity system. *Phys. Rev. A* **87** (2013), 063805.

[87] N. Kalb, A. Reiserer, S. Ritter, and G. Rempe. Heralded Storage of a Photonic Quantum Bit in a Single Atom. *Phys. Rev. Lett.* **114** (2015), 220501.

[88] A. Kuhn, M. Hennrich, and G. Rempe. Deterministic single-photon source for distributed quantum networking. *Physical review letters* **89** (2002), 067901.

[89] A. Kuhn and D. Ljunggren. Cavity-based single-photon sources. *Contemporary Physics* **51** (2010), 289.

[90] A. V. Gorshkov, A. André, M. D. Lukin, and A. S. Sørensen. Photon storage in Λ-type optically dense atomic media. I. Cavity model. *Phys. Rev. A* **76** (2007), 033804.

[91] J. Dilley, P. Nisbet-Jones, B. W. Shore, and A. Kuhn. Single-photon absorption in coupled atom-cavity systems. *Phys. Rev. A* **85** (2012), 023834.

[92] M. Fleischhauer, S. Yelin, and M. Lukin. How to trap photons? Storing single-photon quantum states in collective atomic excitations. *Optics Communications* **179** (2000), 395.

[93] A. Reiserer, N. Kalb, G. Rempe, and S. Ritter. A quantum gate between a flying optical photon and a single trapped atom. *Nature* **508** (2014), 237.

[94] B. Hacker, S. Welte, G. Rempe, and S. Ritter. A photon–photon quantum gate based on a single atom in an optical resonator. *Nature* **536** (2016), 193.

[95] S. Welte, B. Hacker, S. Daiss, S. Ritter, and G. Rempe. Photon-Mediated Quantum Gate between Two Neutral Atoms in an Optical Cavity. *Physical Review X* **8** (2018), 011018.

[96] H. P. Specht, C. Nolleke, A. Reiserer, M. Uphoff, E. Figueroa, S. Ritter, and G. Rempe. A single-atom quantum memory. *Nature* **473** (2011), 190.

[97] P. Treutlein, P. Hommelhoff, T. Steinmetz, T. W. Hänsch, and J. Reichel. Coherence in Microchip Traps. *Phys. Rev. Lett.* **92** (2004), 203005.

[98] A. Reiserer, C. Nölleke, S. Ritter, and G. Rempe. Ground-State Cooling of a Single Atom at the Center of an Optical Cavity. *Phys. Rev. Lett.* **110** (2013), 223003.

[99] S. Nussmann, M. Hijlkema, B. Weber, F. Rohde, G. Rempe, and A. Kuhn. Submicron Positioning of Single Atoms in a Microcavity. *Phys. Rev. Lett.* **95** (2005), 173602.

[100] S. Ritter, C. Nölleke, C. Hahn, A. Reiserer, A. Neuzner, M. Uphoff, M. Mücke, E. Figueroa, J. Bochmann, and G. Rempe. An elementary quantum network of single atoms in optical cavities. *Nature* **484** (2012), 195.

[101] M. Lettner, M. Mücke, S. Riedl, C. Vo, C. Hahn, S. Baur, J. Bochmann, S. Ritter, S. Dürr, and G. Rempe. Remote entanglement between a single atom and a Bose-Einstein condensate. *Physical Review Letters* **106** (2011), 210503.

[102] D. Hunger, T. Steinmetz, Y. Colombe, C. Deutsch, T. W. Hänsch, and J. Reichel. A fiber Fabry–Perot cavity with high finesse. *New Journal of Physics* **12** (2010), 065038.

[103] A. Muller, E. B. Flagg, J. R. Lawall, and G. S. Solomon. Ultrahigh-finesse, low-mode-volume Fabry–Perot microcavity. *Optics letters* **35** (2010), 2293.

[104] M. Uphoff, M. Brekenfeld, G. Rempe, and S. Ritter. Frequency splitting of polarization eigenmodes in microscopic Fabry–Perot cavities. *New Journal of Physics* **17** (2015), 013053.

[105] M. Körber, O. Morin, S. Langenfeld, A. Neuzner, S. Ritter, and G. Rempe. Decoherence-protected memory for a single-photon qubit. *Nature Photonics* **12** (2018), 18.

[106] U. Gaubatz, P. Rudecki, S. Schiemann, and K. Bergmann. Population transfer between molecular vibrational levels by stimulated Raman scattering with partially overlapping laser fields. A new concept and experimental results. *The Journal of Chemical Physics* **92** (1990), 5363.

[107] N. V. Vitanov, A. A. Rangelov, B. W. Shore, and K. Bergmann. Stimulated Raman adiabatic passage in physics, chemistry, and beyond. *Rev. Mod. Phys.* **89** (2017), 015006.

[108] L. Giannelli, T. Schmit, T. Calarco, C. P. Koch, S. Ritter, and G. Morigi. Optimal storage of a single photon by a single intra-cavity atom. *New Journal of Physics* **20** (2018), 105009.

[109] H.-P. Breuer, F. Petruccione, et al. *The theory of open quantum systems*. Oxford University Press on Demand, 2002.

[110] H. Carmichael. An open systems approach to quantum optics: Lectures presented at the Universite Libre De Bruxelles October 28 to November 4. *Lecture notes in physics (Springer-Verlag, Berlin, 1991)* (1991).

[111] M. Mücke, J. Bochmann, C. Hahn, A. Neuzner, C. Nölleke, A. Reiserer, G. Rempe, and S. Ritter. Generation of single photons from an atom-cavity system. *Physical Review A* **87** (2013), 063805.

[112] L. Giannelli and E. Arimondo. Three-level superadiabatic quantum driving. *Physical Review A* **89** (2014), 033419.

[113] D. Rieländer, A. Lenhard, M. Mazzera, and H. de Riedmatten. Cavity enhanced telecom heralded single photons for spin-wave solid state quantum memories. *New Journal of Physics* **18** (2016), 123013.

[114] W. Bowen and G. J. Milburn. *Quantum optomechanics*. CRC Press, 2015.

[115] Z. Qin, A. S. Prasad, T. Brannan, A. MacRae, A. Lezama, and A. Lvovsky. Complete temporal characterization of a single photon. *Light: Science & Applications* **4** (2015), e298.

[116] O. Morin, C. Fabre, and J. Laurat. Experimentally Accessing the Optimal Temporal Mode of Traveling Quantum Light States. *Phys. Rev. Lett.* **111** (2013), 213602.

[117] O. Morin, S. Langenfeld, M. Körber, and G. Rempe. Accurate photonic temporal mode analysis with reduced resources. *Phys. Rev. A* **101** (2020), 013801.

[118] A. Neuzner. Resonance Fluorescence of an Atom Pair in an Optical Resonator. *Dissertation, Technische Universität München* (2016).

[119] D. T. Smithey, M. Beck, M. Belsley, and M. G. Raymer. Sub-shot-noise correlation of total photon number using macroscopic twin pulses of light. *Phys. Rev. Lett.* **69** (1992), 2650.

[120] L. Giannelli, T. Schmit, and G. Morigi. Weak coherent pulses for single-photon quantum memories. *Physica Scripta* **94** (2018), 014012.

[121] C. Kupchak, T. Mittiga, B. Jordaan, M. Namazi, C. Nölleke, and E. Figueroa. Room-Temperature Single-photon level Memory for Polarization States. *Scientific Reports* **5** (2015). Article, 7658 EP.

[122] M. Namazi, C. Kupchak, B. Jordaan, R. Shahrokhshahi, and E. Figueroa. Unconditional polarization qubit quantum memory at room temperature. *Preprint at http://arXiv.org/abs/arXiv:1512.07374* (2015).

[123] Y.-A. Chen, S. Chen, Z.-S. Yuan, B. Zhao, C.-S. Chuu, J. Schmiedmayer, and J.-W. Pan. Memory-built-in quantum teleportation with photonic and atomic qubits. *Nat. Phys.* **4** (2008), 103.

[124] B. Zhao, Y.-A. Chen, X.-H. Bao, T. Strassel, C.-S. Chuu, X.-M. Jin, J. Schmiedmayer, Z.-S. Yuan, S. Chen, and J.-W. Pan. A millisecond quantum memory for scalable quantum networks. *Nat. Phys.* **5** (2009), 95.

[125] S.-J. Yang, X.-J. Wang, X.-H. Bao, and J.-W. Pan. An efficient quantum light–matter interface with sub-second lifetime. *Nat. Photon.* **10** (2016). Letter, 381.

[126] X.-H. Bao, A. Reingruber, P. Dietrich, J. Rui, A. Duck, T. Strassel, L. Li, N.-L. Liu, B. Zhao, and J.-W. Pan. Efficient and long-lived quantum memory with cold atoms inside a ring cavity. *Nat. Phys.* **8** (2012), 517.

[127] R. Zhao, Y. O. Dudin, S. D. Jenkins, C. J. Campbell, D. N. Matsukevich, T. A. B. Kennedy, and A. Kuzmich. Long-lived quantum memory. *Nat. Phys.* **5** (2009), 100.

[128] L.-M. Duan, M. Lukin, J. I. Cirac, and P. Zoller. Long-distance quantum communication with atomic ensembles and linear optics. *Nature* **414** (2001), 413.

[129] B. Schumacher. Quantum coding. *Phys. Rev. A* **51** (1995), 2738.

[130] M. A. Nielsen and I. Chuang. *Quantum computation and quantum information*. 2002.

[131] C. Cohen-Tannoudji, B. Diu, and F. Laloe. *Quantum Mechanics*. Quantum Mechanics. Wiley, 1991.

[132] E. L. Hahn. Spin Echoes. *Phys. Rev.* **80** (1950), 580.

[133] L. Viola and S. Lloyd. Dynamical suppression of decoherence in two-state quantum systems. *Phys. Rev. A* **58** (1998), 2733.

[134] L. Viola, E. Knill, and S. Lloyd. Dynamical Decoupling of Open Quantum Systems. *Phys. Rev. Lett.* **82** (1999), 2417.

[135] D. D. Traficante. Relaxation. Can T2, be longer than T1? *Concepts in Magnetic Resonance* **3** (1991), 171.

[136] J. Altepeter, E. Jeffrey, and P. Kwiat. Photonic State Tomography. Ed. by P. Berman and C. Lin. Vol. 52. Advances In Atomic, Molecular, and Optical Physics. Academic Press, 2005, 105.

[137] J. v. Neumann. Wahrscheinlichkeitstheoretischer Aufbau der Quantenmechanik. *Nachrichten von der Gesellschaft der Wissenschaften zu Göttingen, Mathematisch-Physikalische Klasse* **1927** (1927), 245.

[138] M. Schlüter and L. Jeu Sham. Density functional theory. *Physics Today* **35** (1982), 36.

[139] U. Fano. Density matrices as polarization vectors. *Rendiconti Lincei* **6** (1995), 123.

[140] U. Fano. A Stokes-Parameter Technique for the Treatment of Polarization in Quantum Mechanics. *Phys. Rev.* **93** (1954), 121.

[141] N. F. Ramsey. A Molecular Beam Resonance Method with Separated Oscillating Fields. *Phys. Rev.* **78** (1950), 695.

[142] C. F. Roos, M. Chwalla, K. Kim, M. Riebe, and R. Blatt. 'Designer atoms' for quantum metrology. *Nature* **443** (2006), 316.

[143] J. Clarke and F. K. Wilhelm. Superconducting quantum bits. *Nature* **453** (2008), 1031.

[144] D. A. Steck. *Rubidium 87 D line data*. 2001.

[145] L. Sárkány, P. Weiss, H. Hattermann, and J. Fortágh. Controlling the magnetic-field sensitivity of atomic-clock states by microwave dressing. *Phys. Rev. A* **90** (2014), 053416.

[146] T. Ruster, C. T. Schmiegelow, H. Kaufmann, C. Warschburger, F. Schmidt-Kaler, and U. G. Poschinger. A long-lived Zeeman trapped-ion qubit. *Applied Physics B* **122** (2016), 254.

[147] H. Specht. Einzelatom-Quantenspeicher für Polarisations-Qubits. *Dissertation, Technische Universität München* (2010).

[148] H. Metcalf and P. van der Straten. Cooling and trapping of neutral atoms. *Physics reports* **244** (1994), 203.

[149] A. J. Kerman, Vuleti ć, C. Chin, and S. Chu. Beyond Optical Molasses: 3D Raman Sideband Cooling of Atomic Cesium to High Phase-Space Density. *Phys. Rev. Lett.* **84** (2000), 439.

[150] A. Reiserer, C. Nölleke, S. Ritter, and G. Rempe. Ground-State Cooling of a Single Atom at the Center of an Optical Cavity. *Phys. Rev. Lett.* **110** (2013), 223003.

[151] J. C. Camparo. *The rubidium atomic clock and basic research*. Tech. rep. AEROSPACE CORP EL SEGUNDO CA PHYSICAL SCIENCES LABS, 2007.

[152] J. Bochmann, M. Mücke, C. Guhl, S. Ritter, G. Rempe, and D. L. Moehring. Lossless State Detection of Single Neutral Atoms. *Phys. Rev. Lett.* **104** (2010), 203601.

[153] S. Riedl, M. Lettner, C. Vo, S. Baur, G. Rempe, and S. Dürr. Bose-Einstein condensate as a quantum memory for a photonic polarization qubit. *Phys. Rev. A* **85** (2012), 022318.

[154] C. V. Raman and K. S. Krishnan. A new type of secondary radiation. *Nature* **121** (1928), 501.

[155] M. Uphoff. State manipulation of single atoms in an optical cavity. *Diploma thesis, Technische Universität München* (2010).

[156] R. A. Cline, J. D. Miller, M. R. Matthews, and D. J. Heinzen. Spin relaxation of optically trapped atoms by light scattering. *Opt. Lett.* **19** (1994), 207.

[157] R. Grimm, M. Weidemüller, and Y. B. Ovchinnikov. Optical Dipole Traps for Neutral Atoms. Ed. by B. Bederson and H. Walther. Vol. 42. Advances In Atomic, Molecular, and Optical Physics. Academic Press, 2000, 95.

[158] S. Kuhr, W. Alt, D. Schrader, I. Dotsenko, Y. Miroshnychenko, W. Rosenfeld, M. Khudaverdyan, V. Gomer, A. Rauschenbeutel, and D. Meschede. Coherence Properties and Quantum State Transportation in an Optical Conveyor Belt. *Phys. Rev. Lett.* **91** (2003), 213002.

[159] A. Neuzner, M. Körber, O. Morin, S. Ritter, and G. Rempe. Interference and dynamics of light from a distance-controlled atom pair in an optical cavity. *Nature Photonics* **10** (2016), 303.

[160] Bayer Manfred. Spin echo with light. *Nature Photonics* **4** (2010), 347.